A quantitative Kohn–Sham approach to elementary redox reactions in artificial, bio-inspired and biological catalysis

Dalla Tiezza, Marco

2021

document version
Publisher's PDF, also known as Version of record

A Quantitative Kohn–Sham Approach to Elementary Redox Reactions in Artificial, Bio-Inspired and Biological Catalysis

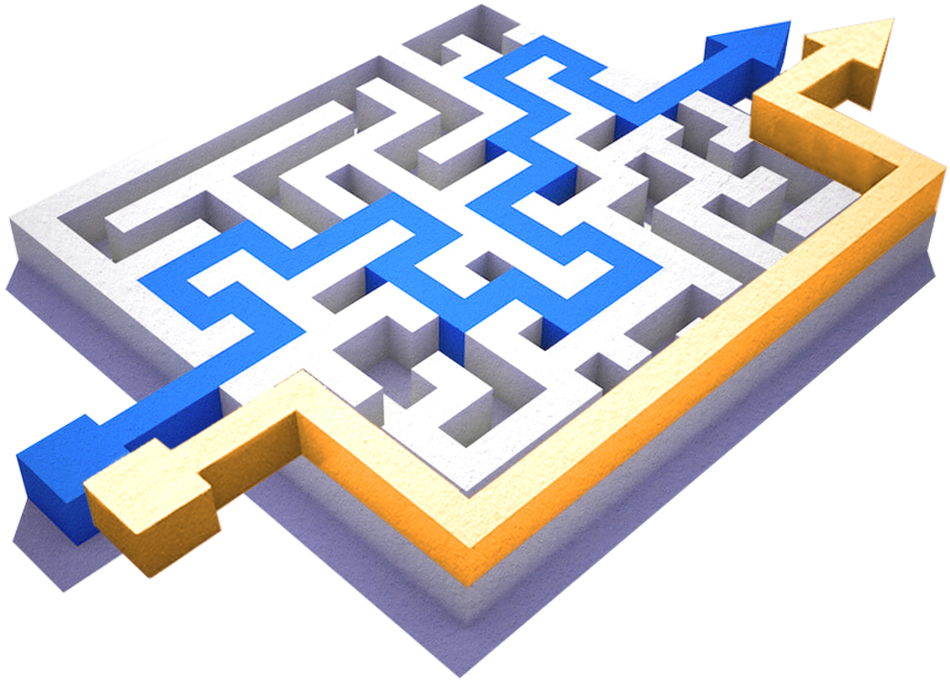

Marco Dalla Tiezza

VRIJE UNIVERSITEIT

A QUANTITATIVE KOHN–SHAM APPROACH TO ELEMENTARY REDOX REACTIONS IN ARTIFICIAL, BIO-INSPIRED AND BIOLOGICAL CATALYSIS

ACADEMISCH PROEFSCHRIFT

ter verkrijging van de graad Doctor aan
de Vrije Universiteit Amsterdam en
Università degli Studi di Padova
op gezag van de rectores magnifici
prof.dr. V. Subramaniam
en prof.dr. R. Rizzuto
in het openbaar te verdedigen
ten overstaan van de promotiecommissie
van de Faculteit der Bètawetenschappen
op 20 september 2021 om 13.45 uur
in de online bijeenkomst van de universiteit,
De Boelelaan 1105

door

Marco Dalla Tiezza

geboren te Feltre, Italië

promotoren: prof.dr. F.M. Bickelhaupt

prof.dr. L. Orian

Università degli Studi di Padova

Department of Chemical Sciences

Department of Theoretical Chemistry

Administrative seat: University of Padova
Doctoral Course in Molecular Sciences
Curriculum: Chemical Sciences
Cycle: XXXIII
Coordinator: Prof. Dr. Leonard Jan Prins

Vrije Universiteit Amsterdam
Doctoral Programme in Chemistry

A quantitative Kohn–Sham approach to elementary redox reactions in artificial, bio-inspired and biological catalysis

Supervisors: Prof. Dr. F. Matthias Bickelhaupt

Prof. Dr. Laura Orian

Ph. D. Candidate: Marco Dalla Tiezza

This manuscript has been presented to jointly opt for the doctoral degree from the University of Padova and the Vrije Universiteit Amsterdam

A quantitative Kohn–Sham approach to elementary redox reactions in artificial, bio-inspired and biological catalysis

"Although my mother didn't know anything about science, she had a great influence on me as well. In particular, she had a wonderful sense of humor, and I learned from her that the highest forms of understanding we can achieve are laughter and human compassion."

-Richard P. Feynman,

What Do You Care What Other People Think?

Table of Contents

List of Figures

List of Tables

1 Introduction

I believe that summarizing in a simple and sober way the impressiveness of catalysis in modern chemistry can be considered a chimera by the most. On October 1948, Ralph Edward Oesper, an American chemist and historian of chemistry, condensed in a couple of pages the life of Alwin Mittasch, a German chemist, particularly known for his first systematic research on the catalysts development for the synthesis of ammonia via the Haber-Bosch process [1]. In this brief essay, we can find a statement that, in some way, tries to give merit to what has been previously said:

> *"Chemistry without catalysis would be a sword without a handle, a light without brilliance, a bell without sound."*
>
> *Paul Alwin Mittasch*

These words are meant to introduce in an understandable and accessible way the importance of catalysis in both every day and non-daily chemistry. However, just before we support what has been said, it is worth answering the following not obvious question: what is catalysis?

The expression was first coined in 1836 by the Swedish scientist Jöns Jacob Berzelius, particularly famous for the discovery of various elements of the periodic table such as cerium, silicon, thorium and selenium: we will see that this last chalcogen, incidentally, will be of paramount importance for the final three chapters of this thesis.

Returning back to the main question: catalysis is the acceleration (or even the slowing down) of chemical reactions by substances, called catalysts, that are not consumed during the whole process: the catalyst can transform and undergo important structural alterations but, in the end, it can always be recovered in its original state. More specifically, catalysts are substances that, added in small amounts to a chemical reaction, modify the reaction kinetics, providing an alternative mechanism of reaction with a reduced activation energy. They are not expended during the reaction itself and therefore they do not appear in the global reaction equations: this means that they do not cause any variation in the value of the equilibrium constant.

Although catalysts are not consumed by the reaction itself, they are not unbreakable: they can be inhibited, deactivated or destroyed by undesirable secondary processes.

Despite their generally high cost, catalysts are widely used in industry because they not only allow a considerable speed up of the process but in some cases are essential to ensure its purity (an example is the Ziegler-Natta catalysts for the synthesis of stereoregular polypropylene). In addition, in the following chapters, we will see how certain processes may not occur unless properly catalyzed.

Speaking of the influence on the global market, there is no need to emphasize that catalysts are a big deal: in 2018 their revenue (including

the polymer industry) is estimated to be around 5.5 billion euros. This evaluation clearly does not take into account the added value of the final product, which is far superior to the value given by the used catalyst, also considering the amount ratio between them.

Catalysis can be extremely diverse and, for this reason, it's impossible to present a complete list, however, a brief overview of the most widely used and famous catalysts will be given hereafter. Without any doubt, in organic catalysis and especially for the numerous reactions involving water, including hydrolysis, acid (or basic) catalysis is crucial for the success of many reactions. In inorganic catalysis, instead, we find multifunctional solids such as zeolites, alumina, oxides, graphite, nanoparticles and nanodots. Transition metals are often used to catalyze redox reactions such as oxidations or hydrogenations, for instance. Noteworthy examples are nickel, as in nickel Raney for hydrogenation, and vanadium oxide (V) for the oxidation of sulfur dioxide to sulfur trioxide in the sulfuric acid production. Many catalytic processes, particularly those used in organic synthesis, require complexes of the so-called "late transition metals" such as palladium, platinum, gold, ruthenium, cobalt, rhodium or iridium. Elements in metallic form can also be excellent catalysts.

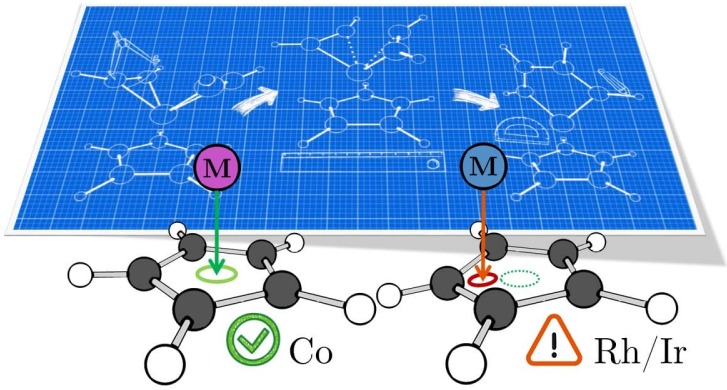

Figure 1.1. Nowadays, the rational designing of more efficient catalysts means to significantly increase the reaction rate, wasting less catalyst and reducing the production costs of the finished product.

In Chapter 3 of this thesis, we will focus on the latter 3 metals (Group 9) taking into account an archetypal reaction aimed at the synthesis of differently substituted benzene rings, pyridine and its derivatives, and in general polycyclic compounds, which are extremely important in the industrial field for their use as precursors of more complex compounds in the pharmaceutical field. Particular attention will be devoted to the role of the catalyst in order to evaluate its activity and then look into ways to improve its performance in order to increase the reaction rate: this approach is better known as rational catalyst design.

The aforementioned reaction is better defined as a [2+2+2] cycloaddition (or cyclotrimerization) where annular molecules are synthesized starting from their constituent fragments. In the simple case of benzene or pyridine, the reactants are acetylene and acetonitrile as shown in Figure 1.2.

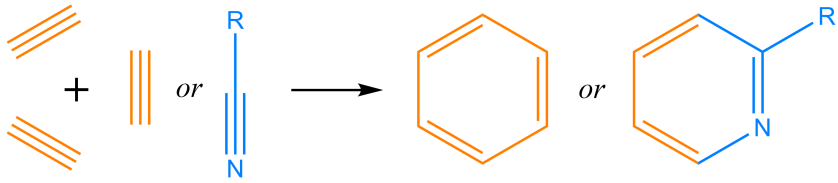

Figure 1.2. [2+2+2] acetylene cycloaddition to benzene can be easily used also to form pyridine derivatives using differently substituted nitriles.

One question arises spontaneously: why must this process be catalyzed? The answer is rather simple considering the Figure 1.2: the reaction is extremely unfavorable from an entropic point of view. In fact, also for other types of processes (e.g. Chichibabin synthesis), high yields are only reported through the use of alumina and/or aluminosilicates, such as zeolites and carrying out the process at high temperature. The synthesis of pyridine catalyzed by transition metal complexes from alkynes and nitriles was first described by Reppe [2] back in 1940s with Ni(II) based catalysts and 1,3,5,7-cyclooctatetraene (COT) as the main ligand. Some pioneering studies have followed in 1973 by Wakatsuki and Yamazaki [3], by Vollhardt et al. [4,5] and by Bönnemann et al. [6,7] in the 80s. Since the beginning, a particular class of compounds exhibited good catalytic activity toward alkynes [2+2+2] cycloadditions: the half-sandwich metal complexes. Particularly, Co(I) and Rh(I) complexes were the most performing and, therefore, the most studied ones (Figure 1.1).

A peculiar structural feature of these catalysts is the coordination of the metal to an aromatic moiety, typically a cyclopentadienyl anion, and they offer the possibility of easily changing the bonding mode by the metal slipping over this aromatic moiety (Figure 1.3). When modifying the ancillary ligands, or proceeding along the catalytic cycle, hapticity changes can be observed, varying from η^5, when the five metal-carbon distances are identical, to $\eta^3 + \eta^2$, in presence of allylic distortion, to η^3, in case of allylic coordination, to η^1, when a sigma metal-carbon bond forms.

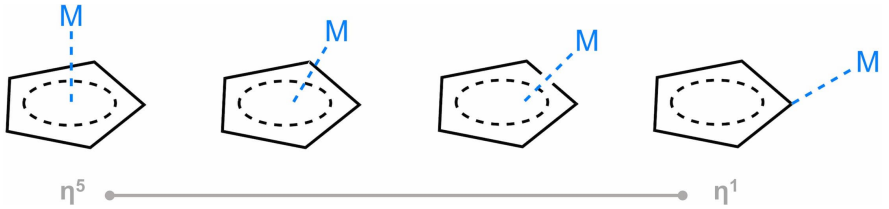

Figure 1.3. Hapticity variation for a cyclopentadienyl-based metal complex. The metal center is not fixed but can more or less smoothly slip above the aromatic moiety.

This extremely evident and easy to notice characteristic is anything but straightforward to understand. This feature reflects both steric and electronic effects and, as we will see in Chapters 3 and 4, it contains all the information we need to define the reactivity of these systems by knowing their geometry (or the geometry of the structures involved in the whole catalytic cycle).

In Chapters 3 and 4, we will present the slippage span model, derived with the aim of establishing a relationship between the slippage variation during the catalytic cycle, quantified in a novel and rigorous way, and the performance of the catalyst in terms of turnover frequency (TOF), computed with the energy span model (explained in Chapter 2). By defining a scale of reactivity, directly related to a geometrical descriptor, it's relatively easy to draw new molecules designed to improve the catalytic activity, proceeding, in this way, to a rational design of novel catalytic moieties.

So far, I have presented some relevant and general aspects of catalysis in chemistry, but I deliberately have not mentioned any detail of one of the most essential aspects. A so crucial characteristic that, most likely, if it were not present in nature, there would not be any form of life as we know it. As you may have already guessed, I am referring to the catalysis of enzymes: the principles do not change from what I have above described, but things are getting much more complicated. A lot more complicated. A living organism is a complex chemical system in which organic matter is synthesized, reproduced, transformed, and

decomposed in a continuous and intense succession of reactions and chemical processes through which all biological functions are performed. Changing the speed of these biochemical processes is essential for the life of the organism, and, commonly, this task is handled by a humongous molecule with an incredible high selectivity that can be activated, inhibited, or modulated only under specific circumstances: the enzyme.

The life of an organism is a fragile balance of equilibria, where most of them are managed at enzymatic level. To give an example, each of us, even at this very moment, is fighting against cellular oxidation, better defined as 'oxidative stress'. This natural process is in fact the primary cause of aging due to the harmful action of exogenous and endogenous factors (exposure to sunlight, pollution, and the normal functioning of our body's metabolism). Oxidative stress is triggered when an excess of free radicals and highly reactive molecules accumulates in an organism preventing cells from defending and protecting themselves.

Several pathologies and diseases can arise from this unbalanced concentration of very reactive species, most of which are ROS (Reactive Oxygen Species) and RNS (Reactive Nitrogen Species), which are the direct cause of the oxidative stress. Commonly, the two ubiquitous chemical species that are involved in these processes are peroxides and peroxynitrites [8]. Among the proteins able to regulate the peroxide tone in the cell, glutathione peroxidase (GPx) is an efficient system to reduce possible harmful substrates like H_2O_2 and hydroperoxides [9–11]. Its enzymatic mechanism can be described as three steps: first, one of the key residues in the catalytic pocket, the selenocysteine (Sec), is oxidized from its selenol form (E-Se-H) to selenenic acid (E-Se-OH) with the simultaneous reduction of the peroxide (Figure 1.4). The second step is the formation of selenenylsulfide intermediate (E-Se-SG) consuming one equivalent of glutathione (GSH). The recovery of the initial reduced selenol form is obtained by reaction with a second equivalent of GSH and the formation of GSSG. The fascinating part concerns the

comparison of this selenoenzyme to Cys-GPx, its sulfur-based mutant, which has a much lower enzymatic activity [12,13]. Unfortunately, a clear and unanimous explanation of the deprecated performance with the change of the chalcogen is not yet available.

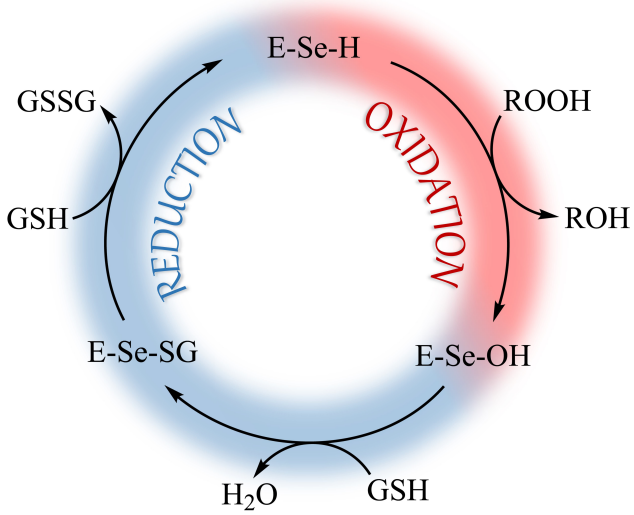

Figure 1.4. The three steps of the GPx mechanism for the reduction of a generic alkyl hydroperoxide ROOH to an alcohol ROH.

Obtaining some insights on the first step of the enzymatic mechanism of Cys-GPx and Sec-GPx (oxidative step) is the central part of Chapter 6. In Chapter 7, we have also tried to generalize, to some extent, what we have learnt from GPx to three other enzymatic families, which can reduce peroxides but are not necessarily involved in the control of the oxidative stress.

The selective antioxidant action can also be provided by small organic molecules acting as antioxidants or more specifically, as radical scavengers. Some examples are flavonoids and in particular, anthocyanins (pigments of many flowers and fruits) or specific molecules such as melatonin, serotonin, ascorbic acid (vitamin A), carotenoids (vitamin C), curcumin and many others of artificial origin including drugs like zolpidem and fluoxetine. The advantage of such small molecules is their easier characterization and therefore their subsequent

development in order to modify their properties, increase their effectiveness or reduce their side effects. Even the smoothest industrial synthesis is something not to be overlooked. The majority of the supplements and drugs are small molecules with a molecular weight inferior to 900 Dalton (the average value is between 100 Da and 500 Da). The accurate assessment of the antioxidant activity is a considerable challenge both from the theoretical and experimental point of view. This challenge mainly resides in the fact that the physiological and lipidic environment, typical of an organism, are complex matrices. Moreover, the high number of potentially quenching mechanisms to deactivate a radical, and the presence of structurally different ROSs further complicates the whole.

In Chapter 5 of this thesis, we will evaluate in silico the antioxidant activity of phenothiazine and its selenium and tellurium derivatives (Figure 1.5 A) trying to exploit what nature teaches us with GPx and, in particular, the advantages that selenium (and by extrapolation, tellurium) have against the most common and light chalcogens such as sulfur.

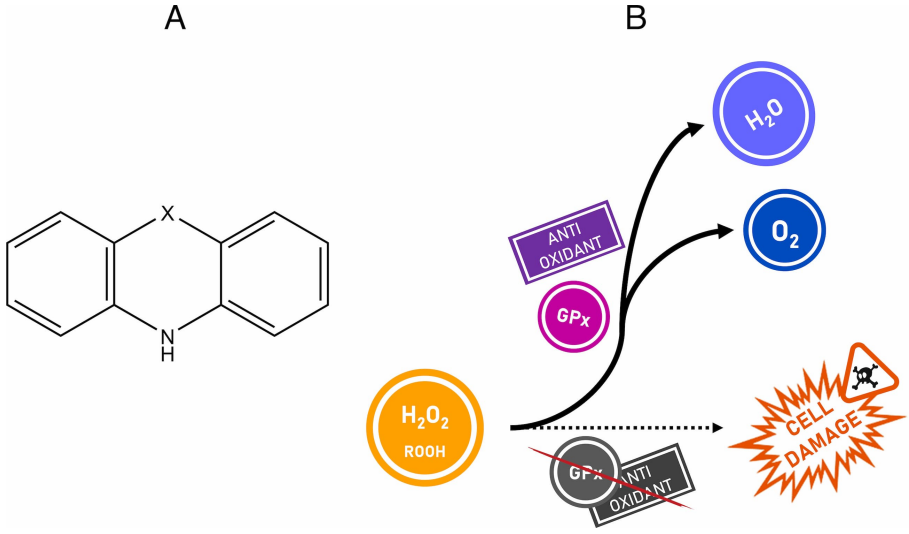

Figure 1.5. A) Powerful antioxidant scaffolds: phenothiazine (X=S). phenoselenazine (X=Se) and phenotellurazine (X=Te). B) Several enzymes

(GPx, OxyR, Prx, etc.) and small antioxidant molecules fight against the continuing oxidative stress condition in order to protect the living cells.

All the different topics described in this thesis have in common catalysis and the presence of redox reactions, and the aim of the whole work was to extract from important and thoroughly investigated cases as general as possible outcomes, which may be valuable, in the future, for those who will come.

I really hope you find it as intriguing as it was for me.

2 Theory and methods

In this thesis, very different systems will be modelled. From the smallest molecular systems (such as inorganic catalysts) to the largest ones (enzymes), the density functional theory (DFT) will be used as the primary working approach. The studied cases, because of their different size and nature, will be handled at different levels of theory which will be explained in the following chapters.

2.1 Density Functional Theory

During the first half of the XX century, the inadequacy of classical theories to describe increasingly microscopic systems became unpleasantly apparent. It was precisely in these years, especially from 1930 onwards, that the dawn of a new era was marked, where classical mechanics, based on continuous physics, was gradually seen as a macroscopic approximation of quantum one. Among the most important pioneers of this new branch, we can find Max Planck, Albert Einstein, Niels Bohr, Louis de Broglie, Max Born, Werner Heisenberg, Wolfgang Pauli, Erwin Schrödinger and, more lately, Richard Feynman.

A name not mentioned in the previous list but undoubtedly worthy of a separate remark is Paul Dirac: despite his rather peculiar temperament, he was able to reconcile the dictates of quantum mechanics with general relativity, and he is considered one of the greatest physicists of the last century. He is universally recognized as the father of relativistic quantum mechanics. On April 1929 he wrote: [14]

> *"The underlying physical laws necessary for the mathematical theory of a large part of physics and the whole of chemistry are thus completely known, and the difficulty is only that the exact application of these laws leads to equations much too complicated to be soluble. It therefore becomes desirable that approximate practical methods of applying quantum mechanics should be developed, which can lead to an explanation of the main features of complex atomic systems without too much computation."*

This concept, which remains still extremely relevant today, is based on the fact that although we could in principle describe a massive molecular system, the final problem is not necessarily easy to solve. In the particular case of the DFT, it was necessary to wait until the 1960s in order to have a more versatile alternative rather than solving an approximate form of the Schrödinger equation with a more direct approach, such as Hartree-Fock or post Hartree-Fock.

Density Functional Theory (DFT) methods are based on the first and the second Hohenberg-Kohn principles [15] dated back to 1964. The first one proves the direct and unique relationship between the total energy (formally presented as external potential $v(\vec{r})$ in literature) and

a given electron density $\rho_v(\vec{r})$. This can be simply described as the following one-to-one mapping (Eq. 2.1):

$$v(\vec{r}) \leftrightarrow \psi_v^{gs} \leftrightarrow \rho_v(\vec{r}) \tag{2.1}$$

The second theorem (Eq. 2.2) affirms the possibility of minimizing the total energy using the variational formalism: the functional that returns the ground state of the system strictly generates the lowest energy if and only if the electronic density in input has been derived from the real ground state.

$$E_v^{gs} \leq E_v[\rho(\vec{r})] \equiv \left\langle \psi[\rho(\vec{r})] \middle| \hat{H} + \hat{V} \middle| \psi[\rho(\vec{r})] \right\rangle \tag{2.2}$$

The implications of these theorems are very powerful from a theoretical point of view, but no practical tools were available to define any property of the fundamental state, even for a simple system. Only one year later, in 1965, the practical implementation of the two theorems was described in what is called Kohn-Sham's equation (KS) [16], which is a useful reformulation of Schrödinger's many bodies formalism as we can see from Eq. 2.3.

$$\left(-\frac{\hbar}{2m} \nabla^2 + v(\vec{r}) \right) \varphi_i(\vec{r}) = \varepsilon_i \varphi_i(\vec{r}) \tag{2.3}$$

Solving this eigenvalue equation, using a KS wave function defined as a single Slater determinant, provides the energy ε_i of all Kohn-Sham orbitals φ_i which are directly connected to the electron density through Eq. 2.4.

$$\rho(\vec{r}) = \sum_{i}^{N} |\varphi_i(\vec{r})|^2 \qquad 2.4$$

In principle, compared to wave function-based techniques, DFT is formally an exact approach, without any sort of approximation, where the correlation energy is naturally taken into account. Unfortunately, on the other hand, the exact form of the exchange-correlation (XC) functional, used to create the conceptual bridge between the total energy and the electron density, is unknown (except for trivial cases, such as the free electrons Fermi gas [17–19]). A widely used approach is the local-density approximation (LDA), in which the functional is only dependent on the density at the coordinate values where the functional is evaluated. More modern ways of approaching the exact formulation of the XC functional, such as generalized gradient approximations (GGA), have been developed later on. These are still local, but they also take into account the density gradient. The evolution of XC functionalities has not stopped and continues today, trying to get closer and closer to the highest step of the famous DFT Jacob's ladder.

Nowadays, the availability of supercomputers has made possible the study of molecular systems, some of which are rather complex/extended, through the use of increasingly advanced techniques but, in spite of that, the use of electron density in DFT techniques dramatically simplifies the description of the system compared to other wave function-based methods such as Møller-Plesset (MPx) perturbation theory, multi-configurational SCF approaches (MCSCF) or coupled clusters (CC). Besides, DFT has better scaling behavior with a negligible accuracy loss.

2.2 Activation strain model (ASM)

Characterizing the nature of a chemical bond by analyzing how the energy barrier for its formation arises is a primary key to deeply understand any reaction deeply. To this purpose, the activation strain model (ASM), also known as distortion/interaction model [20], is a fragment-based approach to easily understand chemical reactions and the associated barriers [21–24]. This approach, already used in the 70s by Morokuma [25] and Ziegler [26], relies on the idea that the two separate reactants, which approach from an infinite distance, begin to interact and deform. In this model, the total energy ΔE is decomposed into the sum of strain energy ΔE_{strain} and the interaction one ΔE_{int} (Eq. 2.5):

$$\Delta E = \Delta E_{strain} + \Delta E_{int} \tag{2.5}$$

Usually, the total strain ΔE_{strain} is a positive value and can also be divided into contributions stemming from each of the reactants. The remaining negative contribution derives from electronic interactions and can be itself split as well through the energy decomposition analysis (EDA) [24] explained in the next section (Eq. 2.7). ASA and EDA are generally applied to the three leading structure involved into an elementary step: starting reactants, transition state (TS) and the final product but a further extension along the reaction coordinate (ζ) is also feasible. Commonly, after locating and optimizing the first-order saddle point structure, the non-equilibrium points are retrieved from the minimum energy path (MEP) in both directions using the intrinsic reaction coordinate (IRC) approach. The use of nudged elastic band (NEB) is also possible: this has the advantage that the TS is not necessary, but only reagents and products are required as initial input.

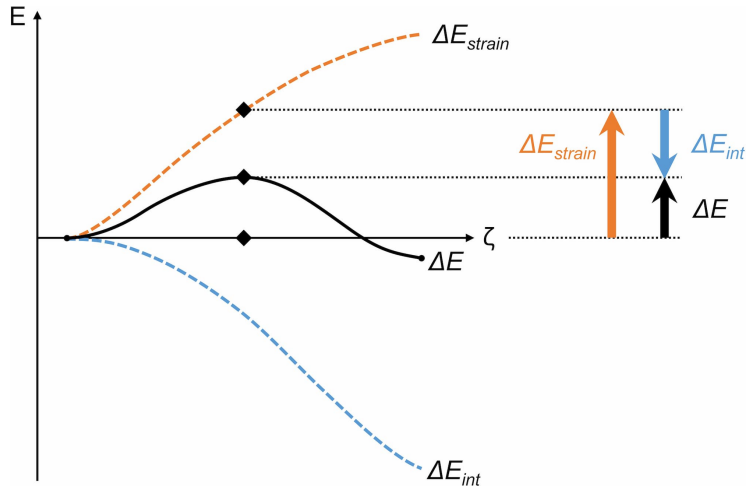

Figure 2.1. ASA applied to a general elementary reaction.

Another important extension to ASM has been proposed by Fernandez et al. [27] with the aim of taking into account unimolecular reactions. This situation is encountered in the present study (Chapter 3). In this case, the activation barrier is given as the *change*, upon going from educt to TS, in strain within the two fragments plus the *change*, upon going from educt to TS, in the interaction between these two fragments (Eq. 2.6):

$$\Delta E = \Delta\Delta E^{\ddagger}_{strain} + \Delta\Delta E^{\ddagger}_{int} \qquad 2.6$$

2.3 Energy decomposition analysis (EDA)

ΔE_{int} can be further analyzed in the framework of the Kohn-Sham molecular orbital (MO) model using a quantitative decomposition of the bond into electrostatic interaction (ΔV_{elstat}), Pauli repulsion (ΔE_{Pauli}), called also exchange repulsion or overlap repulsion, (attractive) orbital interactions (ΔE_{oi}) and dispersion contributions (ΔE_{disp}) (if dispersion is included in the functional).

$$\Delta E_{int} = \underbrace{\Delta V_{elstat} + \Delta E_{Pauli}}_{\Delta E_{steric}} + \Delta E_{oi} + \Delta E_{disp} \qquad 2.7$$

Each term has a physical-chemically meaningful explanation. To apply ASM, the system is ideally divided into two fragments, typically two reactants. These fragments approach and overlap, but they are not allowed to interact with each other: by doing so, only a purely electrostatic interaction, i.e. an attractive potential ΔV_{elstat} (with a quasi-classically Coulombic form), is calculated. It is designed to quantitatively estimate the electrostatic bonding contributions which are neglected in a purely orbital-interaction based analysis. Then, the wavefunctions are allowed to overlap, but this implies an anti-symmetrization step that increases the total energy: this destabilizing term, called ΔE_{Pauli} derives directly from the Pauli exclusion principle, where repulsion effects between the filled orbitals are considered. Electrostatic and Pauli contributions are often summed together to define an overall steric ΔE_{steric} term. Lastly, contributions related to attractive interactions from empty orbitals of a fragment and the filled (or partially filled) ones of the other fragment, are embedded into a stabilizing orbital interaction term ΔE_{oi}. The calculation is performed when fragments orbitals are allowed to relax with a natural electrons redistribution to achieve the final state in the entire complex. Charge transfer and mixing effects, when the two reactants approach to form the complex, are included into this latter term. Generally, classical DFT functionals neglect any form of long range non covalent interaction but, nowadays, dispersion forces can be taken into account with several corrections: actually, one of the most used is the correction D3(BJ) by Grimme [28] (for the van der Waals-like term) and Becke-Johnson [29] (for the damping function). Unless otherwise stated, the term ΔE_{disp} has been excluded in this work because of negligible dispersion effects in our systems.

2.4 Turnover Frequency (TOF) calculations

The turnover frequency (TOF) is a valuable parameter to better understand and characterize the analyzed catalytic cycle. In the beginning, it was conceived to describe enzymatic kinetics and biological promotor/inhibitor species, but the TOF concept can be extended to any cyclic reactions. The canonical definition of TOF is:

$$\mathrm{TOF} = \frac{N}{t} \tag{2.8}$$

where t is the total time required to perform N cycles or to create N molecules of product. A modern approach aiming at translating thermodynamic data into kinetics is the definition of the energy span [30], as the difference between the energy of the highest energy transition state and the energy of the lowest intermediate, to establish a relation between the classical Arrhenius equation and the Boltzmann distribution. Unluckily, this formulation gives exact results only when the energy of the starting reactants lies at the same energy level of the final products, i.e. $\Delta G_r^\circ = 0$. Kozuch and Shaik proposed a more general model for calculating the TOF, based on Christiansen's idea [31]: they defined the turnover frequencies directly in terms of kinetic constants summations. By implementing the Eyring transition state theory (TST) with the Eyring-Polanyi equation:

$$k = \frac{k_b T}{h} e^{\frac{-\Delta G^\ddagger}{RT}} \tag{2.9}$$

where k_b is Boltzmann's constant, T the temperature, h Planck's constant and R is the universal gas constant, they succeeded in deriving the expression 2.10 [32]:

$$\mathrm{TOF} = \frac{k_b T}{h} \frac{e^{\frac{-\Delta G_r}{RT}} - 1}{\sum_{i,j=1}^{N} e^{(T_i - I_j - \delta G_{i,j})/RT}} = \frac{\Delta}{M} \qquad 2.10$$

where

$$\delta G_{i,j} = \begin{cases} \Delta G_r & if \quad i > j \\ 0 & if \quad i \leq j \end{cases} \qquad 2.11$$

T_i and I_j indicate the Gibbs free energies of the i$^{\text{th}}$ transition state and j$^{\text{th}}$ intermediate, respectively. Eq. 2.10 has a strong analogy with Ohm's first law: TOF is a reactants/products flux (in analogy with current intensity), Δ is analogous to the electric potential difference, and M can be interpreted as a resistance due to reactants flux. Importantly, in this model, the energy differences between all intermediates and all transition states are considered. In fact, the denominator is a summation of N^2 exponential terms for each index permutation. The numerator overcomes the limitation above mentioned, since, ΔG_r is the difference between the free energies of the products and of the reactants. In the overall, all the elementary steps of the catalytic cycle are included in the definition of the TOF, and so the rate-determining step (RD step) concept fades into the rate-determining states (RD states) concept, which represents a flexible and accurate way to analyze the efficiency of a cyclic process. This model relies on three assumptions:

I. Eyring TST is used.

II. Bodenstein's approximation, better known as steady state regime, must be valid.

III. All stationary points undergo fast thermal equilibration with their surroundings.

In many catalytic cycles, Eq. 2.10 can be simplified by:

I. neglecting the "-1" term in the numerator: it is merely introduced to avoid thermodynamic inconsistencies for endergonic (TOF<0) or close-to-equilibrium reactions (TOF=0). This term becomes unimportant in exergonic cycles.

II. limiting the denominator to a single exponential term: only the term that involves the two TOF determining states is dominant and must be retained in the expansion; all the rest becomes negligible.

On this basis, Eq. 2.10 can be rewritten as:

$$\begin{aligned} \mathrm{TOF} &\approx \frac{k_b T}{h} e^{(I_{TDI} - T_{TDTS} - \delta G_{TDI,TDTS})/RT} \\ &= \frac{k_b T}{h} e^{-\delta E/RT} \end{aligned} \qquad 2.12$$

where I_{TDI} and T_{TDTS} are the Gibbs free energies of the TOF determining intermediate (TDI) and TOF determining transition state (TDTS), respectively. δE is called *energy span.*

The identification of the TDI and the TDTS in a catalytic cycle is based on an elegant technique which determines the variations of TOF in direct relation with the energy variation of one TS/intermediate. In analogy with the definition of degree of rate control, Kozuch and Shaik derived Eq. 2.13 [32]:

$$X_{RC,i} = \frac{k_i}{r}\left(\frac{\partial r}{\partial k_i}\right)_{k_{i\neq j},K} \rightarrow X_{TOF,i} = \left|\frac{1}{TOF}\frac{\partial TOF}{\partial E_i}\right| \qquad 2.13$$

where r is the overall reaction rate and k_i is the constant rate for the ith step. The identities of Eq. 2.13 are:

$$X_{TOF,T_i} = \frac{\sum_{j=1}^{N} e^{(T_i - I_j - \delta G_{i,j})/RT}}{\sum_{i,j=1}^{N} e^{(T_i - I_j - \delta G_{i,j})/RT}} \quad 2.14$$

$$X_{TOF,I_j} = \frac{\sum_{i=1}^{N} e^{(T_i - I_j - \delta G_{i,j})/RT}}{\sum_{i,j=1}^{N} e^{(T_i - I_j - \delta G_{i,j})/RT}} \quad 2.15$$

The bigger the degree of TOF control (X_{TOF}), the highest the impact of the energy variation of the considered state for TOF. With this mathematical strategy, both TDI and TDTS are quickly identified for a particular catalytic cycle.

It is important to stress that RD step theory fails to predict a few delicate but essential aspects that rule the efficiency of a catalyst. An example is the presence in the cycle of some very low energy species: the resulting effect is the quenching of the catalyst (trapped in a potential well) with a dramatic drop in terms of activity. RD step approach does not describe these situations adequately because it is focussed on the so common “highest limiting barrier” or “lowest kinetic rate step” concepts.

In principle, all the energies in Eq. 2.9-2.15 must be Gibbs free energies. Since our purpose is comparing different catalysts with an identical mechanism, the TOF ratio is a meaningful value. In fact, it benefits from a significant error compensation and electronic energies can be used, since entropic contributions are likely very similar in analogous mechanisms [33].

2.5 QM-ORSA Protocol

The antioxidant capability of a molecule is somewhat difficult to defined in a formal and rigorous way. However, in many cases it is essential to compare and classify different molecules or drugs in order to

subsequently locate the main components from which the antioxidant effect originates. This is one possible approach to better understand how antioxidant molecules works and thus develop, via a rational design, molecules with improved antioxidant capabilities. In chapter 5, we have the necessity to evaluate precisely this characteristic, both qualitatively and quantitatively, of some selected molecules.

Galano and coworkers developed the QM-ORSA protocol to make up for this lack and evaluate the quenching capabilities of molecules toward different reactive oxygen species (ROS) [34]. Nowadays, the method is a reference for this field and it has been successfully used many times in literature also finding a good approval from an experimental point of view.

The method consists firstly in an evaluation of the barrier for a given reaction with a canonical TS minimization on a first-order saddle point, and, in the case of an electron transfer (ET), the Gibbs free energy of activation is calculated invoking the Marcus theory [35,36] through the relation in Eq. 2.16:

$$\Delta G_{ET}^{\ddagger} = \frac{\lambda}{4}\left(1 + \frac{\Delta G_{ET}^{0}}{\lambda}\right)^{2} \qquad 2.16$$

Where the nuclear reorganization energy λ is approximated as:

$$\lambda \approx \Delta E_{ET} - \Delta G_{ET}^{0} \qquad 2.17$$

The Eq. 2.17 has been used several times by Nelsen and coworkers [37,38] for many reactions and it's a simple way to nicely estimate λ. ΔE_{ET} is the (nonadiabatic) difference in energy between reactants and vertical products. Before the conversion of activation energies in reaction rates, two thermal corrections must be applied: the first one is the conversion from the gas phase (1 atm, 298.15K) to the condensed standard state (1 M, 298.15K) via Eq. 2.18:

$$\Delta G^{1M} = \Delta G^{1atm} - RT\ ln(V_M) \tag{2.18}$$

This results in lowering all the ΔG of 1.89 kcal mol^{-1} for a bimolecular reaction, at 298.15K. The second important correction is used to take into account the solvent cage effects. The latter is intended to better estimate the reduced entropy loss for a transition state formation due to the solvation effects. The free volume correction for the condensed phase by Benson [39] has been used:

$$\Delta G^{sol} \cong \Delta G^{gas} - RT\{ln[n10^{2(n-1)}] - (n-1)\} \tag{2.19}$$

The conversion lowers all the ΔG of 2.55 kcal mol^{-1} for a bimolecular reaction, at 298.15K. Ignoring these two corrections can lead to a strong underestimation of the final kinetic rate constants, up to 1800 times. Finally, the rate constants (k) have been calculated within the Transition State Theory (TST) model with the Eyring-Polanyi equation [40,41]:

$$k = \frac{k_B T}{h} e^{-\frac{\Delta G^{\ddagger}}{RT}} \tag{2.20}$$

However, this is not the final rate constant because many reactions are so fast that the process is limited by diffusion and the sole thermal rate constant is no longer a good prediction of the real reaction rate. To solve this issue, the Smoluchowski equation for steady-state solutions [42] (Eq. 2.21) in combination with the Stokes-Einstein [43,44] equation (Eq. 2.22) has been used to calculate the diffusion rate constant:

$$k_D = 4\pi R_{AB} D_{AB} N_A \tag{2.21}$$

R_{AB} is the reaction distance: commonly, the distance between the donor and the acceptor moieties is used. However, this is tricky for particular

reactions such as an electron transfer in which there is no nuclei displacements. In the latter case, the sum of the two interacting fragment radii (vdW or from molar volume) is a good approximation of R_{AB}. D_{AB} is the mutual diffusion coefficient of the ROS (A) and the scavenger (B). It is simply given by the product of the single D_A and D_B [45].

$$D_{A\ or\ B} = \frac{k_B T}{6\pi\eta a_{A\ or\ B}} \qquad 2.22$$

η is the viscosity of water ($8.91 \cdot 10^{-4}$ Pa s) or pentyl ethanoate ($8.62 \cdot 10^{-4}$ Pa s). The former solvent is used to emulate physiological conditions, the latter instead mimics a lipid environment. a_A and a_B is the Stokes radius of A and B, respectively.

Accordingly to the Collins-Kimball theory [46], both the thermal (k) and diffusion (k_D) rate constants are coupled together to form the total rate coefficient:

$$k^{app} = \frac{k_D k}{k_D + k} \qquad 2.23$$

The overall rate coefficient is clearly the sum of k^{app} for every possible mechanism i that could occurs, taking into account any possible reaction path degeneracy σ:

$$k^{overall} = \sum_{i}^{N} \sigma_i k_i^{app} \qquad 2.24$$

Branching ratios (Γ) have been calculated as well, and they represent the contribution of a single mechanism to the overall antioxidant activity:

$$\Gamma_i = \frac{100\ k_i^{app}}{k^{overall}} \tag{2.25}$$

3 [2+2+2] Alkyne Cyclotrimerizations: The Key-Intermediates

Adapted from

M. Dalla Tiezza, F. M. Bickelhaupt, L. Orian

ChemPhysChem 2018, 19, 1766–1773

3.1 Introduction

Metallacycles are derivatives of carbocyclic compounds in which a metal atom replaces a carbon center. They are important reactive intermediates in catalytic processes. For example, they form in olefin metathesis reactions [47], and in alkyne cyclotrimerizations [48–51], or they are unwanted products resulting from ortho-metalation reactions [52].

Metallacycles can be easily classified on the basis of the ring size; four, five and six membered rings are the most common species, although heptacycles can also be encountered. Various metals are involved in their formation, among which, but not exclusively, Zr, Mn, Mo, Cr, Pt, Pd, Fe, Ru, Os, Re, Co, Rh, and Ir. Metallacyclopentadienes have the general formula $L_nM(CH)_4$ (L = ligand, M = metal) and are mostly formed through alkyne coupling at low valent metal centers, i.e., Ni(I) and Co(I) [53]. This reaction (oxidative coupling) is the first step in the process of [2+2+2] alkyne cycloaddition (Figure 3.2), for which a class of well-known catalysts are the fragments CpM (M=Co, Rh, Ir; Cp=$C_5H_5^-$) [54–56]. These catalysts, in which the ligand is the six-electron aromatic cyclopentadienyl anion, have intriguing electronic and structural properties. In fact, the coordination of the metal to the ring is not perfectly symmetric (η^5), but can be described as a distorted arrangement in which the five metal-carbon distances are not equal: two distances are shorter (M-C1 and M-C3) and two distances are longer (M-C1a and M-C3a), as shown in Figure 3.1 A. Typically, one carbon atom (C2) is found between those at a closer distance, which may be located below the ring plane, so that a folding angle $\gamma = 180 - \phi$ is observed (Figure 3.1 B). This tipped structure, described as $\eta^3+\eta^2$, is representative of the phenomenon known as metal slippage [57]. Further distortion can lead to an allylic coordination (η^3) and *in extremis* to the formation of a σ bond between the metal and one C atom (η^1). To quantify the amount of slippage, a parameter was introduced by Basolo and co-workers [58], defined in Eq. 3.1:

$$\Delta\ (\text{Å}) = \frac{(M-C1a + M-C3a) - (M-C1 + M-C3)}{2} \qquad 3.1$$

where M-C1a and M-C3a are the longest distances between M and two adjacent C atoms of the Cp ring and M-C1 and M-C3 are the distances between M and the C atoms adjacent to C1a and C3a, respectively. Even without defining rigorous ranges of values to classify the metal

hapticity, the amount of slippage can be efficiently quantified on the basis of Δ values, which go from 0 (η^5) to ~0.3 (η^3) till values larger than 0.6 (η^1).

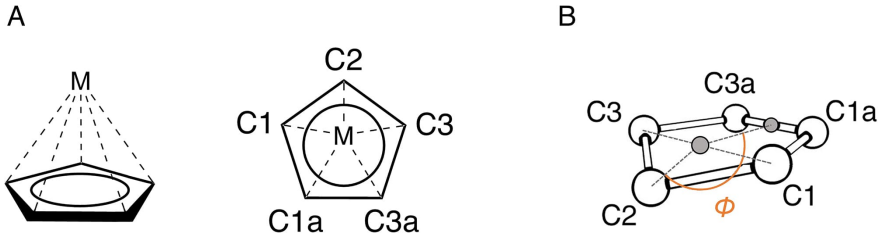

Figure 3.1. CpM (M=Co, Rh, Ir; Cp=$C_5H_5^-$) fragment: numbering scheme (A) and definition of the folding angle ($\gamma = 180 - \phi$).

The extent of metal slippage can be tuned by replacing the Cp moiety with larger aromatic ligands such as indenyl or such as indacenyl anions [59–62].

CpCo catalyzed [2+2+2] co-cycloadditions to produce pyridines from alkynes and nitriles are reported in the pioneering experimental studies by Wakatsuki and Yamazaki [63] and by Bönnemann [64,65]. For many years, Co-based catalysts stayed on the top in terms of efficiency [3,63–67]. An extension to group 9 elements, in particular to Rh, was initially proposed by Booth et al. [68] and Ingrosso et al. [69] They used numerous different Rh(I) half-sandwich complexes to investigate how to trim and optimize selectivity and the overall cyclotrimerization yield.

Metal slippage and its relation with molecular properties and reactivity have been extensively studied theoretically in half-sandwich Rh(I) derivatives [33,56,70]. The catalytic use of CpM fragments in acetylene [2+2+2] cyclotrimerization to benzene and alkyne/nitrile [2+2+2] cycloaddition to pyridine has been investigated also *in silico* for different metals: Co [71,72], Rh [56,73], Ir [74,75] and Ru [55]. These computational mechanistic studies have revealed that the oxidative coupling of two acetylene molecules coordinated to a group 9 metal (M=Co, Rh, Ir) to form the metallacyclopentadiene (Figure 3.2) has the

highest activation energy of the whole cycle; in the case of several Rh-based catalysts, this elementary step, was found TOF (Turn-Over Frequency) determining. Thus, a thorough analysis of the structural and electronic properties of CpM1, CpM2 and TS(CpM1,CpM2), which denote the bis-acetylene precursors, the metallacyclopentadiene and the transition state in between, respectively, is desirable in order to gain deeper insight and more general principles for a rational design of these catalysts (Figure 3.2). In particular, no rigorous explanation has been found yet for the more favorable energetics reported for CpCo fragment [54,71] than CpRh and CpIr fragments in [2+2+2] alkyne cyclotrimerizations.

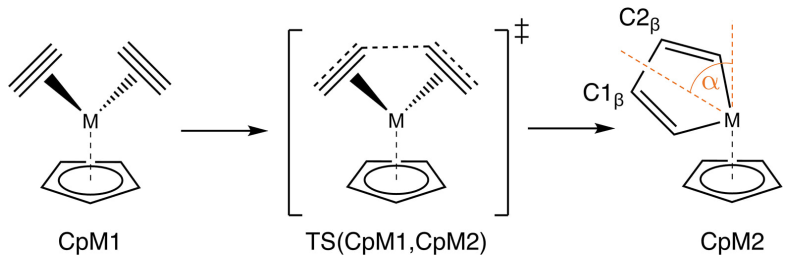

Figure 3.2. Oxidative coupling: formation of a metallacyclopentadiene (CpM2) from a bis acetylene precursor (CpM1). The tilt angle α is shown in CpM2 (M=Co, Rh, Ir).

In the following chapter, the formation of the metallacyclopentadiene was thoroughly explored *via* the intramolecular oxidative coupling of the bis-acetylene precursor containing the group-9 metal (CpM1) for three different cases: cobalt, rhodium and iridium. Apart from the energy profiles, the reasons for the diversified catalytic efficiency are traced to the structural and electronic properties featured by the different metals.

3.2 Methods

All density functional theory (DFT) [15,16,76] calculations were performed with the Amsterdam Density Functional (ADF) program [77–79]. Scalar relativistic effects were accounted for using the zeroth-

order regular approximation (ZORA) [80]. The BLYP [81,82] density functional was used, in combination with the TZ2P basis set for all elements. The TZ2P basis set is a large uncontracted set of Slater-type orbitals (STOs). It is of triple-ζ quality and has been augmented with two sets of polarization functions on each atom: 2p and 3d in the case of H, 3d and 4f in the case of C and N, 4p and 4f in the case of Co, 5p and 4f in the case of Rh, 6p and 5f in the case of Ir. The frozen-core approximation was employed: up to 1s for C and N, up to 2p for Co, up to 3d for Rh and up to 4d for Ir. This level of theory is denoted in the text: ZORA-BLYP/TZ2P.

Equilibrium and transition-state geometries were optimized under C_s symmetry constraint using analytical gradient techniques. All structures were verified by frequency calculations: for minima, all normal modes have real frequencies, whereas transition states have one normal mode with an imaginary frequency. The character of the normal mode associated with the imaginary frequency was analyzed to ensure that the correct transition state was found.

3.3 Results and discussion

Metallacycles are frequently postulated as intermediates in catalytic cycles. The investigation started with a search in the Cambridge database (CSD) [83] of compounds with the $CpM(CH)_4$ (M=Co, Rh, Ir) moiety. Eight crystallographic structures containing the unit $CpCo(CH)_4$, six structures containing the unit $CpRh(CH)_4$ and seven structures containing the unit $CpIr(CH)_4$ are present. In all, except one Ir compound, there is an additional ligand bonded. In fact, CpM2 structures are coordinatively unsaturated 16-electron species, and the presence of an extra ligand ensures that the 18-electron rule is satisfied. On the other hand, this vacancy is fundamental in the catalytic [2+2+2] cyclotrimerization because it favors the coordination of the third acetylene or another unsaturated molecule used to build the cyclic product.

Among these crystallographic structures of metallacyclopentadienes, particular attention should be given to those structures closer to our model systems, i.e. $Cp^*M(CH)_4PPh_3$ (Cp^*=1,2,3,4,5-pentamethylcyclopentadienyl anion) that are labeled BODJUZ [84] and CPBYCO [85] for Co, GOKGIW [86] and PBUDRI10 [87] for Rh, and GOKGOC [86], GOKGUI [86] and MPBYIR10 [87] for Ir. Significant interatomic distances and angles are shown in Addendum (Table S 3.1). An increase of Δ values from Co to Ir may be noticed, in agreement with our calculated relaxed geometries that show an analogous trend.

Overall, a nice agreement between the calculated and experimental structures has come to light when comparing metal-carbon and carbon-carbon interatomic distances. A peculiar structural feature of these metallacycles is the tilted orientation of the cycle with respect to the Cp plane (Figure 3.2). This tilting, has been demonstrated by for $CpRh(CH)_4$ [56] and it is explained on the basis of Woodward-Hoffman rules which predict two equivalent tilted structures with tilt angle α and $-\alpha$, respectively, connected by a TS in which the five-membered metallacycle is oriented in an orthogonal fashion with respect to the Cp plane. The tilting is enhanced in the crystallographic structures likely due to the presence of the extra ligand.

A benchmark study was done on the CpM2 complexes to evaluate the relative stability of the singlet and triplet states. Geometry optimizations were carried out for the singlet (^{1}CpM2) as well as for the triplet ground state (^{3}CpM2) of CpCo2, CpRh2, and CpIr2 at different levels of theory (Table 3.1). The relative stability of the singlet and triplet state in these compounds is a long-standing debate. Earlier studies [71,74,75,88–91] all agree that CpCo2 and CpIr2 are more stable in the triplet state. Conversely, the closed shell configuration is found more stable for the rhodacycle system [56,92,93]. In Table 3.1, the energy difference between singlet and triplet state is consistent at all levels of theory for CpCo2 and CpRh2. In the case of CpIr2, the singlet-

triplet states are relatively close in energy. In this case, the correct order of the states is obtained only when BLYP is used, while other GGA and hybrid functionals show a stabilization, albeit weak, of the singlet state. This supports our choice of ZORA-BLYP/TZ2P, which was previously documented for Rh(I) complexes by several other works [33,56,62,70,73].

Table 3.1 Energy of the $CpM(CH)_4$ metallacycles triplet relative to the singlet state computed with various XC functionals[a].

XC Functional	ΔE (kcal mol^{-1})		
	CpCo2	CpRh2	CpIr2
BLYP	-8.97	2.57	-0.72
OLYP	-8.12	4.28	0.63
OPBE	-5.37	4.84	0.69
B3LYP	-16.53	4.15	1.00
S12g	-4.50	4.59	1.00

At this level of theory, the Co and Ir metallacycles are more stable in the triplet state by 8.97 and 0.72 kcal mol^{-1}, respectively. On the other hand, the rhodacyclopentadiene is more stable in its singlet state with the triplet state being 2.57 kcal mol^{-1} higher in energy. This implies that in the former cases the catalytic cycle of the [2+2+2] acetylene cyclotrimerization requires a change to the triplet potential energy surface (PES) and at a later stage of the catalytic mechanism a return to the singlet PES, as previously reported by Dahy et al. [71,74]. Conversely, CpRh catalyzed [2+2+2] acetylene cycloaddition takes place exclusively on the singlet PES.

After computing the TS structures of the three oxidative couplings, the IRC (intrinsic reaction coordinate) profiles were calculated; they are shown in Figure 3.3. The IRC has been projected onto a reaction coordinate that is defined (Eq. 3.2) as the difference

[a] In all computations the TZ2P basis set was used.

between the average of the two Cβ–M distances and the length of the bond between the β carbons (C1β–C2β), which are shown in Figure 3.2:

$$RC = \frac{(C1_{\beta}\text{–}M) \; + \; (C2_{\beta}\text{–}M)}{2} \; - \; (C1_{\beta}\text{–}C2_{\beta}) \qquad 3.2$$

This allows a good description of the reaction on both sides of the transition state: the first term is the critical geometry parameter for the structural transformations on the right side of the reaction, which is from the TS to the metallacycle. The second term, i.e. the distance C1β–C2β, properly describes the left side of the reaction, i.e. from the bis-acetylene precursor to the TS, while it remains almost unchanged on the right side, i.e. from TS to the metallacycle, because the C1β–C2β bond has been formed already.

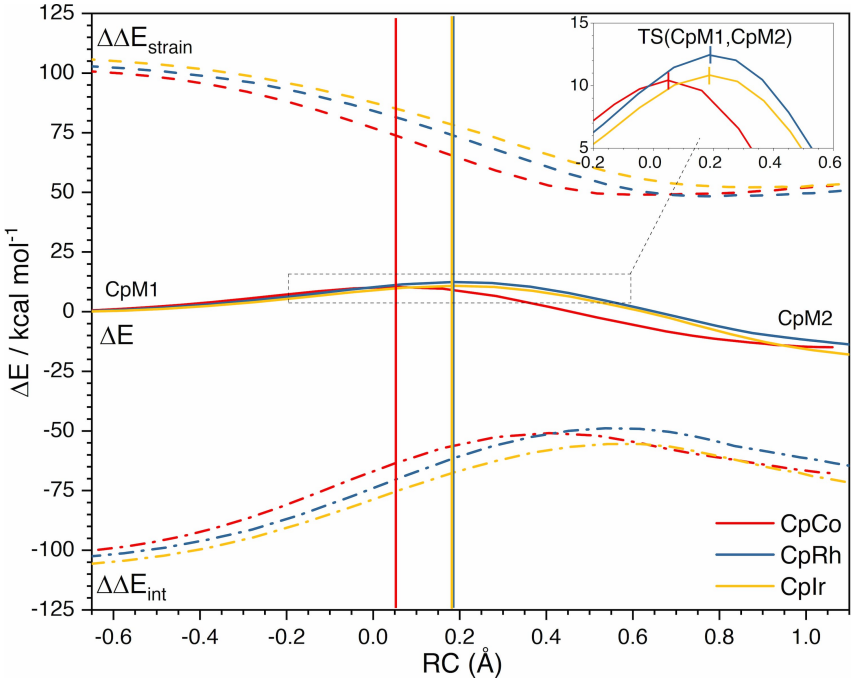

Figure 3.3. ASA along the IRC of the oxidative coupling catalyzed by CpCo, CpRh and CpIr fragments; level of theory ZORA-BLYP/TZ2P.

Table 3.2. Energy values (kcal mol^{-1}) of CpM1[b], CpM2 and TS(CpM1- CpM2) (M=Co, Rh, Ir)[c].

	ΔE	$\Delta\Delta E_{strain}$	$\Delta\Delta E_{int}$	$\Delta\Delta E_{Pauli}$	$\Delta\Delta V_{elstat}$	$\Delta\Delta E_{oi}$
CpCo1	-	101.46	-101.46	284.17	-170.18	-215.45
TS(CpCo1,CpCo2)	10.42	74.13	-63.71	290.44	-164.97	-189.18
CpCo2	-14.90	52.78	-67.68	219.20	-124.98	-161.90
CpRh1	-	103.02	-103.02	336.18	-205.04	-234.16
TS(CpRh1,CpRh2)	12.44	73.80	-61.36	357.25	-207.34	-211.27
CpRh2	-18.26	56.16	-74.42	251.81	-153.69	-172.54
CpIr1	-	106.33	-106.33	462.16	-275.57	-292.92
TS(CpIr1,CpIr2)	10.84	78.12	-67.28	493.92	-286.70	-274.50
CpIr2	-22.65	55.69	-78.34	349.42	-219.74	-208.02

[b] For CpM1, ΔE=0, while $\Delta\Delta E_{strain}$ and $\Delta\Delta E_{int}$ (and the $\Delta\Delta E$ contributions resulting from EDA) are simply the ΔE_{strain} and ΔE_{int} relative to separate reactants, i.e. the CpM fragment and two acetylene molecules.

[c] Computed at ZORA-BLYP/TZ2P.

At a glance, it is evident that the energetics are in favor of the CpCo fragment, while CpRh is the less efficient catalyst, having the highest barrier. Since this oxidative coupling has the highest barrier in the whole cycle, this prompted us to investigate in detail those factors that affect its formation and its height. Activation strain analysis was then performed referring to the fragments CpM (catalyst) and two acetylene molecules ([2(C_2H_2)], substrate). The ground state of the CpM fragment is a triplet for all group 9 metals; so, the excitation energy (ΔE_{exc}) required to prepare each acetylene molecule in a suitable electronic configuration must be taken into account. To this purpose, the imposed C_s symmetry was useful. Since the formation of $CpM(CH)_4$ from the bis-acetylene precursor $CpM(C_2H_2)_2$ is a unimolecular reaction, the analysis can be done considering ΔE as the *change*, upon going from educt to TS, in strain within the two fragments plus the *change*, upon going from educt to TS, in the interaction between these two fragments, which are indicated as $\Delta\Delta E_{strain}$ and $\Delta\Delta E_{int,}$ respectively (Figure 3.3 and Table 3.2). In addition, in this specific case, ASA and EDA were carried out, as explained in the computational methodology, by choosing CpM and [2(C_2H_2)] fragments in triplet configuration. Note that this requires that spin-polarization is taken into account in the computation of ΔE_{int}, more especially, in ΔE_{oi}, in order to obtain accurate an energy decomposition analysis (EDA) that correctly accounts for the differences when changing the metal center [24,94].

In order to apply this concept, we have analyzed the bonding between CpM and the two coordinated acetylene molecules focusing on the frontier molecular orbitals. The CpM fragment has a ground state with one electron in a 4d-derived orbital of A'' symmetry (HOMO-1) and one electron in a 4d-derived orbital of A' symmetry (HOMO) (Figure 3.4 A).

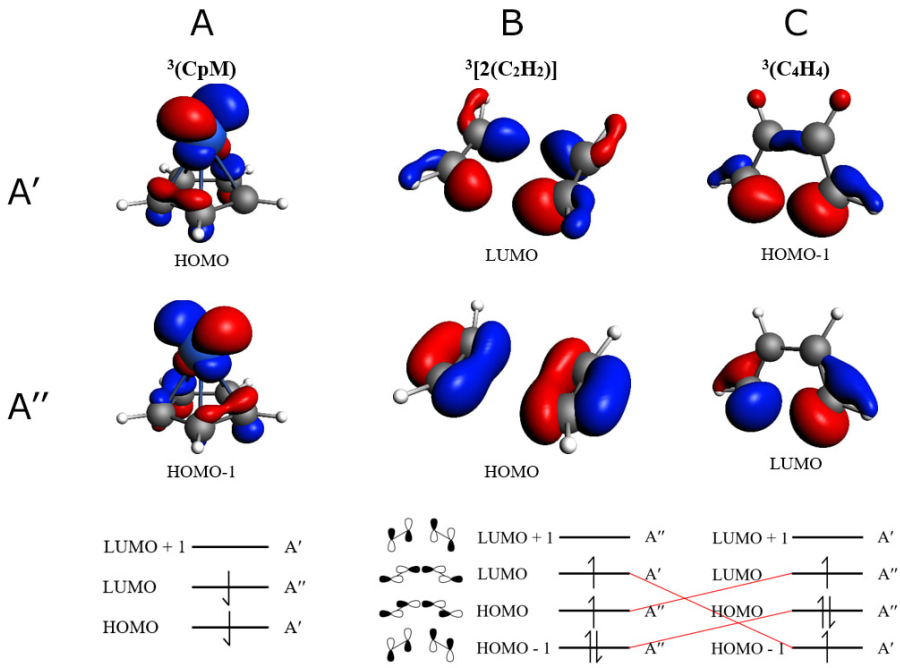

Figure 3.4. Frontier MOs of the two main fragments CpM (A) and [2(C$_2$H$_2$)] in CpM1 (B) and in CpM2 (C), respectively; the tilted geometry of CpM2 can be explained by taking into account the most favorable overlap between CpM and C$_4$H$_4$ orbitals

The ground state of CpM corresponds to its valence state in the overall complex. Conversely, in the bis-acetylene fragment (Figure 3.4 B) of CpM1, an electron from the HOMO (A'' symmetry) has to be excited to the LUMO (A' symmetry) to turn into the appropriate valence state for bonding with CpM and form CpM1. Finally, the MOs of the [2(C$_2$H$_2$)] fragment in its excited valence configuration are also shown for CpM2 (Figure 3.4 C); in this case, the fragment is better labeled as C$_4$H$_4$.

In Figure 3.3, the strain and interaction contributions are plotted along the reaction coordinate for the three oxidative couplings. The differences in $\Delta\Delta E_{strain}$ among the complexes are mainly due to the [2(C$_2$H$_2$)] fragment (Figure 3.5), as expected; CpM deformations eventually gain

importance when the strain contributions of the [2(C_2H_2)] fragment are similar (Rh and Ir cases).

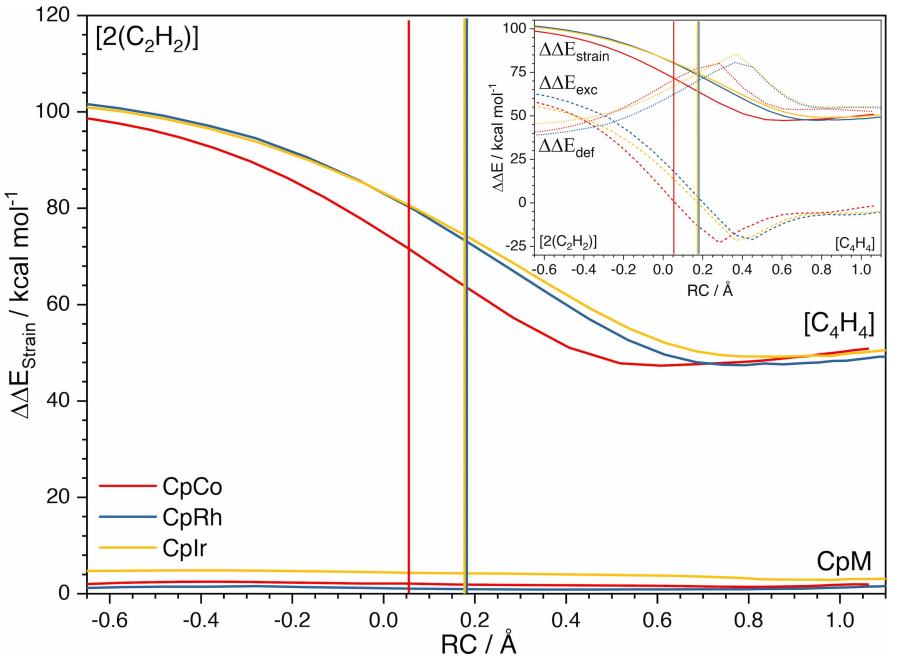

Figure 3.5. Contributions from each fragment to $\Delta\Delta E_{strain}$; $\Delta\Delta E_{strain}$ of the bis-acetylene fragment is further decomposed in a pure deformation contribution $\Delta\Delta E_{def}$ and in the electronic valence excitation contribution $\Delta\Delta E_{exc}$ of the deformed reactants (upper right corner inlay).

The structure of the CpIr fragment is slightly more distorted with respect to its relaxed geometry than the structure of the CpRh and CpCo. Overall, very similar total strain values have been found for Rh and Ir catalysts. The curve of the strain of the [2(C_2H_2)] fragment of the cobalt complex is much lower than those of the other metal catalysts along almost the whole path: this contributes importantly to lower the barrier in the presence of cobalt. The strain of the [2(C_2H_2)] fragment comprises a pure deformation contribution and the electronic excitation contribution of the deformed reactants at each point along the reaction coordinate. The interplay between these contributions explains why it is much lower in the case of cobalt (Figure 3.5). In fact, the two acetylenes come closer with respect to each other when they have to

coordinate to the smallest metal. As a consequence, they have more mutual repulsion and this causes the initially bigger value of $\Delta\Delta E_{def}$ of the $^3[(2C_2H_2)]$ fragment (see small inlay in Figure 2). But of course, this also makes the gap between π–π and π^*+π^* smaller and therefore the $\Delta\Delta E_{exc}$ term becomes relatively more favorable, an effect that apparently dominates the overall $\Delta\Delta E_{strain}$.

Summarizing, the trend for the overall strain contribution is CpCo < CpRh < CpIr, that is the strain contribution becomes less stabilizing when going from Co to Rh and Ir. An inverse trend is found for interaction (at least in the left part of the curve, i.e. from the bis-acetylene precursor to the transition state): CpCo < CpRh < CpIr (in absolute value). This means that the interaction contribution becomes less stabilizing when going from Ir to Rh and Co. Thus, the energy profile depends on the balance between strain and interaction. Notably, both strain and interaction decrease when going from CpM1 to TS(CpM1,CpM2). In fact, the reference relaxed fragment for the $[2(C_2H_2)]$ moiety is formed by two acetylene molecules in singlet state. When imposing to this last fragment the suitable electron configuration to form CpM1 (Figure 3.4 B), the electronic contribution to the strain dominates the pure deformation one, which progressively increases with the reaction progress (Figure 3.5).

In Figure 3.6, the results of EDA are shown, i.e. the interaction computed along the reaction coordinate is decomposed into the Pauli repulsion (ΔE_{Pauli}) orbital interaction (ΔE_{oi}), and electrostatic (ΔV_{elstat}) contributions.

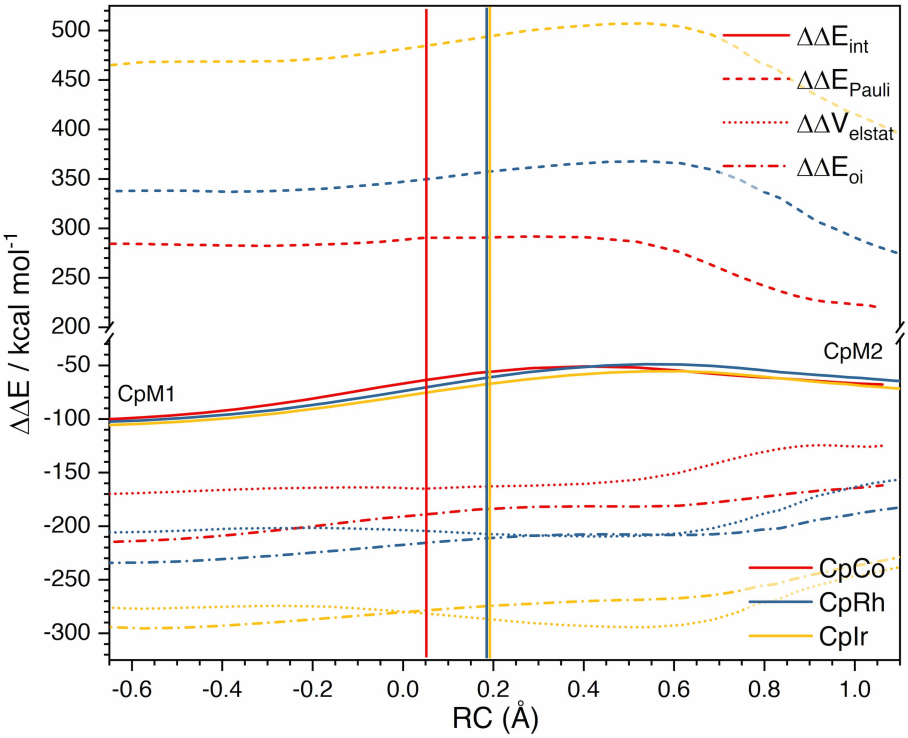

Figure 3.6. EDA along the reaction coordinate for the three studied reactions.

ΔE_{Pauli} remains almost constant along the reaction and the largest difference among the metals is observed in this contribution. In fact, it increases along the group, from Co to Rh and Ir, due to the d and s completely filled orbitals (from Co to Rh) and to additional fully populated 4f orbitals (from Rh to Ir). Being this contribution positive, it means that the heaviest metals are disfavored by high Pauli repulsion. The stabilizing electrostatic and orbital interaction terms increase in absolute value from Co to Rh and Ir. The importance of the former gains weight in this order because, to achieve large electrostatic interactions, an extended metal center with a high polarizability is required. In the case of cobalt, it remains significantly smaller (in absolute value) than the orbital interaction term during the whole reaction. In the case of rhodium, the two curves cross after the transition state and overlap for a part, until they separate again, $\Delta\Delta V_{elstat}$ remaining always above $\Delta\Delta E_{oi}$. Finally, in the case of iridium, the two

curves cross before the transition state and the electrostatic interaction becomes more stabilizing than the orbital interaction contribution. Overlaps between partially filled orbitals influence the attractive interactions; less extended systems, such as CpCo, have smaller overlap between fragments' orbitals. Conversely, in very expanded systems, like CpIr, stabilizing effects arise due to larger overlap.

We have analyzed and compared the three correlation diagrams of CpM1 formed by the fragments $^3[C_4H_4]$ and ^{3}CpM to gain insight into the difference among the metals. The focus of our attention is on the frontier region for clarity. The singly occupied frontier molecular orbital (MOs) of the ^{3}CpM and $^3[2(C_2H_2)]$ fragments are strongly metal d based, while those on the $^3[2(C_2H_2)]$ fragment are combinations of bonding and anti-bonding π MOs of acetylene. Those spanning A' symmetry combine into HOMO-2 (Co) and HOMO-1 (Rh and Ir). Those spanning A'' symmetry combine into HOMO-7 (Co) and HOMO-8 (Rh and Ir).

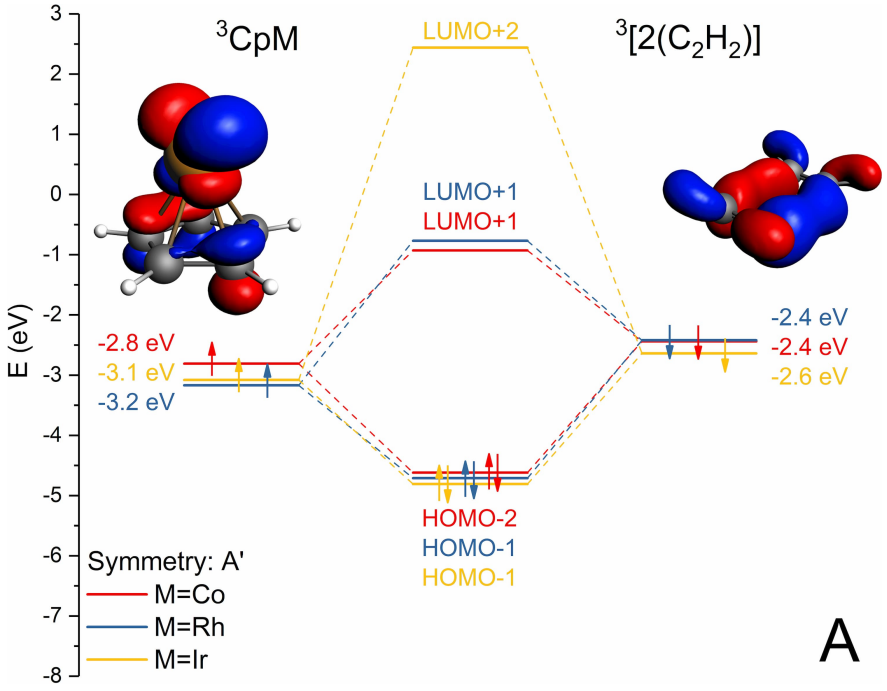

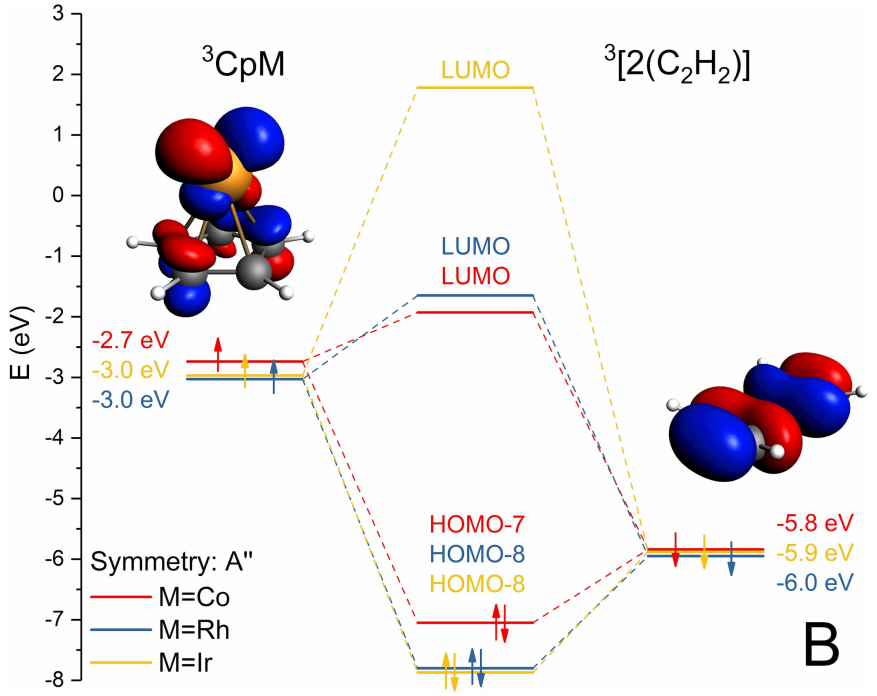

Figure 3.7. Simplified ^{3}CpM-^{3}[2(C$_2$H$_2$)] frontier orbital interaction diagram for M = Co(red), Rh(blue), and Ir(yellow).

These MOs are fundamental for the bonding between the two fragments. The associated orbital interaction gains strength when going from Co to Rh and Ir, since the singly occupied metal d-based orbitals go down in energy along that series which causes the electrons from the destabilized ^{3}[2(C$_2$H$_2$)] fragment to drop deeper in energy when they go into the bonding overall MO (Figure 3.7). Summarizing, the stabilization of the SOMOs (and therefore of the CpM1 MOs) along group 9 clarifies the increasing bond strength between the ^{3}[2(C$_2$H$_2$)] fragment and the metal center. As a consequence, the bond strength between the metal and the aromatic Cp ring decreases when going from Co to Rh and Ir, or, alternatively, the strengthening of the ^{3}CpM-^{3}[2(C$_2$H$_2$)] bond when going from Co to Rh and Ir explains the higher strain in Rh and Ir systems and indirectly the increase of the slippage with increasing metal size.

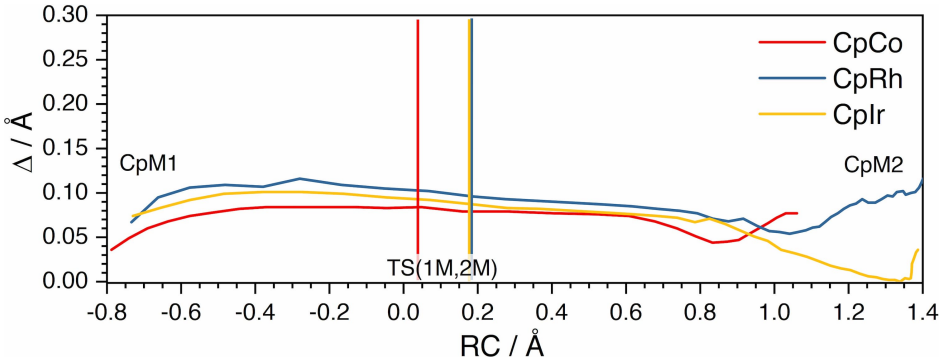

Figure 3.8. Variation of Basolo's slippage parameter along the reaction coordinate.

Aiming at relating the metal slippage, which is a structural parameter, as discussed in the Introduction, to the catalyst reactivity, we have plotted the metal slippage value along the reaction coordinate (Figure 3.8). The starting point on the left, i.e. the CpM1 structures, have Δ values in the expected order (CpCo1 < CpRh1 < CpIr1). Nevertheless, very early, the curve of Ir takes position below the curve of Rh, indicating that during the oxidative coupling, the slippage of the former metal is less pronounced than that of the latter one. This trend (Co < Ir < Rh) reflects the order of the position and of the height of the reaction barriers, suggesting a relation between the structure (slippage parameter) and the reactivity.

3.4 Conclusions

The oxidative coupling leading from a bis-acetylene CpM compound to a metallacyclopentadiene complex for group-9 metal half-sandwich catalysts goes with a barrier that increases along CpCo ≤ CpIr < CpRh. Gratifyingly, the previously presented QM simulations are in excellent agreement with the well-known experimental observation that Co catalysts perform better for this class of reactions.

The activation strain analyses along the reaction coordinate give insight into the physical factors behind this trend: the better

performance of Co-based catalysts is due to the 'rigidity' of the CpCo fragment. This finding might seem counterintuitive since, typically, hapticity variations suggest higher reactivity. Conversely, in this specific case, the smallest metal of the group hardly slips and conserves its high hapticity during the whole reaction. We have explained this phenomenon by quantifying the strength of the electron-pair bonding between the set of SOMOs on the $^3[2(C_2H_2)]$ fragment and those on the the metal center of the CpM fragment: this bond becomes stronger as the polarity in the electron-pair bonds increases when going from CpCo to CpRh and CpIr. Thus, along this series, the electrons stemming from the $[2(C_2H_2)]$ fragment experience more stabilization when entering into the SOMO + SOMO bond orbitals due to the lowering in energy of the metal d-derived CpM SOMOs. The more loosely metal-bonded $[2(C_2H_2)]$ fragment, which evolves to $[C_4H_4]$ in the cobaltacyclopentadiene, shows a fast decrease of the strain contribution which results in a lower barrier for CpCo than for CpRh and CpIr catalysts. In addition, this remarkable decrease in strain in the case of cobalt has been traced to the small size of this metal as compared to rhodium and iridium. No significant difference between CpRh and CpIr is found and, as far as this specific mechanistic step is concerned, no clear preference emerges.

Another important conclusion can be drawn regarding the metal slippage reflecting the metal-Cp bonding strength, which contrary to the bond strength between the $^3[2(C_2H_2)]$ and the ^{3}CpM fragments, is expected to decrease when going from Co to Rh and Ir. The stronger the metal-Cp bond is, the smaller the slippage parameter value. This holds true along the reaction path for cobalt, which remains less slipped than rhodium and iridium; the difference between these last metals is less significant. This qualitatively represents the 'rigidity' of the cobalt system, identified as an important structural element for its catalytic performance.

3.5 Addendum

Table S 3.1. Relevant interatomic distances (Å), Basolo slippage parameter Δ (Å) and angles (°) of selected crystallographic structures and computed geometries of CpM1 (1M), TS(CpM1,CpM2) (TS(1M,2M)), CpM2 (2M) (M= Co, Rh, Ir).

	CSD ID	Δ (Å)	M-C (Å)	**α** (°)	**γ** (°)	M-C_α (Å)	M-C_β (Å)	C_β-$C_{\beta'}$ (Å)
Co	BODJUZ	0.02	1.708	56.5	0.5	2.026	2.869	1.520
	CPBYCO	0.01	1.734	49.1	1.0	2.024	2.881	1.443
	1Co	0.03	1.771	-	0.6	2.013	2.019	2.812
	TS(1Co,2Co)	0.08	1.796	-	0.0	1.938	2.032	1.961
	2Co	0.11	1.759	5.8	0.9	1.890	2.520	1.487
	^{3}2Co	0.04	1.857	16.0	0.3	1.907	2.762	1.448
Rh	GOKGIW	0.03	1.940	49.8	0.5	2.099	3.000	1.513
	PBUDRI10	0.02	1.940	49.7	0.9	2.102	2.951	1.445
	1Rh	0.06	1.984	-	1.4	2.140	2.146	2.903
	TS(1Rh,2Rh)	0.10	2.006	-	0.4	2.055	2.175	1.989
	2Rh	0.13	1.956	30.8	2.2	2.059	2.907	1.480
	^{3}2Rh	0.05	2.051	22.3	0.2	1.989	2.893	1.423
Ir	GOKGOC	0.03	1.922	49.6	0.8	2.130	3.026	1.344
	GOKGUI	0.05	1.928	49.9	0.9	2.120	3.037	1.521
	MPBYIR10	0.06	1.924	49.2	2.4	2.118	2.986	1.318
	1Ir	0.08	1.963	-	1.0	2.135	2.149	2.850
	TS(1Ir,2Ir)	0.09	1.991	-	0.1	2.048	2.182	1.994
	2Ir	0.06	1.905	16.5	3.1	2.075	2.911	1.496
	^{3}2Ir	0.07	2.028	14.9	1.0	1.986	2.897	1.423

4 The Slippage Span Model

Adapted from

M. Dalla Tiezza, F. M. Bickelhaupt, L. Orian

ChemistryOpen 2019, 8, 143–154.

4.1 Introduction

As we have seen in the previous chapter, metal-catalyzed [2+2+2] cycloadditions are important reactions for the synthesis of cyclic and polycyclic compounds such as benzene, pyridine and their derivatives, starting from unsaturated molecules like alkynes, alkenes and nitriles [48]. Half-metallocene fragments, in which the metal is coordinated to an aromatic moiety and the electronic saturation is ensured by ancillary ligands (CO, phosphines, etc…), are largely employed. An important advantage of these catalysts is the facility of displacement of the metal from the centroid of the coordinated aromatic ring, called slippage, which can change along the catalytic cycle in some cases also dramatically. Slippage has important effects on the structure and energy

of the intermediates and transition states, thus affecting the reactivity. The most studied organometallic half-sandwich compounds for the alkynes [2+2+2] cycloadditions are those containing the ubiquitous cyclopentadienyl anion (Cp, Figure 4.1 A) and the indenyl anion (Ind, Figure 4.1 B). Recently, the diheteroaromatic rings 1,2-azaborolyl (Ab, Figure 4.1 C) and 3a,7a-azaborindenyl (Abi, Figure 4.1 D) have also been tested *in silico* in Rh(I) half-sandwich catalysts [95–106]. The idea was to design catalysts for alkynes [2+2+2] cycloadditions with an enhanced metal slippage, promoted by the low symmetry of these anions, which are isoelectronic to the parent hydrocarbon Cp and Ind, respectively.

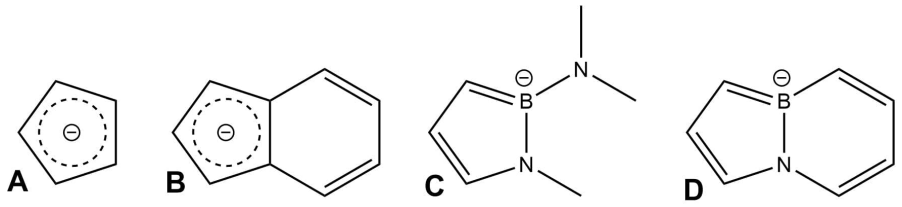

Figure 4.1. Aromatic ligands of the half-sandwich catalysts: A: cyclopentadienyl anion (Cp, $C_5H_5^-$); B: indenyl anion (Ind, $C_9H_7^-$); C: 1,2-azaborolyl anion (Ab, $C_6H_{12}BN^-$); D: 3a,7a-azaborindenyl anion (Abi, $C_7H_7BN^-$).

Cyclotrimerizations are strongly exergonic processes highly disfavored by entropic factors and so their activation energy is typically quite high (60-80 kcal/mol) [54]. The first evidence about a Ni(II)-catalyzed cyclotrimerization, based on the 1,3,5,7-cyclooctatetraene (COT) ligand, was reported by Reppe et al. [2]. Pyridine synthesis from alkynes and nitriles, driven by CpCo as catalyst, was highlighted in the pioneering studies of Wakatsuki and Yamazaki in 1973 [3,63], followed by the work by Vollhardt et al. [66,67] and by Bönnemann et al. [64,65] in the 80s. For many years, cobalt-based catalysts stayed on the top, in terms of efficiency. The first Rh(I) catalyst ever reported and used in alkynes cycloadditions was the neutral rhodacyclopentadiene/arsine complex in 1968 [107]. Afterward, Booth et al. [68] and Ingrosso et al.

[69,108] described a variety of Rh(I) half-sandwich complexes, which have been synthesized and tested to understand how to trim and optimize the overall cyclotrimerization yield. In agreement with Wakatsuki's and Yamazaki's observations for Co catalysts, [Rh(η^5-C_5H_5)L_n] (L=C_2H_4, CO, PR_3; L_2=1,5-cyclooctadiene (COD)) figured out to be very promising; L_n refers to a bunch of common ligands used in inorganic catalysis, such as C_2H_4, carbonyl (CO), tertiary phosphines (PR_3) or a bulky group like 1,5-cyclooctadiene (COD). These [2+2+2] cycloadditions take place at the temperature of reflux of toluene, but further efforts were made to test different environmental conditions with the aim of tuning the overall rate. Importantly, recent studies also report analogous reactions in aqueous solution [109,110]. Unfortunately, in all these experimental studies, a rigorous mechanistic investigation was never performed, and only few hypotheses were proposed. For example, Ingrosso and co-workers discussed the coordination of a nitrile to the metallacycle intermediate in terms of two possibilities: either *end-on*, that is via formation of a σ bond, or *side-on*, that is via an interaction metal-CN π system. The lack of mechanistic details about [2+2+2] cycloadditions catalyzed by Rh(I) compounds is also emphasized in the rather recent book 'Transition-Metal-Mediated Aromatic Ring Construction' by Ken Tanaka [48] who writes:

> *"…Although mechanistic aspects of these reactions attract interest, only a few studies have been reported in specific catalysts and substrates…"*

The mechanistic investigation by Albright and co-workers [54] on CpCo catalyzed acetylene cyclotrimerization to benzene is undoubtedly pioneering. They analyzed the potential energy surface of the whole catalytic cycle mainly with Hartree-Fock (HF) method and thus missed some intermediates because of lack of electron correlation, although all

the relevant species were thoroughly discussed. A few years later, Calhorda and Kirchner and co-workers described CpRuCl acetylene [2+2+2] cycloaddition to benzene using DFT methods [55]. In 2007, the same reaction, catalyzed by CpRh as well as by IndRh fragments, was analyzed [56]. Orian and coworker discussed different paths for the synthesis of benzene and also tackled the CpRh catalyzed synthesis of 2-methylpyridine from acetylene and acetonitrile. In 2008, the same authors explained the *end-on/side-on* linkage isomerism of a generic nitrile coordinated to a rhodacycle, which is an elementary step first postulated by Ingrosso [69] in the CpRh catalyzed synthesis of 2-methylpyridine [73]. Another exciting investigation of reaction paths was performed by Koga et al. [71] on Co-based half-sandwich catalysts, taking into account the stability of the triplet electronic state of the cobaltacycle formed during the first step, i.e. the oxidative coupling.

The CpIr catalyst has also been studied *in silico*, although the interest in iridium has remained quite limited compared to other metals, such as Co, Rh [74,75] and Ru [55]. The advantage of CpCo, with respect to the heavier CpRh in the initial oxidative coupling to form the metallacyclopentadiene, has been rationalized in the previous chapter and ascribed to the smaller slippage variation of the lighter metal along the reaction path [111].

One puzzling aspect emerging in the above mentioned DFT mechanistic study of 2007 [56], in which CpRh and IndRh are compared, is the lack of indenyl effect, consisting in an *'enhanced kinetic performance'* of the latter fragment which, due to the presence of the benzene ring fused with the Cp moiety, allows easier metal slippage. This unexpected computational result, lead to the hypothesis of a different mechanism [33] inspired by the experimental work by Booth et al. [68], in which the real catalysts are L-CpRh and L-IndRh (L=CO).

In this chapter, the slippage span model will be presented in order to establish a relationship between the structure, the energetics and the activity of CpRh, IndRh, AbRh and AbiRh employed in

[2+2+2] acetylene cycloadditions to benzene and [2+2+2] acetylene/acetonitrile cocycloadditions to 2-methylpyridine, likely transferable to analogous catalytic fragments. The novelty is addressing the whole catalytic cycle rather than focusing on key elementary steps, such as the initial oxidative coupling. To this purpose, the energy profiles of few more catalytic cycles have been evaluated, while others were taken from literature. In addition, in selected cases, comparison with CpCo and CpIr catalysis is made to assess the role of the metal center.

4.2 Methods

All DFT calculations were performed with the Amsterdam Density Functional (ADF) program [77–79]. In order to keep consistency with the literature, no changes to the level of theory have been made. The details can be found in Section 3.2.

4.3 Results and discussion

The main target is to relate the chemical reactivity of the studied half-sandwich catalysts to their relevant changes in geometry during the cyclotrimerization process. First, we investigate *in silico* the PESs of acetylene [2+2+2] cycloadditions to benzene and acetylene/acetonitrile cocycloadditions to 2-methylpyridine catalyzed by half-sandwich group 9 metal (Co, Rh, Ir) fragments. Using the energy span model, TOF values of catalytic cycles are computed and trends are discussed in a later stage. In particular, observing that lower TOF values are associated to low-symmetry and/or more largely slipped catalysts, a novel slippage parameter, LISP, which accounts for non-symmetric metal displacements from the centroid of the coordinated aromatic ring has been defined. It emerges that the larger the slippage span, ΔLISP, defined as the difference between the maximum and minimum hapticity value measured in a cycle, the lower the TOF. This is the essence of the

slippage span model, intended as a tool for designing efficient metal half-sandwich catalysts for alkyne [2+2+2] cycloadditions.

4.3.1 Group 9 metal catalyzed acetylene [2+2+2] cycloaddition to benzene: reaction mechanism and PES

The simplest metal catalyzed [2+2+2] cycloaddition converts three molecules of acetylene into benzene. Over the years, several mechanisms have been proposed and analyzed (Figure 4.2). It is consolidated that the path starts from a catalyst precursor [ZML_n] (Z: Cp, Ind, Ab, Abi; M: Co, Rh, Ir; L: C_2H_4, CO, PR_3; L_2: COD) in which the ancillary ligands L are replaced by two acetylene molecules in a photo or thermochemical process [56]. By oxidative coupling of the two acetylenes, the very stable 16-electron ZM2 intermediate forms. From the reaction environment, an acetylene easily coordinates the metal center in η^2 fashion in order to restore a stable 18 electron configuration (ZM3). The synchronous formation of two CC bonds leads to the formation of an unusual bent six membered ring in ZM4 (Figure 4.2 I): this arrangement allows benzene to remain coordinated to the metal satisfying the 18 electron rule. Then, cleavage occurs by stepwise addition of two acetylene molecules to regenerate ZM1. An interesting variation proposed by Schore [112] predicts the formation of a metallacycloheptatriene (ZMh) upon insertion of the third acetylene in one of the two metal carbon bond of the five membered ring of ZM2; then, benzene formation occurs by reductive elimination (Figure 4.2 II). This last step requires a high activation energy and thus this path is ruled out from the mechanism, as explained in detail in Ref [56].

An alternative path was proposed by Booth and co-workers [68], which relies on the hypothesis that, at the beginning, acetylene replaces only one of the two ligands L of the catalyst precursor. This leads to a significantly different mechanism [33], characterized by peculiar intermediates (Figure 4.3) like the rhodabicyclo[3.2.0]heptatriene and the rhodaheptatetraene, which are structurally similar to intermediates

found in the catalytic mechanism of CpRuCl [55]. Starting from ZM2, an alternative mechanism in triplet state might take place: in fact, Dahy et al. showed the larger stability of the triplet state cobaltacycle compared to the singlet one, i.e. 16.6 kcal mol^{-1} [88]. Then, the catalytic cycle continues on the triplet surface till the second crossing point, which corresponds to the intermediate ZM4, although on Dahy's mechanism the preceding coordination of acetylene implies two different intermediates.

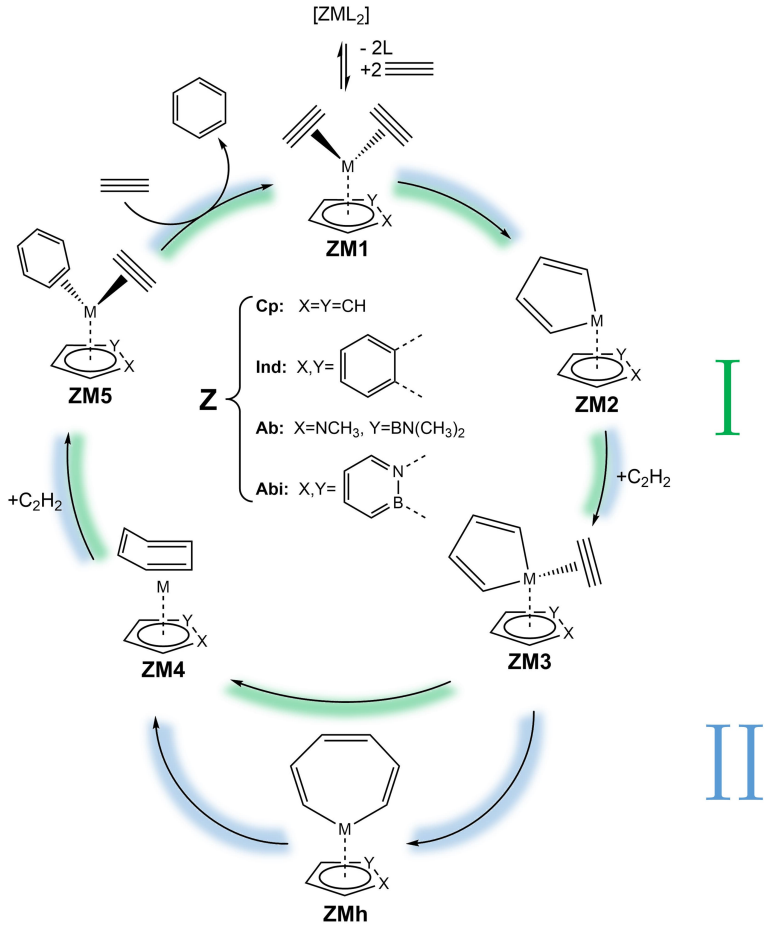

Figure 4.2. Mechanism of acetylene [2+2+2] cycloaddition to benzene catalyzed by a half-sandwich metal fragment CpM (M=Co, Rh, Ir) and ZRh; (L= C_2H_4, CO, PH_3).

ZM4 is more stable in triplet state, but this electronic change implies also a variation of the benzene coordination from eta4 to eta6. The last corssing point leading again to the singlet surface is not reported in [48], but should correspond to the coordination of the two acetylene molecules to displace benzene.

The potential energy surfaces (PESs) for benzene synthesis (Figure 4.2 I) catalyzed by CpCo and CpIr were calculated at ZORA-BLYP/TZ2P, i.e. the same level of theory of the previous chapter and of those taken from literature, as in the case of CpRh, IndRh [33], AbRh and AbiRh [70]. Only singlet states were considered. However, some authors [71] report a possible alternative mixed multiplicity reaction path for CpCo catalysis where the initial singlet state bis-acetylene complex gives rise to a triplet cobaltacycle and only at a later stage, the process moves back again to the singlet PES.

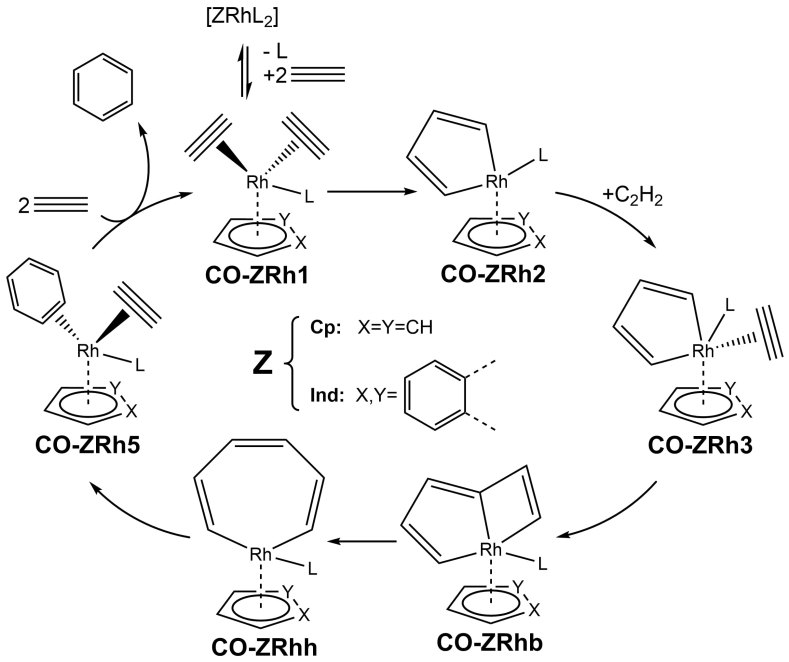

Figure 4.3. Mechanism of acetylene [2+2+2] cycloaddition to benzene catalyzed by a half-sandwich Rh(I) fragment in the hypothesis that an ancillary ligand

(L=CO) remains bonded to the metal throughout the whole catalytic cycle [33].

At a glance, the CpCo catalyzed cycle shows the flattest PES, while the AbRh and AbiRh catalyzed ones show the largest energy span (Figure 4.4). This already gives a qualitative idea of the catalysts' performance: Co-based catalysts (in this case CpCo) are better suited for cyclotrimerizations than analogous Rh or Ir-based complexes, in agreement with experimental findings. The loss of performance in presence of more asymmetric aromatic ligands like Ab and Abi, as reported in 2013 [70], is also evident.

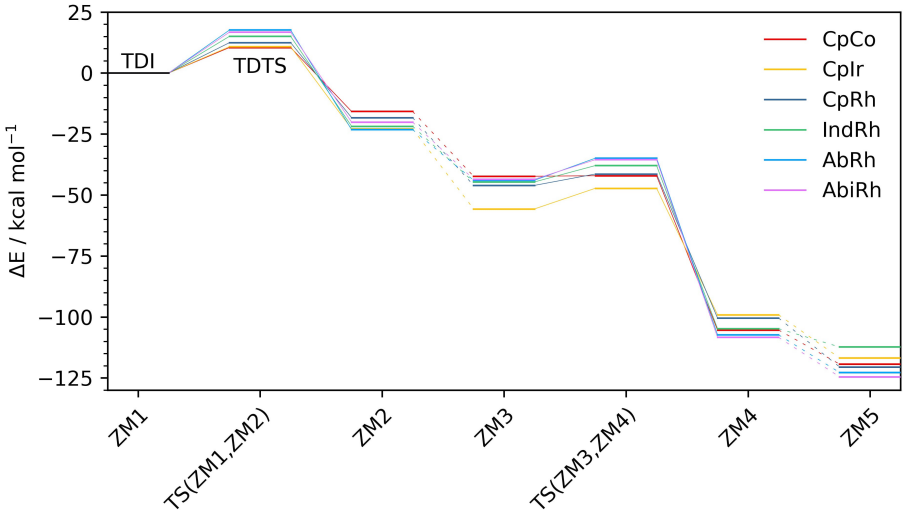

Figure 4.4. Energy profile of acetylene [2+2+2] cycloaddition to benzene (level of theory: ZORA-BLYP/TZ2P). The mechanism is shown in Figure 4.2 I.

4.3.2 Group 9 metal catalyzed acetylene/acetonitrile [2+2+2] cycloaddition to 2-methyl pyridine: reaction mechanism and PES

The mechanism leading to 2-methylpyridine was studied as well. Early experimental studies [64,69] report catalyzed cyclotrimerizations with pyridine or pyridine derivatives as products when acetylene pressure is partially replaced by acetonitrile or molecules with a CN functional

group. The mechanistic details differ from those of benzene synthesis because the forming π-system is not symmetric (due to the presence of N) and thus more intermediates are found. The reaction path of CpRh catalyzed [2+2+2] cocycloaddition to 2-methylpyridine [56], used afterwards as model mechanism, is characterized by 9 intermediates and 6 transition states (Figure 4.5).

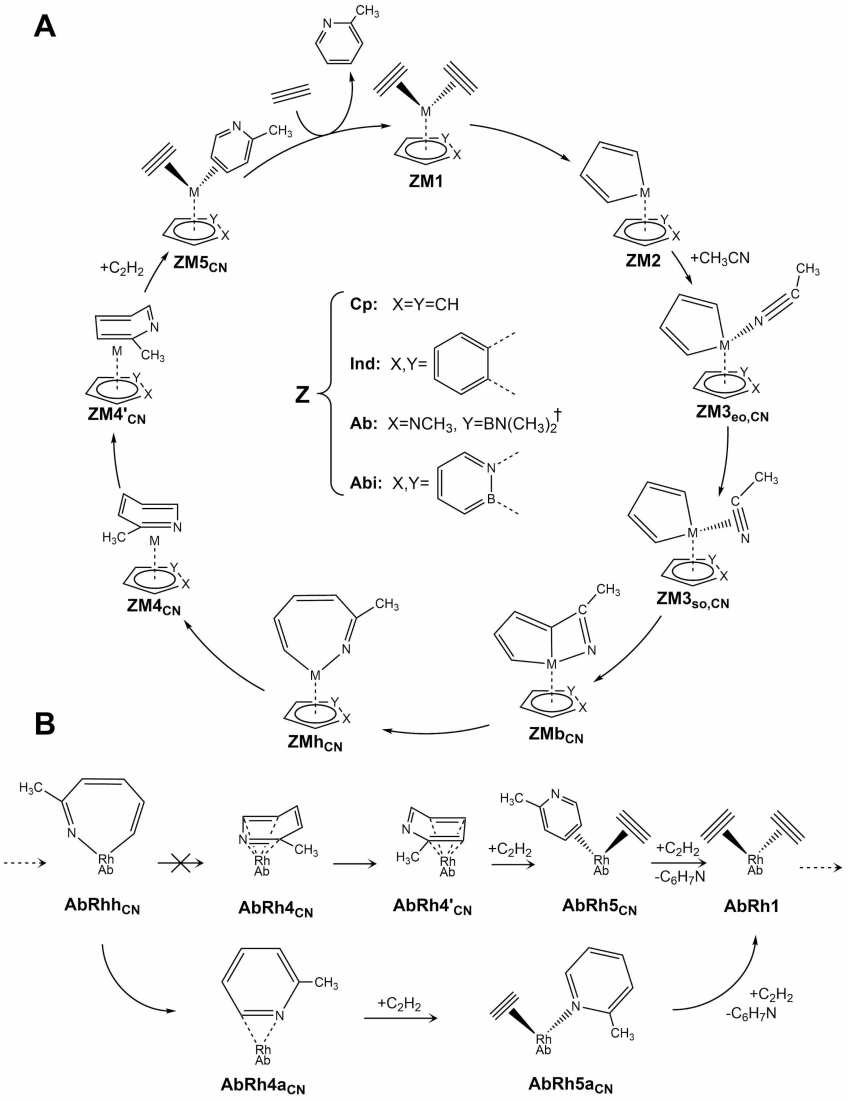

Figure 4.5. A) Mechanism of acetylene/acetonitrile [2+2+2] cycloaddition to 2-methylpyridine catalyzed by a half-sandwich metal fragment CpM (M=Co,

Rh) and ZRh. † Only up to ZMhCN, then the cycle proceeds as shown in Figure 4.5 B. B) Final part of the mechanism of acetylene/acetonitrile [2+2+2] cycloaddition to 2-methylpyridine catalyzed by AbRh fragment starting from the heptacyclic intermediate AbRhhCN.

The initial part of the cycle is identical to that of acetylene [2+2+2] cycloaddition to benzene, since the initial coordination of two acetylenes is thermodynamically more favored than the coordination of an acetylene and a nitrile [93]. The highest energy point of the whole cycle, TS(ZM1,ZM2), is reached when the five-membered metallacycle ZM2 forms. The nitrile coordination takes place in two steps: initially, the terminal nitrogen bonds to the metal center in σ fashion and without any appreciable energy barrier, forming an end-on complex ($ZM3_{eo,CN}$); then, upon rotation of the nitrile fragment, the overlap between the metal d orbitals and the CN π system increases and $ZM3_{so,CN}$ forms. This linkage isomerism leading to a side-on coordination of CH_3CN requires activation energy and was systematically studied *in silico* in 2008 [73]. Starting from the activated side-on structure and passing through TS($ZM3_{so,CN}$,ZMb_{CN}), the bicyclic complex ZMb_{CN} forms. Then, the hinge metal-carbon bond is weakened along the reaction coordinate and the heptacyclic structure ZMh_{CN} forms; despite coordinatively unsaturated, this is a very stable intermediate due to the high exothermic step. Then, a reductive elimination leads to the formation of $ZM4_{CN}$ in which the new born 2-methylpyridine is coordinated to the metal in η^4 fashion using four carbon atoms. A fast isomerization to a new η^4 structure $ZM4'_{CN}$ occurs. The new CCNC-bonded structure, located after the transition state TS($ZM4_{CN}$,$ZM4'_{CN}$), is more stable compared to the initial CCCC-bonded one. The addition of an acetylene molecule helps to lower the planar pyridine derivative hapticity from η^4 to η^2 in the last structure $ZM5_{CN}$. The complete removal of the product to the reaction environment is promoted by the addition of second acetylene and the initial catalyst is regenerated.

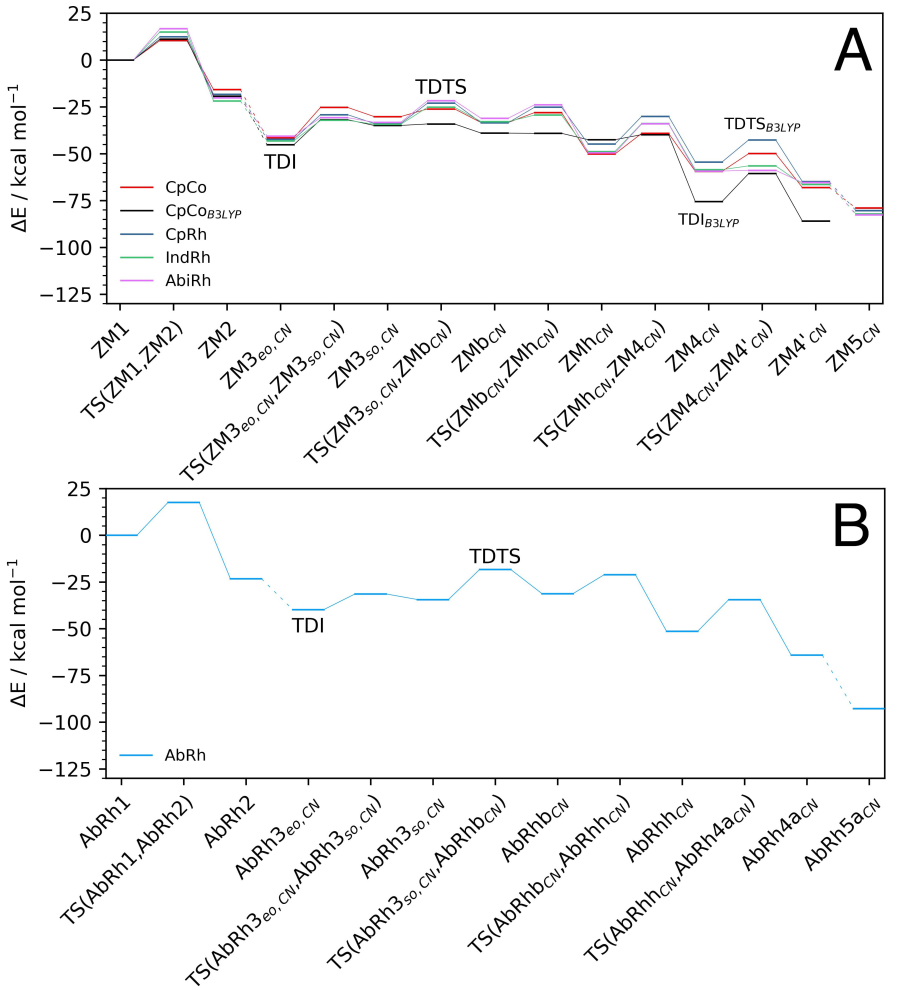

Figure 4.6. A) Energy profile of metal catalyzed acetylene/acetonitrile [2+2+2] cycloaddition to 2-methylpyridine (level of theory: ZORA-BLYP/TZ2P). The dashed black line was drawn using data taken from ref. [71] computed at a different level of theory, i.e. B3LYP/6-31G(d,p). The mechanism is shown in Figure 4.5 A. B) Energy profile of the AbRh catalyzed acetylene/acetonitrile [2+2+2] cocycloaddition to 2-methylpyridine. The alternative reaction path begins from AbRhh$_{CN}$ and is shown in Figure 4.5 B.

For comparison, we have included in Figure 4.5 A the CpCo catalyzed cycle computed at a different level of theory (black dashed line), that is B3LYP combined with 6-31G(d,p) basis set for all elements [71].

All intermediates and transition states sketched in Figure 4.5 have been successfully located on the PES with one exception in AbRh catalysis. In fact, for AbRh catalyst, the same mechanistic path of Figure 4.5 is followed, but only till the formation of the heptacyclic intermediate $AbRhh_{CN}$. The subsequent transition state does not lead to the formation of a complex with an η^4 coordinated 2-methylpyridine, but directly to the formation of a product with an η^2 coordinated 2-methylpyridine ($AbRh4a_{CN}$), bonded with a nitrogen and a carbon atom to the metal center (Figure 4.5 B). The last step is barrierless and ends with the formation of a σ bond between the metal and the N atom of 2-methylpyridine upon coordination of an acetylene ($AbRh5a_{CN}$). From this intermediate, the cycle switches back again to AbRh1, after 2-methylpyridine cleavage is promoted by the addition of a second acetylene molecule. For this reason, the PES of the AbRh cycle is not included in Figure 4.6 A, but is shown separately in Figure 4.6 B[d].

[d] All the calculations were carried out in the gas phase. To take into account solvation, we used the COnductor-like Screening MOdel (COSMO) [113]. The chosen solvents are toluene, a very common aprotic medium, and acetonitrile that is one of the reactants for the synthesis of 2-methylpyridine. Single-point energy correction with COSMO have been computed using the geometries optimized in the gas phase. This was possible after checking that our molecular structures are almost unaffected when embedded in solvent [61]. In both solvents, the result is an overall stabilization of the entire PES, as can be seen in Figure S 4.1, Figure S 4.2 and Figure S 4.3. Acetonitrile leads to the largest change in energies (a larger stabilization) whereas toluene shows a milder stabilization of stationary points, in line with the dielectric constants of the two solvents. The energy shift is almost constant for every intermediate and transition state. Thus, we can conclude that the solvent effects on the energy profiles may be disregarded for the analyzed processes. The main reason for this is the absence of strongly polarized and charged species.

4.3.3 TOF calculations

Generally, in organometallic catalysis, the most used parameter to measure how many moles of substrate are required to reach catalyst's saturation is the turnover number (TON). However, it is usually convenient to turn this value into a time dependent parameter, i.e. the turnover frequency, which is the turnover number per unit of time. After generating the PESes, the TOF of the catalytic cycles has been calucated as explained in the section 2.4.

To approach the experimental conditions in the TOF calculations, we chose two reference temperatures: the first one is the IUPAC standard room temperature (25° C) and the second one is the reflux temperature of toluene: 110.6° C, sometimes used as solvent in cyclotrimerization reactions [69].

Firstly, the acetylene [2+2+2] cycloaddition to benzene mediated by different catalysts will be discussed. In all cases, the TDI is the bis-acetylene intermediate, and the TDTS is the subsequent transition state leading to the five-membered ring metallacycle. The crucial step of the whole cycle is indeed the oxidative coupling since the degree of TOF control is almost one for all the analyzed catalysts. For this reason, a dedicated analysis of these species was recently performed [111]. CpCo has the highest efficiency (Table 4.1), in agreement with the experimental findings. CpIr is somewhat less performant, followed by CpRh. The less extended aromatic ligand (Cp anion) seems to be a better choice compared to polycyclic moieties, like Ind anion. The asymmetric diheteroaromatic fragments (AbRh and AbiRh) are in general the worst catalysts, and their chemical activities are more or less comparable.

Table 4.1. Calculated TOF values and TOF ratios[e] for the catalytic cycle of Figure 4.2 (acetylene [2+2+2] cycloaddition to benzene).

Catalyst	$TOF_{298.15K}$ (s^{-1})	$Ratio_{298.15K}$	$TOF_{383.65K}$ (s^{-1})	$Ratio_{383.65K}$
CpCo	$1.3 \cdot 10^{5}$	144928	$8.6 \cdot 10^{6}$	12464
CpIr	$6.9 \cdot 10^{4}$	100000	$5.1 \cdot 10^{6}$	7391
CpRh	$4.4 \cdot 10^{3}$	6377	$6.2 \cdot 10^{5}$	899
IndRh	$5.4 \cdot 10^{1}$	78	$2.0 \cdot 10^{4}$	29
AbiRh	$3.1 \cdot 10^{0}$	4	$2.2 \cdot 10^{3}$	3
AbRh	$6.9 \cdot 10^{-1}$	1	$6.9 \cdot 10^{2}$	1

Notably, no indenyl effect [114] is found, that is, no enhancement of reactivity is achieved using IndRh rather than CpRh, as predicted in 2007 [56]. In contrast, a mild indenyl effect is present with the diheteroaromatic catalysts considering AbRh and AbiRh, structurally analogous to CpRh and IndRh, respectively. The lack of indenyl effect was recently explained in the hypothesis that an ancillary CO ligand remains bonded to Rh throughout the whole catalytic cycle [33]. The TOF values were calculated for these cycles too (Table 4.2) and the Ind-based catalysts results ten order of magnitude more efficient than the Cp-based one.

Table 4.2. Calculated TOF values and TOF ratios for the catalytic cycle of Figure 4.3 (acetylene [2+2+2] cycloaddition to benzene).

Catalyst	$TOF_{298.15K}$ (s^{-1})	$Ratio_{298.15K}$	$TOF_{383.65K}$ (s^{-1})	$Ratio_{383.65K}$
CO-IndRh	$7.1 \cdot 10^{-9}$	$5.5 \cdot 10^{10}$	$4.3 \cdot 10^{-4}$	$2.3 \cdot 10^{8}$
CO-CpRh	$1.3 \cdot 10^{-19}$	1	$1.9 \cdot 10^{-12}$	1

[e] The TOF ratio is computed taking, as reference, the TOF of the worst catalyst.

The TOFs of acetylene/acetonitrile [2+2+2] cocyclotrimerizations to 2-methylpyridine were computed as well (Table 4.3). A change of the metal implies a significant variation in efficiency, as previously shown in Table 4.1 for acetylene cyclotrimerizations. Also, the trend is retained: CpCo works better than Rh-based catalysts. In this case, on the basis of the degree of TOF control, the TDI is the end-on adduct ($ZM3_{eo,CN}$), and the TDTS is the transition state between the species with side-on coordination of the acetonitrile and the bicyclic intermediate, TS($ZM3_{so,CN}$, ZMb_{CN}). This applies to all tested catalysts except CpCo. The energetics of the first CpCo catalyzed cycle was computed by Dahy et al. [71] with the B3LYP hybrid functional. They found that the TDI is the product of the reductive elimination of the heptacycle, when the first tetrahapto-bonded pyridine molecule is formed ($CpCo4_{CN}$). The TDTS lies between the two intermediatesvcharacterized by η^4 coordinated 2-methylpyridines, i.e., TS($CpCo4_{CN}$, $CpCo4'_{CN}$). The CpCo catalyzed cycle computed in the present work using ZORA-BLYP/TZ2P, identifies the TDTS mainly in correspondence of the end-on/side-on interconversion (80%), and the remaining part on the previously reported TS($ZM3_{so,CN}$, ZMb_{CN}) (20%). The TDI corresponds to the intermediate with the end-on bonded acetonitrile ($ZM3_{eo,CN}$).

This latter case is an instructive example of a situation in which the results from the energy span approximation (Eq. 2.12) may be misinterpreted. Thus, here, it is not possible to univocally identify the TDTS and this prevents a straighforward definition of a correct energy span to be used in Eq. 2.12. To avoid errors in TOF calculations, we used in all cases the complete equation (Eq. 2.10) without any approximation. The perfomance improvement can be readily seen also from the energy profiles (Figure 4.6 A) where, compared to the other cycles, the CpCo one is much flatter. This follows a pretty common rule of thumb used in catalysis: if a reaction involves small energy variations, it usually means that the cycle is characterized by very high reaction rates.

In 2-methylpyridine formation, a slight indenyl effect is present: IndRh is ten times more efficient than the CpRh. The AbiRh performance is mostly comparable to CpRh one (at both temperatures). AbRh TOF values cannot be compared since the reaction mechanism shows some significant differences in the final stages.

Table 4.3. Calculated TOF values for acetylene/acetonitrile cocyclotrimerization to 2-methylpyridine.

Catalyst	$TOF_{298.15K}$ (s^{-1})	$Ratio_{298.15K}$	$TOF_{383.65K}$ (s^{-1})	$Ratio_{383.65K}$
$CpCo_{B3LYP}$	$5.8 \cdot 10^{1}$	1450	$2.0 \cdot 10^{4}$	282
CpCo	$6.4 \cdot 10^{0}$	160	$3.4 \cdot 10^{3}$	48
IndRh	$4.0 \cdot 10^{-1}$	10	$4.2 \cdot 10^{2}$	6
AbiRh	$8.2 \cdot 10^{-2}$	2	$1.2 \cdot 10^{2}$	2
CpRh	$4.0 \cdot 10^{-2}$	1	$7.1 \cdot 10^{1}$	1
AbRh	$1.2 \cdot 10^{-3}$	-	$4.7 \cdot 10^{0}$	-

4.3.4 Slippage: a novel metal decentralization marker

The studied catalysts, in which the aromatic hydrocarbon ligand is the six electrons Cp anion or the ten electrons Ind ligand, have intriguing electronic and structural properties. In fact, as we saw in the previous chapter, the coordination of the metal to the ring is not perfectly symmetric (η^5), but can be described as a distorted arrangement in which the five metal-carbon distances are not equal: two distances are shorter (M– C1 and M– C3) and two distances are longer (M– C1a and M– C3a), as shown in Figure 4.7. Typically, one carbon atom (C2) is found between those at a closer distance, which may be located below the ring plane, so that a folding angle can be observed. This tipped structure, described as $\eta^3 + \eta^2$, is related to the phenomenon known as metal slippage. Further distortion can lead to an allylic coordination (η^3) and, *in extremis*, to the formation of a σ bond between the metal and one C atom (η^1). To quantify the amount of slippage, a parameter

was introduced by Fred Basolo [58] and previously defined in the Eq. 3.1.

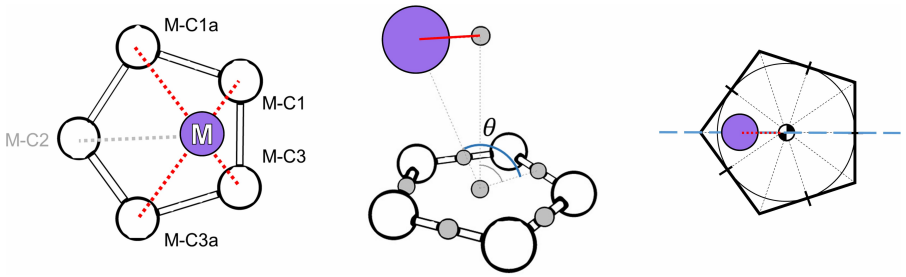

Figure 4.7. Novel definition of the metal slippage for a five-member ring.

Unfortunately, this slippage parameter is partially blind for "out-of-plane" metal displacements. The plane in question (Figure 4.7, blue dashed line) is orthogonal to the pseudo-plane containing the five memebered ring atoms. When a lateral movement of the metal center takes place, with a consequent irregular variation of the distance pairs M– C1a, M– C3a and M– C1, M– C3, the Δ parameter defined in Eq. 3.1 gives unreliable results.

A redefinition of slippage has been developed by us mainly for two reasons: light up every dark corner when we loose C_S symmetry and build a label independent parameter to monitor any metal displacement along the reaction coordinate. First, we have defined a ring centroid, equal to the center of mass when the five atoms are equal (Cp and Ind), and the middle points of all five bonds between adjacent ring atoms. These points are depicted in grey in Figure 4.7. The label independent slippage parameter (LISP) has been calculated as the sum of the five average minimum distances from a normal vector that passes through the centroid and the metal center (red line, Figure 4.7):

$$\text{LISP (Å)} = \frac{M}{N}\sum_{i=1}^{N}\left|\sin\left(\theta_i - \frac{\pi}{2}\right)\right| \qquad 4.1$$

where M is the distance between the metal atom and the ring centroid, θ_i is the angle between the middle point of two carbon atoms, the ring centroid and the metal and N is the number of atoms of the ring. This general definition can be extended in straightforward manner to five memebered rings containing heteroatoms. As expected, the trend is not too different from the Δ values (that preserves an optimal behavior in C_S symmetry for Cp and Ind anions) except when the metal atom drifts out of plane. The average distance has been chosen to take into account the distortion of the ring from a perfect polygon and to completely untie the label dependent formalism, intrinsic in the definition of Δ.

4.3.5 Slippage Span Model

The slippage parameter has been computed using the LISP definition for all the intermediates and transition states of the different catalytic cycles. For benzene formation (mechanism of Figure 4.2 I), the LISP values are shown in Figure 4.8.

CpM catalysts show a very small variation of LISP along the cycle, especially CpCo; conversely, in the presence of the Ind, Ab and Abi ligands higher hapticity variations are computed. To quantify this trend, we introduced a parameter called slippage span (ΔLISP), defined as the difference between the maximum and the minimum value of LISP of the whole cycle. ΔLISP values, for the cases shown in Figure 4.8, are listed in Table 4.4.

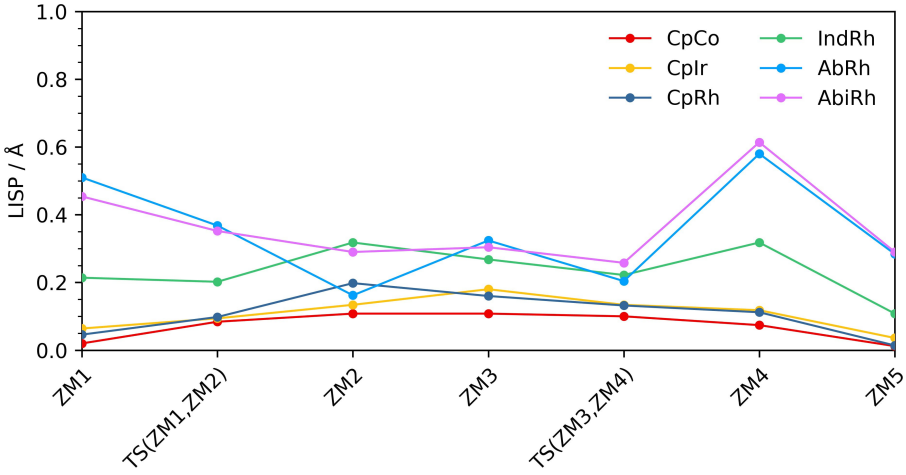

Figure 4.8. LISP values for acetylene [2+2+2] cyclotrimerization to benzene catalyzed by CpM (M=Co, Rh, Ir) and ZRh (Z=Ind, Ab, Abi). The mechanism is shown in Figure 4.2 I and the PESs are shown in Figure 4.4.

Table 4.4. Slippage span values (ΔLISP) and TOF ratios at ambient and toluene reflux temperature for metal-catalyzed acetylene [2+2+2] cycloaddition to benzene.

Catalyst	ΔLISP(Å)	TOF Ratio$_{298.15K}$	TOF Ratio$_{383.65K}$
CpCo	0.10	144928	12464
CpIr	0.14	100000	7391
CpRh	0.19	6377	899
IndRh	0.21	78	29
AbiRh	0.36	4	3
AbRh	0.42	1	1

In Table 4.4, the catalysts are ordered according to decreasing performance. A relationship between geometric and kinetic/energy parameters (TOF ratios) emerges: a lower slippage span corresponds to an increased catalytic activity for a given catalyst. A small slippage span is in general associated to low absolute LISP values, but the connection between these terms is not straightforward. CpCo is the most rigid fragment: the metal remains almost perfectly centered with respect to the Cp anion during the whole catalytic cycle and only weak

slippage occurs. The metal Cp bonding strength explains the trend of CpIr and CpRh [111]. As expected, IndRh, whose intermediates and transition states are more slipped and overall shows higher flexibility, is less performant than the other catalysts, that is no indenyl effect is found.

In contrast, a mild indenyl effect is found in presence of the two diheteroaromatic ligands: AbiRh works better than AbRh; also in these cases, the slippage span follows the trend above described.

The structural information gathered from the ZRh4 intermediate is interesting: in presence of bulky aromatic ligands, such as Ind^-, Ab^- or Abi^-, the slippage is very pronounced. The tetrahapto coordination of benzene is likely the cause. In fact, when the benzene molecule switches to an η^2 coordination in the ZRh5 intermediate, LISP values are dramatically lowered.

The important achievement is that a minimization of the slippage span leads to an increased catalytic efficiency in terms of TOF values. To confirm the validity of the slippage span model within different mechanisms, LISP values have also been calculated for acetylene [2+2+2] cycloaddition catalyzed by CO-CpRh and CO-IndRh, shown in Figure 4.3. Very high absolute LISP values were measured on the calculated structures since remarkable changes in hapticity take place due to the presence of the CO ligand (Figure 4.9). In fact, the metal center is always slipped far away from the ring centroid reaching in some cases also the η^1 coordination.

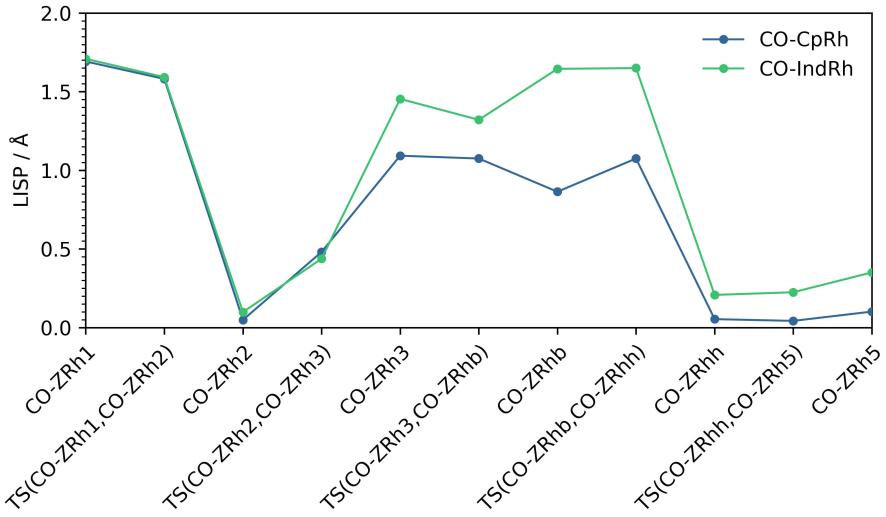

Figure 4.9. LISP values for acetylene [2+2+2] cycloaddition to benzene catalyzed by CO-CpRh and CO-IndRh. The mechanism is shown in Figure 4.3 and the PESs can be found in Ref [33].

In Table 4.5, ΔLISP values for these two cycles are listed with the corresponding TOF ratios. The difference between ΔLISP values is 0.04 Å for CO-CpRh and CO-IndRh and is comparable to the value obtained in Table 4.4 for CpRh and IndRh, i.e. 0.02 Å. Importantly, the trend is maintained: lower ΔLISP are found in correspondence of higher catalytic performance based on TOF values.

Table 4.5. Slippage span values (ΔLISP) and TOF ratios at ambient and toluene reflux temperature for CpRh and IndRh in the hypothesis that a CO ligand remains bonded throughout the whole catalytic cycle.

Catalyst	ΔLISP(Å)	TOF Ratio$_{298.15K}$	TOF Ratio$_{383.65K}$
CO-IndRh	1.61	$5.5 \cdot 10^{10}$	$2.3 \cdot 10^{8}$
CO-CpRh	1.65	1	1

The slippage span model was tested also for the acetylene/acetonitrile [2+2+2] cocycloaddition to 2-methylpyridine using CpM (M=Co, Rh, Ir) and ZRh (Z=Ind, Abi) catalysts. AbRh has been excluded because of mechanistic differences.

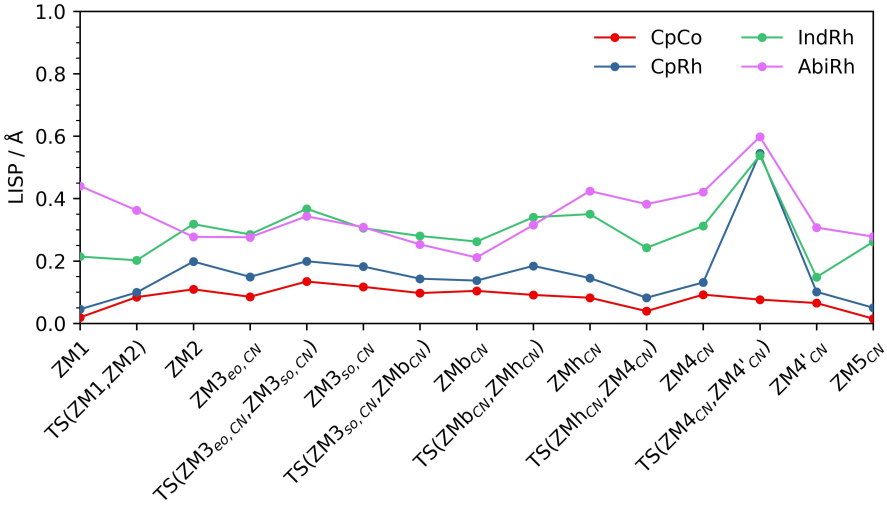

Figure 4.10. LISP values for [2+2+2] acetylene/acetonitrile cocycloaddition to 2-methylpyridine; the mechanism is shown in Figure 4.5 A and the PESs are shown in Figure 4.6 A.

In Figure 4.10, CpCo appears again as the most performant, in agreement with the experimental evidence and emerges also from the values reported in Table 4.6. Notably, a mild indenyl effect is found in this mechanism, while CpRh and AbiRh fragments are those with the lowest performance.

Table 4.6. Slippage span values (ΔLISP) and TOF ratios at ambient and toluene reflux temperature for metal-catalyzed acetylene/acetonitrile cocyclotrimerization to 2-methylpyridine.

Catalyst	ΔLISP(Å)	TOF Ratio$_{298.15K}$	TOF Ratio$_{383.65K}$
CpCo	0.12	160	48
IndRh	0.39	10	6
AbiRh	0.39	2	2
CpRh	0.50	1	1

4.3.6 Improvement of the Slippage Span Model

ΔLISP is a simple and efficient way to relate reactivity to a structural parameter, but it seems weak in some critical cases, i.e. small ΔLISP can correspond to large/small difference in TOF ratios and vice-versa. This could be probably overridden by redefining the slippage span with a more complete descriptor that takes into account all intermediates and transition states rather than considering only the extreme values. This pushed to work on an extension of the original descriptor (ΔLISP). After different trials, the improved slippage span parameter (ΔLISP*) was introduced (Eq. 4.2). It is the sum of three contributions:

$$\Delta\text{LISP}^{*}\ (\text{Å}) = \sum_{i=1}^{N-1} |\text{LISP}_1 - \text{LISP}_{i+1}| + \sum_{i=1}^{N-1} |\text{LISP}_i - \text{LISP}_{i+1}| + |\text{LISP}_N - \text{LISP}_1| \qquad 4.2$$

The first term takes into account how structurally far/close from the starting point every intermediate or transition state of the catalytic cycle is. The second term contains the slippage difference between an arbitrary state and the one immediately following. The last term (third block) is simply the slippage variation between the last intermediate located on the PES and the recovered catalyst. Every term must be as small as possible in order to have a more efficient catalytic system: in this way, ΔLISP* preserves the same meaning given for the original slippage parameter (ΔLISP). A summary of the results are reported in Table 4.7: at a glance, a great improvement can be noticed when considering the couple CO-CpRh and CO-IndRh for the benzene synthesis and in IndRh and AbiRh for the synthesis of 2-methylpyridine. In these two cases, the sensitivity issues founded with ΔLISP have been nicely solved with ΔLISP*.

Table 4.7. TOF ratios, slippage span values (ΔLISP) and improved slippage span values (ΔLISP*) for benzene and pyridine synthesis.

	Catalyst	TOF $Ratio_{298.15K}$	ΔLISP (Å)	$\Delta LISP^{*}$ (Å)
Benzene	CpCo	144928	0.10	0.58
	CpIr	100000	0.14	0.66
	CpRh	6377	0.19	0.88
	IndRh	78	0.21	1.02
	AbiRh	4	0.36	2.00
	AbRh	1	0.42	2.81
	CO-IndRh	$5.5 \cdot 10^{10}$	1.61	14.48
	CO-CpRh	1	1.65	16.31
Pyridine	CpCo	160	0.12	1.34
	IndRh	10	0.39	2.76
	AbiRh	2	0.39	3.04
	CpRh	1	0.50	3.14

4.4 Conclusions

Herein, the slippage span model has been developed and it's itended to establish a quantitative relationship between, on one hand, the extent of variation in the geometrical slippage along the reaction of the metal relative to its aromatic ligand in group-9 metal half-sandwich complexes and, on the other hand, their catalytic activity in [2+2+2] alkyne cycloadditions. Our computed turn over frequencies (TOF) of the catalytic cycles for acetylene cyclotrimerization to benzene show that Co catalysts perform better than Rh and Ir ones. This trend originates from the first reaction step, oxidative coupling, which involves both, the TOF-determining intermediate (TDI) and the TOF-determining transition state (TDTS). In this elementary step, the rigid, almost perfectly η^5 CpCo complex is more efficient than the more slipped η^3+η^2 CpRh and CpIr complexes [111].

On the other hand, an indenyl effect is found when comparing CpRh and IndRh catalysts in the cocyclotrimerization of

acetylene/acetontrile to 2-methylpyridine and in acetylene cyclotrimerization to benzene only if CO-CpRh and CO-IndRh catalysts are used, i.e., in cycles in which the intermediates and transition states possess no symmetry. Conversely when comparing CpRh- and IndRh-catalyzed acetylene cyclotrimerization to benzene, in which almost all intermediates and transition states have pseudo-C_S symmetry, no indenyl effect is predicted; when replacing the hydrocarbon Cp and Ind with the diheteroaromatic Ab and Abi, the TOF value of the catalytic cycle decreases.

The results point out that lowering the molecular symmetry, through significant hapticity deviations from the ideal η^5, reduces the catalyst's performance. This suggests the existence of a relationship between the reactivity and the metal slippage, which is the essence of the proposed *slippage span* model. We have defined a new slippage parameter, the label independent slippage parameter (LISP), which is also valid for, and applicable to non-symmetric metal displacements. Our computations reveal an inverse proportional relationship between the TOF and the ΔLISP, that is, the slippage span or difference between maximum and minimum LISP along a catalytic cycle.

The proposed *slippage span* model can serve as a guideline for the rational design of a performant half-sandwich, group 9 metal catalyst for [2+2+2] cycloadditions.

4.5 Addendum

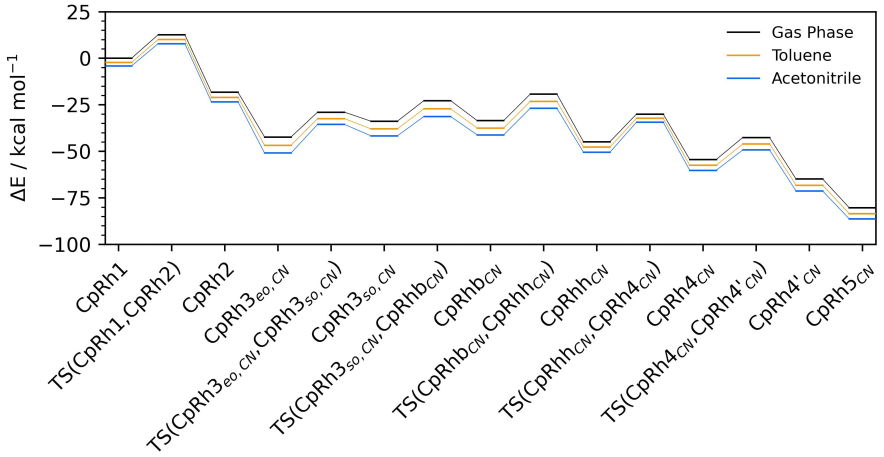

Figure S 4.1. Energy profile of acetylene/acetonitrile [2+2+2] cocycloaddition catalyzed by CpRh with different solvent: gas phase, toluene and acetonitrile (level of theory (COSMO)-ZORA-BLYP/TZ2P).

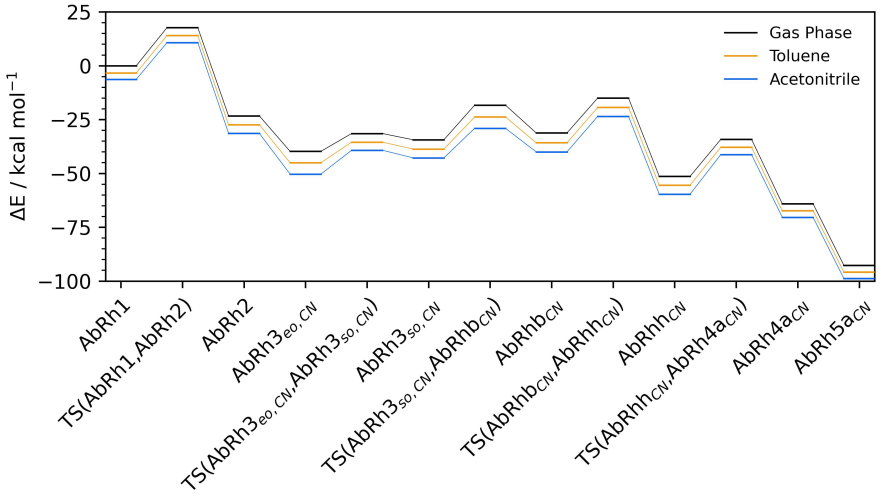

Figure S 4.2. Energy profile of acetylene/acetonitrile [2+2+2] cocycloaddition catalyzed by AbRh with different solvent: gas phase, toluene and acetonitrile (level of theory (COSMO)-ZORA-BLYP/TZ2P).

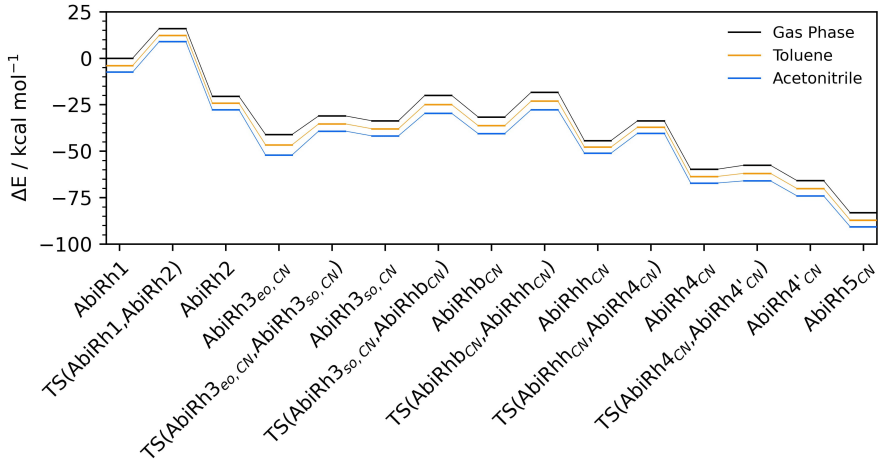

Figure S 4.3. Energy profile of acetylene/acetonitrile [2+2+2] cocycloaddition catalyzed by AbiRh with different solvent: gas phase, toluene and acetonitrile (level of theory (COSMO)-ZORA-BLYP/TZ2P).

5 Radical scavenging potential of phenothiazine scaffolds

5.1 Introduction

Oxidative stress is a pathological condition due to an unbalanced concentration of highly oxidant species in the cell, like peroxides and harmful radicals, which can react with phospholipids, proteins and nucleic acids impairing their function [115–120]. The antioxidant defense system cannot efficiently maintain the redox equilibrium inside the cell, so that its components are irreversibly damaged. Oxidative stress is found in numerous diseases of different gravity, from inflammatory processes to diabetes, cardiovascular and autoimmune diseases, cancer and neurodegenerative diseases [121–125]. Oxidative stress also accompanies several severe mental disorders, like depression, schizophrenia, even certain dependencies [126]. This is not surprising because the brain is particularly vulnerable to oxidative stress, due to

its large oxygen consumption. It is not clear whether oxidative stress is a cause or a consequence of the pathological condition, and no treatment can be exclusively tailored to fight oxidative stress. Anyway, there is clinical evidence that a regular intake of antioxidant dietary supplements has beneficial effects on the therapeutic efficacy and patient outcome.

It has been recently reported that some well-known psychotropic drugs possess antioxidant activity as radical scavengers. Zolpidem, a diffuse hypnotic, is more efficient than melatonin in quenching hydroxyl and alkoxyl radicals [127], while fluoxetine, better known with its commercial name 'Prozac' is the molecule which has revolutionized the approach to depression treatment and possesses a discrete antioxidant capacity but rather exerts this added function by increasing the levels of free serotonin, a strong radical scavenger [128]. Based on these examples, the administration of these drugs may have beneficial effects adding value to the therapeutic approach. These results, which stem firstly by clinical observation, have been rationalized at chemical level using *in silico* approaches. Despite the physiological environment is highly complex, molecular studies on the antioxidant capacity of a substance are a valuable first approach to *in vivo* and clinical testing. One of the most important advantages of *in silico* approaches rather than *in vitro* ones is the possibility of screening a large number of molecules at a reduced time and price cost. In addition, a detailed computational analysis, carried out at an accurate level of theory, allows to rationalize the results, thus providing information and guidelines for designing more efficient antioxidants.

In this chapter, we have studied the antioxidant potential of the scaffold of a very important class of antipsychotic drugs, i.e. phenothiazines (Figure 5.1, PS/PSE/PTE). Actually, different derivatives of these heterocyclic compounds find application in different medical fields, as antihistaminics (promethazine, Figure 5.1, A), sedatives (chlorpromethazine, Figure 5.1, B), anthelminthics. An

important derivative is methylene blue (Figure 5.1, C), which was first synthesized in 1876 and used by Ehlrich to distinguish bacteria, among which the malaria pathogen. Ehrlich proposed to use methylene blue in the treatment of malaria and, after testing, it was used for this purpose till the Second World War. Recently, it has been proposed again for malaria treatment [129] due to its low cost and as attempt to combat drug resistance [130].

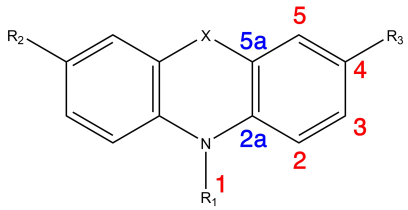

	X	R_1	R_2	R_3
PS:	S	-H	-H	-H
PSE:	Se	-H	-H	-H
PTE:	Te	-H	-H	-H
A:	S		-H	-H
B:	S		-H	-H
C:	S^+	-H	$-N(CH_3)_2$	$-N(CH_3)_2$

Figure 5.1. Phenothiazine (PS), phenoselenazine (PSE), phenotellurazine (PTE), promethazine (A) Chlorpromethazine (B) and methylene blue (C). The reactive sites are shown in red and blue.

The phenothiazine scaffold finds no application, but represents the parent compound, whose activity can be regulated by different substituents. For example, in the phenothiazine derivatives used as antipsychotics, the sedative effects as well as the extrapyramidal side effects can be modulated by using different substituents at nitrogen. Since we are interested in the antioxidant potential of this class of compounds, we have introduced a chemical change, replacing sulfur with the heavier selenium and tellurium, generating phenoselenazine (PSE) and phenotellurazine (PTE), respectively. In fact, selenium organocompounds are well known antioxidants mimicking the enzymatic activity of glutathione peroxidases (GPx) and tellurium analogs are cautiously being tested for their enhanced capacity of reducing hydroperoxides, as also predicted by computational studies.

PSE and PTE were designed as ideal 'tandem' antioxidants, which can act as radical scavengers via different mechanisms, as well as GPx mimics, which can efficiently reduce H_2O_2 and hydroperoxides to water and alcohols, respectively, as recently proposed for selenoderivatives of fluoxetine [131].

5.2 Methods

All the density functional theory (DFT) [15,16] calculations have been carried out with the Gaussian 16 rev. C.01 software [132]. The used exchange-correlation (XC) functional is the M06-2X, a hybrid meta-GGA functional developed by Yan and Truhlar [133]. It contains 54% of exact Hartree-Fock (HF) exchange and has been developed to give excellent results for main group thermochemistry. This has been used in combination with the following basis sets: the 6-311++G(d,p) basis set for H, C, N, O and S atoms and the cc-pVTZ for the Se and Te [134–137]. A proper effective core potential (ECP) is also necessary for the heaviest chalcogen. The former is a Pople split-valence triple-ζ GTOs (Gaussian-type orbitals) basis set with two polarization functions (1 additional set of d orbitals on heavy atoms and one set of p orbitals on hydrogen). The cc-pVTZ instead is a Dunning's correlation-consistent triple-ζ basis set. The optimized structures of minima and transition state have been computed both in gas-phase and in solvent: in this latter case, we have used the solvation model based on density (SMD) to emulate the physiological conditions (water) and the lipidic environment (pentyl ethanoate) [138]. The obtained molecules have been subsequently verified with a vibrational analysis in order to assess the correct nature of the points located on the PES: all normal modes of the minima have real frequencies, and, in the case of transition states, there is one normal mode associated to a single imaginary frequency. The above-mentioned level of theory (SMD-M06-2X/6-311++G(d,p), cc-pVTZ(-PP)) is compatible with the QM-ORSA protocol used to calculate the overall antioxidant capability of the analyzed molecules

and this allows direct comparison to other antioxidant systems described in literature if necessary [34].

5.3 Results and discussion

Three different mechanisms of radical scavenging, i.e. Hydrogen Atom Transfer (HAT), Radical Adduct Formation (RAF), and Single Electron Transfer (SET), have been analyzed assuming that they are the possible mechanisms through which ROS quenching occurs. On the basis of molecular symmetry, there are 7 non-equivalent active sites on the phenothiazine and its derivatives (Figure 5.1): 1 is the only amino nitrogen, 4 are aromatic carbon atoms (2, 3, 4, 5) and 2 are junction carbon atoms (2a and 5a). The energetics of the three mechanisms will be described and analyzed in detail in the next paragraphs.

5.3.1 Hydrogen Atom Transfer (HAT)

Hydrogen atom transfer (HAT) is the most relevant mechanism for radical quenching. It is shown in Figure 5.2:

$$\text{Px-H} + \text{R}^{\bullet} \longrightarrow \text{Px}^{\bullet} + \text{R-H}$$

Figure 5.2. HAT mechanism where Px = PS, PSE, PTE and $\text{R}^{\bullet} = \text{HO}^{\bullet}$, $\text{HOO}^{\bullet}$, $\text{CH}_3\text{OO}^{\bullet}$.

There are 5 positions on the phenothiazine scaffold from which $\text{H}^{\bullet}$ can be generated (sites 1, 2, 3, 4, 5, Figure 5.1).

The most exergonic reaction involves the most acidic hydrogen, i.e. the amino hydrogen. The reaction Gibbs free energies associated to HAT from the aromatic sites are comparable (sites 2, 3, 4, 5, Figure 5.1) and much less negative when the hydroxyl radical is involved; they become positive when peroxyl radicals are considered, denoting that this mechanism is disfavored from a thermodynamic point of view (Table 5.1). Overall, the $\Delta\Delta G_r$ between ΔG_r associated to site 1 and the average ΔG_r computed for the four aromatic sites is almost retained

when changing radicals, chalcogens and medium and spans from 30 to 32 kcal mol^{-1} with the only exception of PTE in water. In this system, the reactions are more endergonic when the transfer happens from the aromatic positions. This is likely due to its planar conformation, differently from the bent one observed in the other cases (Figure 5.3). The planar minimum of PTE is computed only in water phase.

Table 5.1. ΔG_r for Hydrogen Atom Transfer (HAT) scavenging mechanism. All the energies are in kcal mol^{-1}. Level of theory: SMD-M06-2X/6-311++G(d,p), cc-pVTZ(-PP).

		ΔG_r - Water			ΔG_r - Lipid		
ROS	Site	S	Se	Te	S	Se	Te
	1	-39.9	-39.2	-37.4	-37.6	-36.7	-34.7
	2	-7.4	-7.7	4.0†	-5.7	-6.0	-6.4
HO•	3	-8.5	-8.6	12.2†	-6.4	-6.6	-6.5
	4	-7.8	-8.0	10.0†	-5.7	-5.9	-6.0
	5	-8.1	-8.8	4.1†	-6.1	-6.8	-7.8
	1	-7.6	-7.0	-5.2	-5.1	-4.1	-2.1
	2	24.8	24.5	36.2†	26.9	26.5	26.2
HOO•	3	23.8	23.6	44.4†	26.1	26.0	26.0
	4	24.5	24.2	42.3†	26.8	26.6	26.6
	5	24.1	23.4	36.3†	26.4	25.8	24.7
	1	-6.3	-5.6	-3.8	-3.4	-2.5	-0.5
	2	26.2	25.8	37.5†	28.5	28.2	27.8
CH_3OO•	3	25.1	24.9	45.7†	27.8	27.6	27.7
	4	25.8	25.6	43.6†	28.5	28.3	28.2
	5	25.4	24.8	37.6†	28.1	27.4	26.4

† The minimum geometry, and thus also the energies, for the aromatic radicals in water of PTE is significantly different from the bent structures computed for PS and PSE.

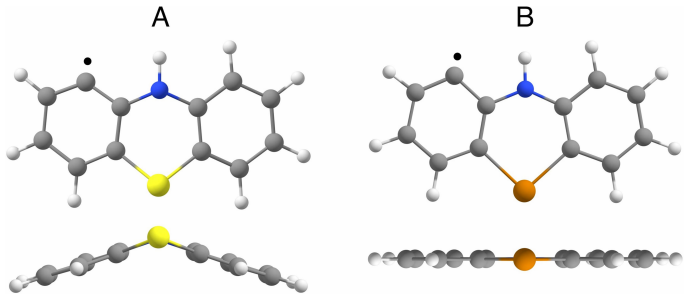

Figure 5.3. A) Minimum energy structure in water for PS radical (site 2). B) Peculiar minimum structure of PTE radical (site 2) in water: the geometry is planar. Level of theory: SMD-M06-2X/6-311++G(d,p), cc-pVTZ(-PP).

The smallest analyzed radical ($HO^{\bullet}$) is the most reactive and the only one that shows exergonic HAT reactions for all sites of the three studied scaffolds (with the sole exception of PTE in water). When considering the reactivity toward $HOO^{\bullet}$ and $CH_3OO^{\bullet}$ radicals, HAT is always highly endergonic and the only possible hydrogen abstraction with peroxyl radicals occurs from the amino site (site 1).

No clear trend emerges when changing the chalcogen but, in general, the most efficient system is PS, followed by PSE and PTE. This always holds true for HAT from site 1, but the trend is undistinguishable for the aromatic sites.

For all three radicals and all chalcogenides, the HAT mechanism seems to be only feasible (from a thermodynamic point of view) from the amino site; hence the potential energy surface (PES) has been thoroughly analyzed for this site.

Table 5.2. $\Delta G^{\ddagger}$ for Hydrogen Atom Transfer (HAT) scavenging mechanism. All the energies are in kcal mol^{-1}. Level of theory: SMD-M06-2X/6-311++G(d,p), cc-pVTZ(-PP).

		$\Delta G^{\ddagger}$ - Water			$\Delta G^{\ddagger}$ - Lipid		
ROS	Site	S	Se	Te	S	Se	Te
$HO^{\bullet}$		0.0	0.0	0.0	5.3	6.2	6.1
$HOO^{\bullet}$	1	0.0	0.0	0.0	17.2	16.8	18.0
$CH_3OO^{\bullet}$		0.0	0.0	0.0	18.7	19.0	19.6

The process in the polar environment is completely barrierless regardless the radical (Table 5.2); no effect of the chalcogen is found. However, in lipid media, the barriers are appreciable: they are rather small for HO$^{\bullet}$ but increase significantly for HOO$^{\bullet}$ and $CH_3OO^{\bullet}$ (from 17 kcal mol^{-1} to almost 20 kcal mol^{-1}, depending on the chalcogen).

5.3.2 Radical Adduct Formation (RAF)

The Radical Adduct Formation (RAF) is another important mechanism that leads to the formation of a single adduct as a product (Figure 5.4).

$$Px + R^{\bullet} \longrightarrow PxR^{\bullet}$$

Figure 5.4. RAF mechanism where Px = PS, PSE, PTE and R$^{\bullet}$ = HO$^{\bullet}$, HOO$^{\bullet}$, $CH_3OO^{\bullet}$.

In the case of the phenothiazine scaffold, this path is rather essential because the HAT mechanism is not well suited for the aromatic positions since the hydrogen transfer from the benzene rings to a ROS disrupts the aromaticity. The RAF mechanism may involve up to 6 sites (2a, 2, 3, 4, 5, 5a) on each aromatic ring. Sites 5a and 2 show the most exergonic reactions (Table 5.3). On the other hand, the three worst sites are 5 and 3. Sites 2a and 4 show intermediate thermodynamic feasibility. This trend holds true in all cases (PS, PSE, PTE) and for all the studied radicals. Also, in this case, the most reactive radical is HO$^{\bullet}$: the reactions are highly exergonic for all sites and for all the three chalcogens. HOO$^{\bullet}$ and $CH_3OO^{\bullet}$ show similar reactivity and all the involved reactions are thermodynamically disfavored.

Table 5.3. ΔG_r for Radical Adduct Formation (RAF) scavenging mechanism. All the energies are in kcal mol^{-1}. Level of theory: SMD-M06-2X/6-311++G(d,p), cc-pVTZ(-PP).

		ΔG_r - Water			ΔG_r - Lipid		
ROS	Site	S	Se	Te	S	Se	Te
HO•	2a	-9.8	-9.4	-8.6	-9.0	-8.4	-7.4
	2	-10.2	-10.5	-10.4	-10.2	-10.7	-10.7
	3	-8.3	-8.2	-7.6	-8.2	-8.1	-7.2
	4	-9.9	-10.2	-10.2	-9.7	-9.9	-9.6
	5	-8.1	-8.2	-8.6	-7.8	-8.1	-8.5
	5a	-13.3	-13.2	-38.0†	-12.6	-12.7	-39.8†
HOO•	2a	15.5	15.9	16.4	17.9	18.6	19.3
	2	15.4	14.9	14.5	16.5	16.4	15.8
	3	16.6	16.6	17.4	18.4	18.5	19.3
	4	14.6	14.0	14.6	16.3	16.2	16.5
	5	17.5	16.4	16.3	18.8	17.7	18.1
	5a	11.9	11.6	-8.0†	13.8	13.2	-7.2†
CH_3OO•	2a	18.2	18.7	19.6	21.9	22.2	23.3
	2	17.8	17.3	17.1	19.9	19.5	19.5
	3	19.1	19.3	20.0	21.6	22.2	22.8
	4	17.2	16.9	17.3	20.0	19.8	20.1
	5	19.0	19.1	19.4	22.0	21.9	22.2
	5a	15.1	14.4	-6.7†	17.5	16.8	-4.8†

† The reaction leads to the central ring opening: the original structure of the antioxidant is no longer recoverable.

The trend found for ΔG_r is recovered for $\Delta G^{\ddagger}$ as well (Table 5.4): the lowest barriers are computed for HO•, followed by HOO• and CH_3OO•. The barriers associated to the different sites roughly follow the previously described trend in ΔG_r: the smaller barriers are calculated for sites 5a and 2a, the highest ones for sites 5 and 3. Like in the HAT mechanism, the differences in terms of ΔG_r and $\Delta G^{\ddagger}$ between the polar

and apolar solvent are not so pronounced because the products of both processes are neither charged nor highly polarized. Hence, there is no overstabilization of products rather than reagents due to the solvation effect. However, a general trend is noticed because in lipid media, the barriers tend to be higher and the reactions slightly more endergonic.

Table 5.4. $\Delta G^{\ddagger}$ for Radical Adduct Formation (RAF) scavenging mechanism. All the energies are in kcal mol^{-1}. Level of theory: SMD-M06-2X/6-311++G(d,p), cc-pVTZ(-PP).

		$\Delta G^{\ddagger}$ - Water			$\Delta G^{\ddagger}$ - Lipid		
ROS	Site	S	Se	Te	S	Se	Te
HO•	2a	4.8	4.6	5.1	9.2	9.5	10.0
	2	5.7	5.5	5.4	7.6	7.6	7.6
	3	8.2	7.5	8.3	10.4	10.3	10.5
	4	5.9	5.7	5.5	8.4	8.3	8.5
	5	9.1	8.9	8.8	10.7	10.4	10.2
	5a	4.2	4.5	4.9†	8.5	8.6	9.1†
HOO•	2a	22.3	22.2	22.7	26.2	26.6	26.8
	2	23.3	22.9	22.6	25.6	25.5	25.4
	3	24.8	24.7	25.2	27.3	27.5	28.1
	4	21.6	21.5	21.3	24.9	24.9	25.0
	5	25.2	24.3	24.5	27.3	26.9	26.7
	5a	21.3	21.2	21.3†	24.7	24.8	24.9†
CH_3OO•	2a	24.8	25.1	25.6	29.9	30.2	30.7
	2	25.1	24.9	24.8	28.7	28.5	28.5
	3	27.1	27.3	27.7	30.8	31.1	31.5
	4	23.9	23.6	23.9	28.1	28.1	28.5
	5	26.6	26.6	27.0	30.1	30.4	30.6
	5a	23.9	24.0	24.5†	28.5	28.7	29.3†

† The reaction leads to the central ring-opening: the original molecule of antioxidant is no longer recoverable.

It is worth to notice that in PTE, the attack of the ROS to site 5a is not possible: the process involves the opening of the ring and the subsequent and irreversible loss of the original antioxidant molecule. This happens with all the three screened radicals and in both solvents.

5.3.3 Single Electron Transfer (SET)

The Single Electron Transfer (SET) is the only mechanism that doesn't require nuclear displacements and, for this reason, the canonical minimization for the transition state localization is impracticable. However, Marcus theory is well suited for this purpose. The mechanism is reported in Figure 5.5:

$$Px + R^{\bullet} \longrightarrow Px^{\bullet +} + R^{-}$$

Figure 5.5. SET mechanism where Px = PS, PSE, PTE and $R^{\bullet}$ = $HO^{\bullet}$, $HOO^{\bullet}$, $CH_3OO^{\bullet}$.

In gas phase, this mechanism is highly unlikely due to the large positive ΔG_r values (in the best-case scenario, i.e. PS + $OH^{\bullet}$, the reaction is neatly endergonic and ΔG_r exceeds 120 kcal mol^{-1}). The reason can be ascribed to the formation of highly destabilized products, i.e. charged radical species. Thus, the overall contribution of SET to scavenging activity in gas phase and in lipid media is negligible. However, this is not true in a polar environment (Table 5.5): in water the charged products are strongly stabilized, and the SET becomes exergonic in the case of $HO^{\bullet}$. As for the previously described mechanisms, this radical is the most active one, regardless the involved chalcogen. Conversely, the processes involving hydroperoxyl ($HOO^{\bullet}$) and methylperoxyl radical ($CH_3OO^{\bullet}$) are endergonic.

Table 5.5. ΔG_r for Single Electron Transfer (SET) scavenging mechanism. All the energies are in kcal mol^{-1}. Level of theory: SMD-M06-2X/6-311++G(d,p), cc-pVTZ(-PP).

	ΔG_r - Water			ΔG_r - Lipid		
ROS	S	Se	Te	S	Se	Te
HO•	-10.6	-13.0	-16.7	33.3	31.0	28.9
HOO•	11.5	9.0	5.3	52.7	50.4	48.3
CH_3OO•	13.3	10.8	7.1	54.0	51.7	49.5

In water, the reaction with HO• is almost barrierless (Table 5.6) and, for this reason, SET contributes to the overall antioxidant activity regardless the chalcogen present in the scaffold (Table 5.9). Two details are remarkable: the first one is related to the observed chalcogen trend and the second one deals with the Marcus region for two particular cases. SET is the first mechanism with a clear trend in exergonicity and in terms of transition states energies: Tellurium-based systems appear to be more favored from both thermodynamic and kinetic points of view. The presence of the lighter chalcogen, instead, is associated to the less efficient SET, similarly to the PSE case. The only exception in the barriers trend is found when comparing the cases of PSE and PTE with the hydroxyl radical. This can be explained because the reorganization energy is in both cases much smaller compared to the absolute value of ΔG_r and therefore, these two processes occur in the Marcus inverted region, where the greater the exergonicity of reaction, the larger the barrier.

Table 5.6. $\Delta G^{\ddagger}$ for Single Electron Transfer (SET) scavenging mechanism. All the energies are in kcal mol^{-1}. Level of theory: SMD-M06-2X/6-311++G(d,p), cc-pVTZ(-PP).

	$\Delta G^{\ddagger}$ - Water			$\Delta G^{\ddagger}$ - Lipid		
ROS	S	Se	Te	S	Se	Te
$HO^{\bullet}$	0.0	0.1†	5.7†	46.6	41.3	50.7
$HOO^{\bullet}$	12.9	11.2	7.4	63.6	59.5	61.5
$CH_3OO^{\bullet}$	14.2	12.4	8.5	65.6	61.4	63.6

† The reaction lies in the Marcus inverted region because the reorganization energy λ is smaller than the absolute value of ΔG_r.

5.3.4 Direct oxidation of the chalcogen center

In the previous paragraphs, we have seen how different ROS can be quenched with different mechanisms and by different substrates. From this analysis, it emerges that the smaller attacking radical, i.e. hydroxyl radical, is the more efficient regardless of the media and the involved chalcogen. The poor selectivity of $HO^{\bullet}$ is well known in literature. This ROS is an extremely effective one-electron oxidizing agent and the involved reactions are commonly limited by its diffusion ($k > 10^9$ M^{-1} s^{-1}) [139–141]. A very short half-life (10^{-9} s) [142] and a large and positive one-electron reduction potential (2.31V at physiological pH) [143] demonstrate its high reactivity and, consequently, the low selectivity towards the substrate. In general, alkoxyl radicals $RO^{\bullet}$ tends to retain this characteristic but in a much more modest way: they are less active compared to $HO^{\bullet}$ but they are more reactive than peroxyl radicals $ROO^{\bullet}$. A conversion of the latter is possible with a direct oxidation of the chalcogen center on PS, PSE and PTE according to Figure 5.6:

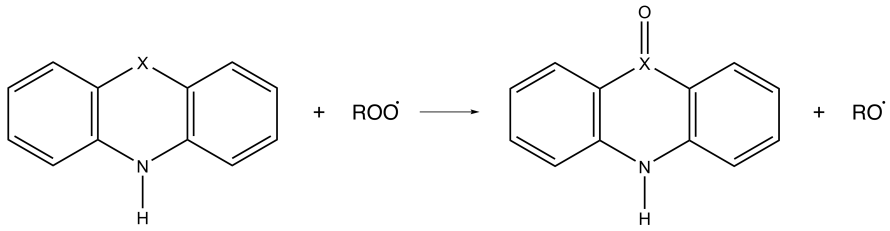

Figure 5.6. Direct oxidation of phenothiazine (X=S, PS), phenoselenazine (X=Se, PSE) and phenotellurazine (X=Te, PTE) by a peroxyl radicals ROO•.

From a mere theoretical point of view, this reaction path could in principle enhance the overall antioxidant activity of PS, PSE and PTE due to the conversion of the ROS from a relatively poorly reactive peroxyl radical to an alkoxyl radical. In the particular case of hydroperoxyl radical, the product is an extremely reactive hydroxyl radical molecule. The nature of newly formed oxidized molecule and, in particular, of the sulfoxide, selenoxide and telluroxide bond X=O (X=S, Se, Te) is best described by a polarized σ bond rather than a simple double bond. For this reason, due to the formation of a positive partial charge on X and a negative on O, the molecule does not exhibit a classical hypervalency. The strength of the X=O bond is related to the involved electrostatic interactions between the two atoms and tend to decrease from X=S to X=Te [144]. In our systems, the direct oxidation is an exergonic process for almost all cases (Table 5.7) with the only exception of PS + HOO• in lipidic media.

Table 5.7. ΔG_r for the direct oxidation of the chalcogen by HOO• and CH_3OO• radicals. All the energies are in kcal mol^{-1}. Level of theory: SMD-M06-2X/6-311++G(d,p), cc-pVTZ(-PP).

	ΔG_r - Water			ΔG_r - Lipid		
ROS	S	Se	Te	S	Se	Te
HOO•	-5.3	-12.0	-18.4	0.9	-1.6	-5.3
CH_3OO•	-12.2	-18.9	-25.3	-5.9	-8.3	-12.1

The reaction is thermodynamically favored in physiological environment and in the presence of alkylperoxyl radicals. All the previously explored mechanisms (HAT, RAF and SET) in which the $HOO^{\bullet}$ and $CH_3OO^{\bullet}$ radicals are being involved show much more endergonic reactions. However, the direct oxidation requires rather prohibitive activation energies under standard conditions (Table 5.8). In the best scenario (PTE with $HOO^{\bullet}$ in water), $\Delta G^{\ddagger}$ is about 12 kcal mol^{-1} and considering a barrierless process, such as HAT in our systems, the contribution to the overall antioxidant activity of a mechanism involving the direct oxidation of the chalcogen and subsequent scavenging has to be considered extremely limited.

Table 5.8. $\Delta G^{\ddagger}$ for the direct oxidation of the chalcogen by $HOO^{\bullet}$ and $CH_3OO^{\bullet}$ radicals. All the energies are in kcal mol^{-1}. Level of theory: SMD-M06-2X/6-311++G(d,p), cc-pVTZ(-PP).

	$\Delta G^{\ddagger}$ - Water			$\Delta G^{\ddagger}$ - Lipid		
ROS	S	Se	Te	S	Se	Te
$HOO^{\bullet}$	31.5	23.6	11.9	38.2	30.8	21.1
$CH_3OO^{\bullet}$	34.4	26.9	15.5	42.1	35.4	24.8

5.3.5 Kinetic constants and antioxidant activity

According to the QM-ORSA protocol described in the material and methods section, the kinetic constants have been calculated for both the solvents in order to assess the overall antioxidant capability and to make comparison with data reported in literature for other systems. The apparent kinetic constants in water were computed and are summarized in Table 5.9. For HAT mechanism, only site 1 has been taken into account: the kinetic constant of transfers involving aromatic hydrogens are orders of magnitude smaller when compared to the one of the amino sites. HAT is the primary mechanism for the bigger radicals (hydroperoxyl and methyl peroxyl radical) for PS and PSE. The RAF mechanism, instead, is the favored mechanism for the hydroxyl radical and this could be mainly ascribed to the number of available positions

on the aromatic rings (also considering the degenerate pathways due to the symmetry) and shallow barriers. Unfortunately, the barriers increase significantly with the peroxyl radicals and thus, the contribution of RAF to the overall activity is negligible for $HOO^{\bullet}$ and $CH_3OO^{\bullet}$. However, the combination of these two radicals and PTE is the most efficient case for SET.

Table 5.9. Kinetic constants for the analyzed mechanisms in water at 298.15K. All the kinetic constants are in M^{-1} s^{-1}. The branching ratio is reported in brackets.

		k_{app} - Water		
	ROS	PS	PSE	PTE
HAT	$HO^{\bullet}$	$2.61 \cdot 10^{9}$ (3%)†	$2.63 \cdot 10^{9}$ (3%)†	$2.58 \cdot 10^{9}$ (3%)†
	$HOO^{\bullet}$	$1.96 \cdot 10^{9}$ (100%)†	$1.98 \cdot 10^{9}$ (97%)†	$1.96 \cdot 10^{9}$ (23%)†
	$CH_3OO^{\bullet}$	$1.69 \cdot 10^{9}$ (100%)†	$1.69 \cdot 10^{9}$ (99%)†	$1.68 \cdot 10^{9}$ (32%)†
RAF	$HO^{\bullet}$	$6.88 \cdot 10^{10}$ (86%)†	$7.18 \cdot 10^{10}$ (87%)†	$7.01 \cdot 10^{10}$ (86%)†
	$HOO^{\bullet}$	$2.11 \cdot 10^{1}$ (0%)	$2.48 \cdot 10^{1}$ (0%)	$2.42 \cdot 10^{1}$ (0%)
	$CH_3OO^{\bullet}$	$3.10 \cdot 10^{-1}$ (0%)	$3.70 \cdot 10^{-1}$ (0%)	$2.28 \cdot 10^{-1}$ (0%)
SET	$HO^{\bullet}$	$8.53 \cdot 10^{9}$ (11%)†	$8.47 \cdot 10^{9}$ (10%)†	$8.43 \cdot 10^{9}$ (10%)†
	$HOO^{\bullet}$	$3.61 \cdot 10^{6}$ (0%)	$6.98 \cdot 10^{7}$ (3%)	$6.75 \cdot 10^{9}$ (77%)†
	$CH_3OO^{\bullet}$	$4.15 \cdot 10^{5}$ (0%)	$9.69 \cdot 10^{6}$ (1%)	$3.50 \cdot 10^{9}$ (68%)†
OVERALL	$HO^{\bullet}$	$7.99 \cdot 10^{10}$ †	$8.30 \cdot 10^{10}$ †	$8.11 \cdot 10^{10}$ †
	$HOO^{\bullet}$	$1.96 \cdot 10^{9}$ †	$2.05 \cdot 10^{9}$ †	$8.72 \cdot 10^{9}$ †
	$CH_3OO^{\bullet}$	$1.69 \cdot 10^{9}$ †	$1.70 \cdot 10^{9}$ †	$5.18 \cdot 10^{9}$ †

† Diffusion-controlled reaction.

The global antioxidant activity is given by the sum of the k_{app} for all considered mechanisms: in physiological conditions, the sum of all thermal constants exceeds the value estimated for diffusion and therefore, all processes are limited by the latter. Unfortunately, this rules out the fine-tuning possibility of the antioxidant capacities by a simple modification of the chalcogen and therefore, the scavenging capacity is determined by the radical's ability to diffuse in water.

In a lipidic environment, the situation is less diversified than in the water system (Table 5.10): the HAT mechanism is the favored reaction pathway only for the larger radicals ($HOO^{\bullet}$ and $CH_3OO^{\bullet}$) and, as seen before, the most active radical reacts via RAF. In this case, the branching ratios, are highly independent from the chalcogen in the antioxidant. The lipid medium is not able to stabilize the charged products deriving from SET and, as a consequence, this mechanism is energetically unfavorable both from the thermodynamic and kinetic points of view.

Table 5.10. Kinetic constants for the analyzed mechanisms in pentyl ethanoate at 298.15K. All the kinetic constants are in M^{-1} s^{-1}. The branching ratio is reported in brackets.

		k_{app} - Lipid		
	Radical	S	Se	Te
HAT	$HO^{\bullet}$	$2.88 \cdot 10^{9}$ (7%)†	$2.89 \cdot 10^{9}$ (7%)†	$2.80 \cdot 10^{9}$ (8%)†
	$HOO^{\bullet}$	$2.62 \cdot 10^{3}$ (100%)	$5.71 \cdot 10^{3}$ (100%)	$7.26 \cdot 10^{2}$ (100%)
	$CH_3OO^{\bullet}$	$2.10 \cdot 10^{2}$ (100%)	$1.40 \cdot 10^{2}$ (100%)	$5.23 \cdot 10^{1}$ (100%)
RAF	$HO^{\bullet}$	$3.81 \cdot 10^{10}$ (93%)†	$3.75 \cdot 10^{10}$ (93%)†	$3.14 \cdot 10^{10}$ (92%)†
	$HOO^{\bullet}$	$7.44 \cdot 10^{-2}$ (0%)	$6.64 \cdot 10^{-2}$ (0%)	$5.77 \cdot 10^{-2}$ (0%)
	$CH_3OO^{\bullet}$	$2.19 \cdot 10^{-4}$ (0%)	$2.15 \cdot 10^{-4}$ (0%)	$1.39 \cdot 10^{-4}$ (0%)
SET	$HO^{\bullet}$	$8.11 \cdot 10^{-19}$ (0%)	$6.08 \cdot 10^{-15}$ (0%)	$7.26 \cdot 10^{-22}$ (0%)
	$HOO^{\bullet}$	$2.51 \cdot 10^{-31}$ (0%)	$2.65 \cdot 10^{-28}$ (0%)	$9.52 \cdot 10^{-30}$ (0%)
	$CH_3OO^{\bullet}$	$9.31 \cdot 10^{-33}$ (0%)	$1.08 \cdot 10^{-29}$ (0%)	$2.83 \cdot 10^{-31}$ (0%)
OVERALL	$HO^{\bullet}$	$4.09 \cdot 10^{10}$ †	$4.04 \cdot 10^{10}$ †	$3.42 \cdot 10^{10}$ †
	$HOO^{\bullet}$	$2.62 \cdot 10^{3}$	$5.71 \cdot 10^{3}$	$7.26 \cdot 10^{2}$
	$CH_3OO^{\bullet}$	$2.10 \cdot 10^{2}$	$1.40 \cdot 10^{2}$	$5.23 \cdot 10^{1}$

† Diffusion-controlled reaction.

The antioxidant capacity in apolar environment results comparable to that computed in water only when considering the hydroxyl radical. The selectivity towards peroxyl radicals is strongly reduced.

In order to better understand the calculated kinetic constants for PS, PSE and PTE, a comparison to few well-known antioxidant molecules has been made (Table 5.11). In aqueous solution, the activity towards the $HO^{\bullet}$ radical shows reaction rates that are approaching the diffusion rate limit: this is a common point also found for glutathione, sesamol, caffeine, melatonin, DHMBA, Trolox and edaravone. Calculating an accurate kinetic constant strongly depends on the approximation used to estimate the rate of diffusion in a particular media: the most challenging parameter to assess and for which, to the best of our knowledge, there is no accurate technique of evaluation, is the reactants Stokes radius that defines both the diffusion coefficients.

Table 5.11. Calculated and experimental kinetic rate constants for the quenching activity of several antioxidant molecules towards different ROSs. All the kinetic constants are in M^{-1} s^{-1}.

Substrate	ROS	Solvent	k_{calc}	k_{exp}
PS	$HO^{\bullet}$	Aqueous	$7.99 \cdot 10^{10}$	
PSE	$HO^{\bullet}$	Aqueous	$8.30 \cdot 10^{10}$	
PTE	$HO^{\bullet}$	Aqueous	$8.11 \cdot 10^{10}$	
Glutathione	$HO^{\bullet}$	Aqueous	$7.68 \cdot 10^{9}$ [145]	$8.72 \cdot 10^{9}$ [146–148]
Glutathione	$CH_3O^{\bullet}$	Aqueous	$5.89 \cdot 10^{8}$ [145]	$9.00 \cdot 10^{8}$ [149]
Glutathione	$HOO^{\bullet}$	Aqueous	$2.69 \cdot 10^{7}$ [145]	
Glutathione	$CH_3OO^{\bullet}$	Aqueous	$2.02 \cdot 10^{4}$ [145]	
Sesamol	$HO^{\bullet}$	Aqueous	$2.37 \cdot 10^{10}$ [150]	$1.10 \cdot 10^{10}$ [151]
Sesamol	$HOO^{\bullet}$	Aqueous	$6.36 \cdot 10^{7}$ [150]	
Caffeine	$HO^{\bullet}$	Aqueous	$2.15 \cdot 10^{9}$ [152]	$5.60 \cdot 10^{9}$ [153–155]
Melatonin	$HO^{\bullet}$	Aqueous	$1.85 \cdot 10^{10}$ [156,157]	$3.04 \cdot 10^{10}$ [158–162]
DHMBA	$HOO^{\bullet}$	Aqueous	$1.34 \cdot 10^{9}$ [163]	
Capsaicin	$ROO^{\bullet}$	Mixed	$6.50 \cdot 10^{3}$ [164]	$5.60 \cdot 10^{3}$ [165]
Tyrosol	$ROO^{\bullet}$	Aqueous	$4.30 \cdot 10^{3}$ [166]	$9.40 \cdot 10^{3}$ [167]
Trolox	$HO^{\bullet}$	Aqueous	$2.78 \cdot 10^{10}$ [165]	$8.10 \cdot 10^{10}$ [168]
Edaravone	$HO^{\bullet}$	Aqueous	$1.35 \cdot 10^{10}$ [169]	$1.93 \cdot 10^{9}$ [170,171]

Changing ROS ($HOO^{\bullet}$, $ROO^{\bullet}$) usually leads to a decrease of the antioxidant capabilities; however, this heavily depends on the substrate structure. For instance, PS, PSE and PTE show no HAT barrier for the amino hydrogen (site 1) and this is the only reason explaining the outstanding performance towards less active radicals, i.e. $HOO^{\bullet}$ and $CH_3OO^{\bullet}$. In a similar fashion, we can find an analogy with the 3,5-dihydroxy-4-methoxybenzyl alcohol (DHMBA): one of the hydroxy groups exhibits barrierless process via HAT and, as a primary consequence, the involved kinetic rate constant for the $HOO^{\bullet}$ quenching, easily reaches the diffusion regime. On the other hand, in lipid media, where the NH hydrogen abstraction becomes an activated process (especially for $HOO^{\bullet}$ and $CH_3OO^{\bullet}$), the overall activity of PS, PSE and PTE is close to what we find in capsaicin or tyrosol. Finally, another general observation, which is also in agreement with the data reported literature for other scavengers, is the poor selectivity of alkoxyl radicals, especially $HO^{\bullet}$, versus the low reactivity of the peroxyl radicals.

5.4 Conclusions

In this chapter, we have analyzed in silico the scavenging activity of the phenothiazine scaffold and its selenium and tellurium derivatives. The idea of chemically modifying this system, which is the parent molecular structure of a well-known class of psychotropic and antihistaminic drugs, introducing selenium aims at improving its antioxidant action with beneficial therapeutic consequences. Differently from what reported in other cases, i.e. selenofluoxetine vs fluoxetine [131], the presence of a different chalcogen does not lead to enhanced activity via the three considered mechanisms, i.e. HAT, RAF and SET. In addition, an alternative path consisting in the direct oxidation of the chalcogen followed by the ROS quenching mechanisms is here discussed but excluded, due to the unfavored energetics. While the presence of substituents of the rings, which is a characteristic of the real drugs, can

modify the electronic structure and directly affect the scavenging potential, as well as the replacement of the amino hydrogen with an alkyl pendant, we conclude that the phenothiazine scaffold is a rather good scavenger for $HO^{\bullet}$, comparable to well-established antioxidants like melatonin and Trolox, but is not effective for peroxyl radicals.

6 Thiol oxidation in proteins: a model molecular study based on GPx4

6.1 Introduction

In recent years, selenium redox chemistry has stepped into the limelight. Besides the fundamental role organoselenides have in organic catalysis [172], particularly in oxidations of substrates by H_2O_2 [173], selenium-mediated redox reactions are key steps in biological processes related to oxidative stress control and signaling [174]. There is general consensus that in the redox behavior of selenium, which differs significantly from that of sulfur and tellurium [175,176], a plausible justification of the presence of this oligoelement in some proteins can be found [177].

Among the 25 human genes encoding selenoproteins discovered so far, glutathione peroxidases are a family of important enzymes able to reduce H_2O_2 and hydroperoxides to water or the corresponding alcohols, respectively [178–180]. The mechanistic details have been thoroughly investigated in the last decade in computer-assisted studies [181–184] and experimental results and modeling nicely agree, at least on the first step, i.e., the oxidation of the selenocysteine of the active site to selenenic acid with concomitant reduction of the peroxide. In fact, not only the presence of selenium rather than sulfur leads to a more favorable energetics and kinetics [185], explaining the drop of efficiency observed in GPx sulfur mutants. In addition, a two-step mechanism has been pinpointed, which explains the incredibly fast reactivity of GPx [180,186,187], where more simple explanations based on acidity and nucleophilicity difference of Sec vs Cys remain too qualitative. The selenol proton can be shuttled to a close acceptor, identified in the highly conserved Trp residue in all GPx, leading to a high energy zwitterionic form, in which the selenolate anion has enhanced nucleophilic power compared to the neutral selenol. The process is mediated by at least one water molecule and the hydrogen bond network in the enzymatic cavity is responsible for the stability of the charge separated intermediate. The peroxide bond disruptor occurs by nucleophilic attack of the chalcogenolate to one O atom, while the proton back-transfer to the other O atom creates the optimal leaving group, i.e., a water molecule. This mechanism was very recently assessed in four families of (selenol)thiol-based proteins and thus can be considered of more general validity for enzymes containing peroxidatic cysteines [188]. While the proton dislocation is an activated process with barriers ranging approximately from 15 to 30 kcal mol^{-1}, we found that the S_N2 step occurs easily without appreciable barrier. Prompted by curiosity of rationalizing this latter outcome, which might be ascribed to an effect of the enzymatic environment, we have built a bioinspired molecular model based on the GPx catalytic pocket, for which our previous data [182] are available for direct comparison.

In this chapter, we present the results of the H_2O_2 reduction in very simple models built from GPx structures and, besides reinforcing the advantages of selenium rather than sulfur, rooting nature's choice in the chalcogen chemistry, we indirectly assess the unique role of the conserved residues in GPx in promoting and enhancing selenium capacity of reducing hydroperoxides.

6.2 Methods

Density functional theory (DFT) methods have been used to carry out geometry optimizations and transition state searches, as implemented in Gaussian 16 rev. C.01 [132] and ADF 2019 suites [77–79]. The exchange-correlation (XC) potential employed in this work is the hybrid GGA B3LYP functional [189–192] with the D3(BJ) dispersion correction developed by Grimme et al. [28,29]. This method has been chosen also to be fully consistent with previous calculations carried out on a cluster of amino acids representing the GPx4 enzymatic pocket. The 6-311G(d,p) basis set [134] has been used to describe all atoms except selenium. This is an extended Pople style GTOs (Gaussian-type orbitals) basis set, and it is characterized by a split-valence triple-ζ quality with one set of polarization functions on each atom (1 additional set of d orbitals on heavy atoms and one set of p orbitals on hydrogen). The selenium atom, instead, has been described with cc-PVTZ, the very popular Dunning's correlation-consistent triple-ζ basis set [136]. All the geometry optimizations have been performed in gas phase and, in order to improve the accuracy of the final energy, single points were carried out in condensed phase with the 6-311+G(d,p)/cc-PVTZ basis sets. The calculations in condensed phase have been performed with the Minnesota Solvation Model based on Density (SMD) developed by Truhlar and coworkers [138]. Water has been chosen as the main solvent in order to mimic the physiological environment. A classical vibrational analysis has been carried out for all stationary points. Particularly, in order to ensure that the correct transition states have been found, the

single normal mode associated to the negative force constant (and imaginary frequency) has been verified. For an in-depth analysis on a reduced model system we used ADF, along with Activation Strain Model (ASM) [20].

6.3 Results and discussion

The first step of the Cys-GPx and Sec-GPx mechanism is a keystone passage of the whole enzymatic process, because it is the stage at which the reduction of the peroxide occurs, and the enzyme explicates its function. It is justified to consider the first step of the catalytic cycle separately, since kinetic measurements reveal that the individual steps are not influenced by the respective co-substrate [181,186]. As illustrated in the introduction, this reduction is actually a two-step process, that is a proton transfer, which allows deprotonation of the (selenol)thiol, followed by a S_N2, leading to the peroxide bond breaking, selenenic(sulfenic) acid formation and generation of a water molecule. We designed a molecular model that includes the essential fragments for the stepwise reduction and maintains the topological features of the catalytic pocket of Cys and Sec glutathione peroxidases, as obtained by molecular dynamics (MD) simulations of GPx4 [182]. In the enzyme, the proton transfer occurs from Sec45 to the indole nitrogen of Trp136 (residue numbering of human GPx4; Figure 6.1 A and B) and is mediated by one molecule of hydrogen peroxide and one molecule of water [182–184]. Our model is composed by an indole, mimicking Trp136, a water molecule, a H_2O_2 molecule and ethaneselenol(thiol) (**X-1**, Figure 6.1 C).

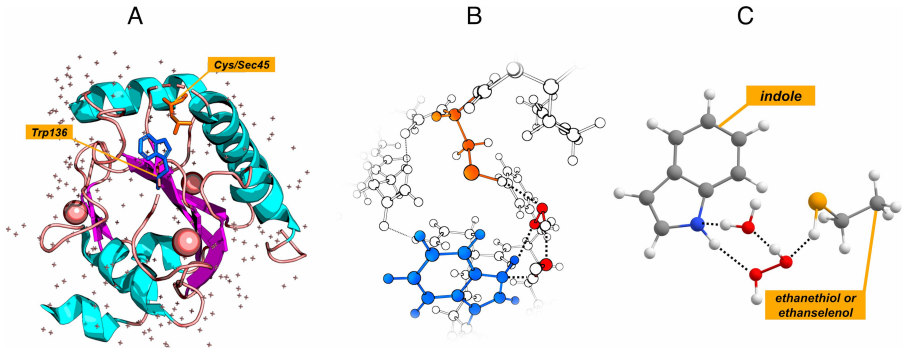

Figure 6.1. A) The human GPx4 enzyme [182,193]; Sec45 and Trp136 are explicitly shown in orange and blue, respectively. B) Details of the catalytic pocket of the human GPx4. C) Our minimal molecular model of the Cys/Sec-GPx catalytic pocket (X-1, X = S, Se): ethaneselenol(thiol) and indole molecules are arranged in space to retain the exact geometry of the corresponding residues in GPx4.

When the selenol/thiol proton is shuttled to the indole nitrogen, the zwitterionic species (**X-2$_{CS}$**, X=S, Se) forms. The ethaneselenolate(thiolate) of **X-2$_{CS}$** is a strong nucleophile due to the acquired negative charge. In this condition, a nucleophilic attack may easily occur leading to the O-O cleavage of the peroxide substrate and the formation of the selenenic(sulfenic) acid, while the back-transfer of the proton dislocated on indole to the second O atom favors the cleavage of a water molecule; this final state is labeled as **X-3** (X = S, Se). The whole two-step process is fully consistent with the description of the oxidative step of GPx4 and is shown in Figure 6.2.

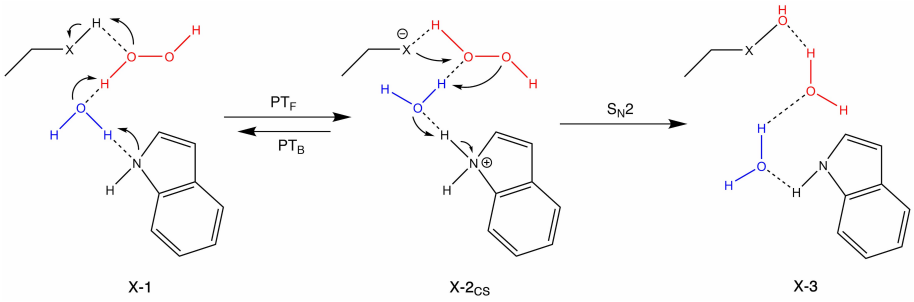

Figure 6.2. Starting from X-1, the first elementary step is a proton transfer (PTF) mediated by the oxygen atoms of the H_2O_2 and H_2O molecules. The

product is the zwitterionic form of the initial reactants (X-2_{CS}). From X-2_{CS}, a S_N2 reaction takes place and the selenenic(sulfenic) acid (together with indole and two water molecules) forms (X-3); X=S, Se.

Table 6.1. Energy values referring to proton transfer for the formation of the zwitterionic intermediate X-2_{CS} in the two model systems used to mimic Cys-GPx and Sec-GPx. ΔG is in kcal mol^{-1} and all values are relative to the initial state X-1. Level of theory: SMD-B3LYP-D3(BJ)/6-311+G(d,p), cc-pVTZ// B3LYP-D3(BJ)/6-311G(d,p), cc-pVTZ.

	X=S	Cys-GPx	X=Se	Sec-GPx
	ΔG_{solv}	ΔG_{solv}†	ΔG_{solv}	ΔG_{solv}†
X-1	0.00	0.00	0.00	0.00
X-TS(1, 2_{CS})	57.05	27.10	44.42	21.60
X-2_{CS}	42.81	18.30	28.90	11.40

† Taken from Ref. [182].

In this set of calculations, all the atoms have been kept frozen in the positions they have in the residues of the GPx pocket and only the H atoms were free to move. Both **S-2_{CS}** and **Se-2_{CS}** form, and the energetics is reported in Table 6.1.The barriers are much higher when compared to those reported in the literature for the corresponding enzymatic clusters [182], and this is due drastic reduction of the atoms' degrees of freedom compared to the fully unconstrained biological system. However, the energy trends are coherent for both transition state and product energies. In fact, the activation energy for the conversion of **Se-1** is smaller, and the corresponding charge separated product **Se-2_{CS}** is approximately 10 kcal mol^{-1} more stable compared to the S-based one. In this case, it was impossible to proceed further and analyze the subsequent step (S_N2) because the oxygen nuclei were not allowed to move by choice.

Thus, a second set of calculations were carried out on the same model (Table 6.1 C) but removing the constraints on the oxygen atoms.

Unexpectedly, we were unable to obtain the **S-2$_{CS}$** intermediate and all attempts lead to the initial neutral structure **S-1**. Thus, no mechanistic path was found for the peroxide reduction in the S-based model system.

Differently from the previous case, the reaction path leading to the zwitterionic intermediate **Se-2$_{CS}$** requires a hydrogen rotation in H_2O_2 and this leads to the formation of the intermediate **Se-2**, passing through **Se-TS(1,2$_{CS}$)** with a very small barrier (0.32 kcal mol^{-1}). This step is necessary for the subsequent forward proton transfer (PT_F) and any attempt to find the transition state connecting to **Se-2$_{CS}$** without invoking the formation of **Se-2** failed. Once the zwitterionic intermediate is formed, two possible evolutions can be envisioned: (I) the product **Se-3** forms via nucleophilic substitution (S_N2) due to the strong nucleophilicity of the selenolate or (II) a back proton transfer (PT_B) occurs with a barrier corresponding to the energy difference between **Se-TS(2, 2$_{CS}$)** and **Se-2$_{CS}$**, leading to **Se-2**. The barriers for the back-proton transfer and the nucleophilic substitution are comparable in both the model systems. However, from a thermodynamic and kinetic point of view, the higher exergonicity of the S_N2 and the smaller barrier compared to the back proton transfer (PT_B) definitively favors the formation of the selenenic acid (-1.49 kcal mol^{-1} of **Se-2** vs -57.89 kcal mol^{-1} of **Se-3**).

We estimated the energetics for the S-based model system using the geometry of **Se-1** and replacing the Se nucleus with S; then, the chalcogen-carbon distance was scaled using the covalent S/Se radii ratio. The results are shown in Table 6.2. This strategy helped also to elucidate the role of the chalcogen atom in the whole peroxide reduction process.

Table 6.2. Energetics of forward proton transfer (PT_F), back proton transfer (PT_B) and nucleophilic substitution (S_N2). ΔG is in kcal mol^{-1} and all values are relative to the initial state X-1. Level of theory: SMD-B3LYP-D3(BJ)/6-311+G(d,p), cc-pVTZ// B3LYP-D3(BJ)/6-311G(d,p), cc-pVTZ.

	X=S	X=Se	X=S†
	ΔG_{solv}	ΔG_{solv}	ΔG_{solv}
X-1	Stable	0.00	0.00
X-TS(1, 2)	-	0.32	1.85
X-2	-	-1.49	0.00
X-TS(2, 2_{CS})	-	28.33	35.78
X-2_{CS}	Not stable	27.97	33.83
X-TS(2_{CS}, 3)	-	30.80	35.10
X-3	-	-57.89	-49.25
$\Delta G^{\ddagger}$ (PT_F)	-	29.82	35.78
$\Delta G^{\ddagger}$ (PT_B)	-	0.36	1.95
$\Delta G^{\ddagger}$ (S_N2)	-	2.83	1.27

† These data refer to an S-based model system built using the geometry of Se-1 with sulfur-carbon bond distances scaled using the covalent S/Se radii ratio.

From the data of Table 6.2, the nice agreement with the tendency found in GPx models emerges, i.e. the energetics in presence of selenium is more favorable, because the barrier associated to the forward proton transfer is smaller (29.82 vs 35.78 kcal mol^{-1}) and the zwitterionic **X-2$_{CS}$** is less destabilized with respect to the neutral precursor **X-2** (29.46 vs 33.83 kcal mol^{-1}). Since in both cases the barrier for the back-proton transfer and the S_N2 are comparable, the mechanisms are controlled by the thermodynamics.

Keeping in mind that the S-based model system (Table 6.2) has a fictitious geometry that does not correspond to the real arrangement in the catalytic pocket of the Cys-GPx, we have to justify why our small bioinspired model is not working in presence of sulfur, since the Cys-GPx is able to reduce hydroperoxides, although less efficiently than the selenoenzyme. In the hypothesis that in the former case the activity is

largely promoted by the enzymatic environment, we have added two formaldehyde molecules to simulate the carboxylic group of the conserved Gln86 and the CO moiety of the peptide bond between the conserved Asn137 and Phe138 (also conserved) (Figure 6.3), which, after inspection of the Cys-GPx structure, interact with H_2O_2 as well as with Trp136 via hydrogen bonding; these H-bonds are highlighted in Figure 6.3.

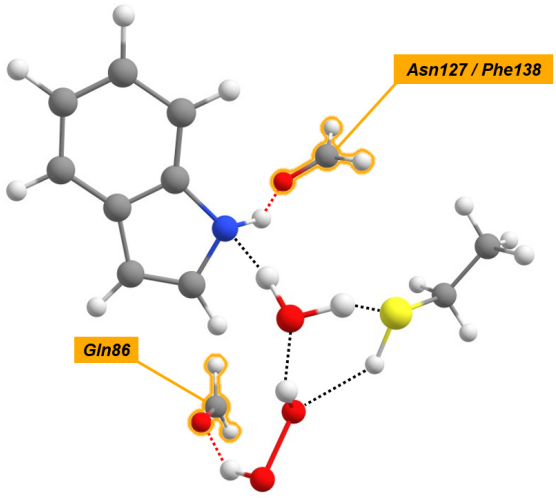

Figure 6.3. S-1 with the two formaldehyde molecules (indicated by orange labels referring to the GPx residues they are mimicking), which are mandatory to observe the reduction of H_2O_2 in our bioinspired model system.

In this enlarged system, **S-2** does not form and the formation of the zwitterionic structure is energetically easier compared to the case reported in Table 6.2 using the model built from **Se-1**. In fact, the barrier for the proton transfer is lower, i.e. 30.04 vs 35.78 kcal mol^{-1} and **S-2**$_{CS}$ is significantly less destabilized, i.e. 21.15 vs 33.83 kcal mol^{-1}. Importantly, the barrier associated to the back-proton transfer is much lower than that of S_N2, although the process is certainly driven by thermodynamics and **S-3** can form.

Table 6.3. Energetics of forward proton transfer (PT_F), back proton transfer (PT_B) and nucleophilic substitution (S_N2) for the S-based model system with the inclusion of two formaldehyde molecules. ΔG is in kcal mol^{-1} and all values are relative to the initial state X-1. Level of theory: SMD-B3LYP-D3(BJ)/6-311+G(d,p), cc-pVTZ// B3LYP-D3(BJ)/6-311G(d,p), cc-pVTZ.

	X=S	Cys-GPx	Sec-GPx
	ΔG_{solv}	ΔG_{solv}†	ΔG_{solv}†
X-1	0.00	0.00	0.00
X-TS(1, 2_{CS})	30.04	27.10	21.60
X-2_{CS}	21.15	18.30	11.40
X-TS(2_{CS}, 3)	38.91	-	-
X-3	-50.73	-48.90	-68.40
$\Delta G^{\ddagger}$ (PT_F)	30.04	27.10	21.60
$\Delta G^{\ddagger}$ (PT_B)	8.89	8.80	10.20
$\Delta G^{\ddagger}$ (S_N2)	17.76	-	-

† Taken from Ref. [182].

From the sets of calculations presented so far, we can conclude that GPx works efficiently thanks to an efficient hydrogen bonding network involving water, the close residues and the hydroperoxide itself. This is not peculiar of GPx, but holds true also in other families of enzymes with peroxidatic cysteines /selenocysteines, in which the same mechanistic path has been very recently assessed ([188], Chapter 7). The interatomic distances and the mutual orientation in this hydrogen bonding network is fundamental for the reactivity, which is affected by even slight modifications. For example, we analyzed the effect of removing the substrate, by replacing H_2O_2 with a water molecule. The **X-2_{CS}** intermediate for the S-based model system was not located on the PES, and therefore a proton transfer could not be observed. Again, for this system the geometry of **Se-1** was used (replacing Se with S atom and scaling the C-S distances using the S/Se covalent radii ratio) and the data are reported in Table 6.4. The barrier leading to **X-2_{CS}** is approximatively 8 kcal mol^{-1} higher and the zwitterionic product is less

stable by a similar amount of energy when sulfur is present rather than selenium. In addition, the barrier leading to **Se-2$_{CS}$** is approximatively 1.3 kcal mol^{-1} lower (28.57 vs 29.82 kcal mol^{-1}) in this water-water bridged system when compared to the peroxide-water bridged system (Table 6.2). This is likely to be ascribed to the shorter bridge, which is also slightly less efficient in stabilizing the zwitterionic product (28.57 vs 27.97 kcal mol^{-1}). The latter effect is attributable to an additional stabilization due to the two peroxidic hydrogens both pointing towards chalcogenolate. It is also possible to deduce that in the peculiar topology of the catalytic pocket favors an optimal length exists for the bridge linking the donor and the acceptor moieties in order to lower the proton transfer barriers.

Table 6.4. Energetics of forward proton transfer (PT_F) mediated by two H_2O molecules. ΔG is in kcal mol^{-1} and all values are relative to the initial state X-1. Level of theory: SMD-B3LYP-D3(BJ)/6-311+G(d,p), cc-pVTZ// B3LYP-D3(BJ)/6-311G(d,p), cc-pVTZ.

	X=S	X=S†	X=Se
	ΔG_{solv}	ΔG_{solv}	ΔG_{solv}
X-1	Stable	0.00	0.00
X-TS(1, 2$_{CS}$)	-	36.17	28.57
X-2$_{CS}$	Not Stable	34.79	27.22
$\Delta G^{\ddagger}$ (PT_F)	-	36.17	28.57
$\Delta G^{\ddagger}$ (PT_B)	-	1.38	1.34

† These data refer to an S-based model system built using the geometry of Se-1 with sulfur-carbon bond distances scaled using the covalent S/Se radii ratio.

Based on the results illustrated so far, our model systems faithfully reproduce the mechanistic and energy trends observed for Cys-GPx and Sec-GPx. Particularly, for the less efficient S-based system, the close residues seem even more important for the reactivity. Finally, the

deprotonation of Cys/Sec, which is a long-debated topic, is regulated by a precise hydrogen bonding network, in which the peroxide itself is involved and plays a crucial role, especially in **S-1**.

In order to better understand and precisely locate the reasons for the different role of the two chalcogens, an in-depth analysis has been carried out on a minimal model system composed by an acceptor moiety (dimethylamine, DMA) and a donor one (methanethiol/methaneselenol) bridged by a single water molecule via two hydrogen bonds (Table 6.4). The two systems have been fully optimized in order to reduce, as much as possible, any strain contribution to the energetics. The calculated barriers for the forward proton-transfer, shown in Table 6.4, are consistent with the values previously discussed for the GPx-like systems and decrease when going from sulfur to the heavier chalcogen. The stabilization of the zwitterionic products also increases. The Se-based system is the most energetically and kinetically favored system for proton transfer.

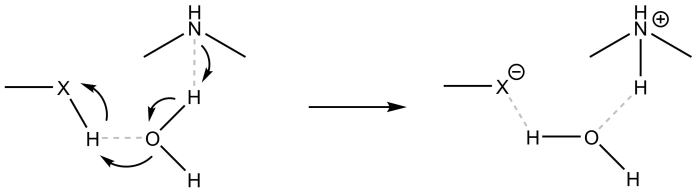

X_{min}-1 X_{min}-2_{CS}

Figure 6.4. Reactants (X_{min}-1) and products (X_{min}-2_{CS}) for the minimal system. The donor moiety CH_3XH can be methanethiol (X=S) or methaneselenol (X=Se).

Table 6.5. Energetics of the proton transfer mediated by a H_2O molecule in the model system of Figure 6.4. ΔG is in kcal mol^{-1} and all values are relative to the initial state X_{min}-1. Level of theory: SMD-B3LYP-D3(BJ)/6-311+G(d,p), cc-pVTZ// B3LYP-D3(BJ)/6-311G(d,p), cc-pVTZ.

	X=S ΔG_{solv}	X=Se ΔG_{solv}
X_{min}-1	0.00	0.00
X_{min}-TS(1, 2_{CS})	9.15	5.36
X_{min}-2_{CS}	7.73	2.03
$\Delta G^{\ddagger}$ (PT_F)	9.15	5.36
$\Delta G^{\ddagger}$ (PT_B)	1.42	3.34

We are able to recognize two relatively strong (in the non-covalent panorama) attractive interactions: the H···NH and the XH···O bonds. The nature of these barriers must be definitively investigated in the most crucial moiety, i.e. the donor molecule, and, for this reason, the ASA/EDA analysis (Table 6.6) has been carried out for the heterolytic dissociation of hydrogen from the CH_3XH molecule.

Table 6.6. ASA/EDA for the three heterolytic dissociations of H from CH_3XH (X = S, Se). ΔE is in kcal mol^{-1}. Level of theory: B3LYP-D3(BJ)/TZVP.

X	ΔE	ΔE_{strain}	ΔE_{int}	ΔV_{elstat}	ΔE_{oi}	ΔE_{Pauli}	ΔE_{disp}
S	-363.94	0.85	-364.79	-157.07	-207.05	0.00	-0.67
Se	-354.29	0.61	-354.90	-149.97	-204.21	0.00	-0.73

The chalcogen-H bond formation is mainly due to a very stabilizing interaction contribution in which only the electrostatic part is found to vary between the three different chalcogens. Orbital interaction, Pauli repulsion, dispersion forces and strain effects revealed to be of very limited importance in the X-H bond formation/disruption. ΔV_{elstat} is less stabilizing when going down from methanethiol to methaneselenol. This

confirms the more polar-covalent nature of the bond for the former. Selenols are somewhat stronger acids than the corresponding thiols because the Se-H bond is weaker than the S-H bond and because the bigger selenium atom better disperses the resulting negative charge as compared to sulfur due to its higher polarizability (Figure 6.5). For the same reason, tellurols are even stronger acids than selenols. At the same time, the hydrogen bonding of TeH and SeH is much weaker than SH hydrogen bonding. This property is also experimentally supported including oxygen and observing that thiols are more volatile and have lower boiling points than the corresponding alcohols.

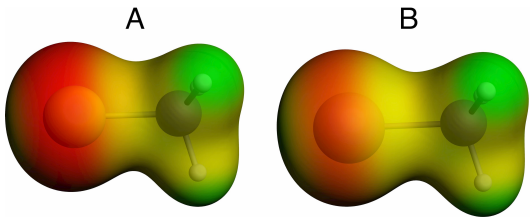

Figure 6.5. Electrostatic potential surfaces for CH3S$^-$ (A) and CH3Se$^-$ (B). Level of theory: B3LYP-D3(BJ)/TZVP. The negative charge is more evenly distributed in the selenolate showing its higher polarizability when compared to the thiolate.

As a consequence, the XH bond becomes weaker from S to Se and the heavier chalcogen is more prone to shuttle the hydrogen to the water molecule. Conversely, the stabilization of the deprotonated product increases from S to Se and it is due to the higher polarizability of the heavier chalcogen.

6.4 Conclusions

In this chapter, we have analyzed the two-step mechanism of H_2O_2 reduction promoted by the so-called peroxidatic cysteines and selenocysteines in proteins using a model molecular system based on GPx structure. The motivation was (i) to demonstrate that the deprotonation of the catalytic site, which occurs via proton shuttling to a close conserved residue, is so efficient in enhancing the nucleophilic

character of the chalcogen that the subsequent S_N2 attack to the peroxide O-O bond is almost barrierless; (ii) to pinpoint the role of the catalytic pocket in enhancing the reactivity of Cys and Sec, facilitating the proton shuttling that leads to the formation of the chalcogenolates via a network of hydrogen bonding; (iii) to assess that the advantageous presence of selenium rather than sulfur in the enzymes is first of all rooted in the different chemistry of these two chalcogens, particularly in acidity and polarizability properties. We can draw these conclusions: (i) Cys and Sec can donate their proton to a suitable proximate acceptor moiety, converting into strongly nucleophilic anions. In order to have a fast peroxide reduction, this is not enough. In fact, the S_N2 step is facilitated also by the transfer of the same proton to the peroxide, promoting the cleavage of the O-O bond and releasing water as leaving group. (ii) The close conserved residues in the enzymes play a fundamental role: one of them is the proton acceptor, while the others provide a suitable frame in which a hydrogen bonding network forms along which proton transfer occurs. The inadequacy of this pathway leads to inactivity or less efficiency of the system, as revealed by the S-based model which is not working if not enough residues are included or the water-only bridged system, which is likely to lead to less stable zwitterionic species when compared to the peroxide-water bridged one. (iii) It is well known that selenols are stronger acids than thiols and that bonds involving Se are more polarizable than ones involving S. But through ASA/EDA we have demonstrated that these purely chemical properties influence the onset of the weak interactions, which, as above commented, are the key elements for the observed peroxidatic activity.

7 The common principle of peroxidatic cysteine and selenocysteine residues

Adapted from

M. Dalla Tiezza, F. M. Bickelhaupt, L. Flohé, M. Maiorino, F. Ursini, L. Orian

Redox Biology 2020, 34, 101540

7.1 Introduction

Already centuries ago, when Thénard discovered hydrogen peroxide (H_2O_2) [194], it became obvious that this compound was readily decomposed by organic material. Over the years, the observation was reported many times [195–197] and finally culminated in the discovery of catalase as a widely distributed enzyme that catalyzed the

destruction of H_2O_2 [198]. Starting in the 1920s, the iron and heme content of catalase and peroxidases was established by different groups (reviewed in [199,200]), and for long, peroxidase activities were considered to strictly depend on heme as prosthetic group. Up to the mid-1970s this dogma is still reflected in monographs on oxidoreductases or reviews on catalase or peroxidases in general [201,202], although it should have been abandoned when Mills, in 1957, described glutathione peroxidase (GPx) as a non-heme protein [179]. GPx (now GPx1) was later verified as the first mammalian selenoprotein to be discovered [203–205]. The redox-active residue in its reaction center proved to be a selenocysteine [206,207]. These findings and the later discovery of the second mammalian selenoprotein [208], phospholipid hydroperoxide glutathione peroxidase (PHGPx, now GPx4) supported the believe that the magic catalytic power of selenium could substitute for heme in the catalytic decomposition of hydroperoxides, an assumption that had to be equally refused.

When Maiorino et al. exchanged the catalytic selenocysteine of GPx4 against cysteine, the activity of this CysGPx4 enzyme was expectedly impaired [185]. However, the bimolecular rate constant for the oxidation of the enzyme by phosphocholine hydroperoxide k_{+1} was decreased by less than 3 orders of magnitude and with $5 \cdot 10^4$ $M^{-1}s^{-1}$ was still orders of magnitude higher than any rate constant for the oxidation of any low molecular weight thiol by a hydroperoxide (Table 7.1). Moreover, naturally occurring CysGPxs, e. g. the GPx of *D. melanogaster* [209], displayed rate constants that were almost competitive with those of mammalian selenoenzymes (for review see [187]). At the latest after the discovery, in the laboratories of Bruce Ames and Earl Stadtman, of the second non-heme peroxidase family [210,211], the peroxiredoxins, which only exceptionally work by selenium catalysis [212], it became clear that also sulfur can efficiently catalyze the reduction of hydroperoxides.

The first step of these peroxidatic reactions is an oxidation of their active site cysteine or selenocysteine to the corresponding sulfenic or

selenenic acid, respectively. The latter then react with thiol groups of diverse compounds such as glutathione, SH groups of other proteins, "resolving cysteine" residues of the peroxidase itself and/or redoxins to stepwise regenerate the ground state enzyme [213]. Analogous chemistry is now increasingly considered to explain the multiple modifications of cysteine residues of regulatory proteins. However, in most of the cases, the speed of the first step, *i.e.* that of the cysteine oxidation, is comparatively low ([214,215], see also Table 7.1). In many cases, their "reactive cysteines" are therefore not likely oxidized directly by H_2O_2. Instead, the oxidation equivalents are transferred to these proteins, typically *via* hetero-dimerization followed by thiol/disulfide exchange, by oxidized thiol peroxidases, which here act as H_2O_2 sensors [216]. Such indirect oxidative thiol modification has been demonstrated for the activation of the transcription factor Yap1 by yeast GPx3 in *Saccharomyces cerevisiae* [217], for the reaction of transcription factor Pap1 and the signal transducer Sty1 with the peroxiredoxin–type Tpx1 in *Schizosaccharomyces pombi* [218], of the activator protein STAT3 with PrxII in mammalian cells (HEK293T) [219], and the *S*-glutathionylation of protein kinase C and others by glutathione *S*-transferase P [220]. More recently, Stöcker et al. [221] found the overall content of oxidized protein thiols decreased in mammalian cells having the 2-Cys-Prxs knocked-out. This surprising finding indicates that the support of thiol peroxidases in cysteine oxidation is more common than hitherto anticipated.

The cysteine residues of 2-Cys-peroxiredoxins reacting fast with H_2O_2 were the first to be called "peroxidatic cysteine" residues (C_P), but this term has meanwhile been adopted to all cysteine or selenocysteine residues (U_P in this case) with unusually high reactivity towards hydroperoxides. They do not only exist within the two thiol peroxidase families. Other well documented examples are the bacterial transcription factors of the OxyR family discovered 1985 by Ames and coworkers in *Salmonella typhimurium* [116]. Also, the active site cysteine of GAPDH is often oxidized directly by H_2O_2 or peroxynitrite.

Its activity as glycolytic enzyme is thereby blocked, whereby carbohydrate metabolism is directed towards the pentose phosphate shunt, and as glutathionylated, nitrosylated or aggregated protein GAPDH adopts a broad spectrum of functions [222].

The mechanisms leading to the extreme reactivities of the cysteines (C_P) or selenocysteines (U_P) in thiol peroxidases and other proteins have only been addressed in exceptional cases. The most commonly read explanation claims surface exposure and a low pK_a of C_P or U_P, respectively, induced by neighboring basic residues. For sure, the chalcogenols in these proteins have to be dissociated to enable an efficient S_N2 attack on the hydroperoxide bond [223]. However, as is known from low molecular weight compounds with freely accessible thiols or selenols (see Table 7.1 and [224,225]), they will hardly react with H_2O_2 at rate constants exceeding $50 \cdot M^{-1}s^{-1}$, even if they are fully dissociated. Therefore, there is a common agreement that the peculiar architecture of the active site, which differs between protein families with a C_P (or U_P), accounts for their efficiency [215,222,223,226]. For the peroxiredoxins, a stabilization of the transition state has been postulated [215]. Peralta and coworkers [227] detected a relay of shuttling protons in GAPDH, and Ferrer Sueta et al. [223] and others highlighted the importance of an ideal leaving group. In a previous study [181], Orian and coworkers concluded that the unusually high efficiency of the GPx-type peroxidases is based on water-mediated proton shuttling. This leads to a zwitterionic structure, in which the O-O bond can be easily split by a concerted nucleophilic attack of the deprotonated chalcogen and an electrophilic one by a highly energized proton that is dislocated to a tryptophan nitrogen of the active site. We here try to figure out if a similar dual attack can generally account for C_P activity. To this end, we subjected the active sites of the different protein families with high C_P activity, which for convenience we call peroxidases. This way, the mechanism established for GPx family is here extended to GAPDH (1U8F), OxyR (4X6G) and an alkylhydroperoxide reductase, a peroxiredoxin (Prx; 4X0X). Although

a U_P is only common in the GPx family and only exceptionally present in the Prx family, we consider Cys as well as Sec as reactive moiety of all the protein families, to gain an idea of the impact of the catalytic chalcogen on the energetics [228–230].

Table 7.1. Selected rate constants for chalcogen oxidation near physiological pH.

Compound	Co-reactant	k_{+1} (M^{-1} s^{-1})	Ref.
GSH	H_2O_2	0.9	[224]
Cysteine	H_2O_2	2.9	[224]
Selenocysteine	H_2O_2	35.4	[231]
Protein phosphatase PTP1B	H_2O_2	9 - 20	[215,224]
Protein phosphatase Cdc25B	H_2O_2	$1.60 \cdot 10^2$	[224]
Glyceraldehydephosphate dehydrogenase	H_2O_2	$\sim 5 \cdot 10^2$	[224]
Transcription factor OxyR	H_2O_2	$\sim 5 \cdot 10^4$	[232]
Peroxiredoxins	H_2O_2	$\sim 10^4$-10^7	[224,233]
Transcription factor Ohr (Prx)	Linoleic acid hydroperoxide	$3 \cdot 10^7$	[226]
Cys-glutathione peroxidases	H_2O_2	up to $1.6 \cdot 10^6$	[187]
Glutathione peroxidase 1 (bovine)	H_2O_2	$5 \cdot 10^7$	[186]
Glutathione peroxidase 4 (porcine)	Phoshatidylcholine hydroperoxide	$1.4 \cdot 10^7$	[187]
Glutathione peroxidase 4 U→C	Phoshatidylcholine hydroperoxide	$5 \cdot 10^4$	[187]

7.2 Methods

Computational mechanistic studies were carried out employing state-of-the-art DFT methodologies as implemented in the Gaussian programs suite [132]. For technical limitations, we had to restrict our calculation to the intimate environment of the peroxidatic cysteine, i.e., to a S (Se) distance of about 7 Å. This implies that the possible impact of the more remote residues on the reaction mechanism is ignored.

All geometry optimizations were carried out with Gaussian 16 software rev. C.01 [132] The used exchange correlation functional is the three parameters hybrid GGA B3LYP [189–192] with additional dispersion corrections implemented with the D3(BJ) approximation [28,29]. The used basis set for light atoms (H, N, C, O, S) is the Pople 6-311G(d, p) [134,135], a split-valence triple-zeta set plus p and d polarization functions for hydrogen and non-hydrogen atoms, respectively. The selenium atom, instead, has been described with Dunning's cc-pVTZ basis set [234]: a correlation-consistent and polarized-valence basis set of triple ζ quality. All the optimizations were performed in the gas phase. The stationary points, minima and transition states, have been localized with a canonical vibrational analysis. The single normal mode associated with a negative force constant (and imaginary frequency) involved in the transition state has been verified to completely assure the nature of the barrier. Unless explicitly stated otherwise, all the geometry optimizations on the enzymes' catalytic pockets were carried out keeping a frozen backbone (N, C, O atoms are constrained). Only H, S, Se and the O atoms of the hydrogen peroxide and water molecules are free to move. In all cases, the minimum energy reaction path (MERP) has also been confirmed by a NEB (nudged elastic band) calculation carried out with ORCA 4.2.1 [235–237]. The calculations in condensed phase have been carried out with the Minnesota Solvation Model based on Density (SMD) developed by Truhlar et al. [138]. In order to mimic the proteic environment, a dielectric constant of 4.24

(diethyl ether) has been chosen in accordance with Ref [182,238]. Unless otherwise stated, only Gibbs free energies are presented in this chapter.

7.3 Results and discussion

In order to solve the enigma of the super-reactive cysteines in proteins, we subjected representatives of three more protein families to practically the same DFT calculations, as we had applied before for the GPx family [181]. Prerequisites for choosing the proteins were known X-ray structures and kinetics that revealed a k_{+1} for the reduction of H_2O_2 significantly higher than that of any fully dissociated low molecular mass thiol or selenol. The relevant k_{+1} values covered a wide range from comparatively low to extremely high (GAPDH: 10^2-10^4 $M^{-1}s^{-1}$; OxyR: ~ 10^5 M^{-1} s^{-1}; peroxiredoxins: 10^4-10^8 $M^{-1}s^{-1}$).

7.3.1 *Pa*OxyR (*Pseudomonas aeruginosa* Oxidative Stress Regulator)

A common structure for the peroxide sensing in bacteria is the Oxidative Stress Regulator (OxyR), which indirectly adjusts the level of H_2O_2 in the cellular environment. It is worth to mention that sensing mechanisms in different bacteria are numerous, and the relative importance of each of them is still debated. However, two major parts of the OxyR reaction have been assessed. The reactive cysteine ("C_P") is oxidized to a sulfenic acid, but unlike in the mechanism of the selenocysteine-containing GPxs, the sulfenic acid here forms an intramolecular disulfide bridge between two highly conserved cysteines. This process leads to a structural change that results in the transcription factor activity of the (oxidized) OxyR [230]. Our attention is focused on the first part (oxidation step), i.e. the H_2O_2 reduction step.

For our calculations, we selected 4 residues (Thr100, Thr129, His198 and Cys199) from the full-length *Pa*OxyR of the 4X6G crystallographic structure [230]. In order to better understand the binding site and the

orientation of the oxidizing substrate, the C_P was mutated to Asp and then the crystallized protein was exposed to H_2O_2 vapors. The entire system is tetrameric and can be further divided into two extended subunits and two contracted ones. In our initial structure, the Cys199 active site has been adapted from an Asp199 residue that was present in the *Pa*OxyR reported in Ref. [230]. In order to obtain a reliable orientaton of the Cys199, the -SH moiety was kept unfrozen during our structure optimizations. The terminations of the non-contiguous amino acid chains have been saturated with the ACE/NME capping.

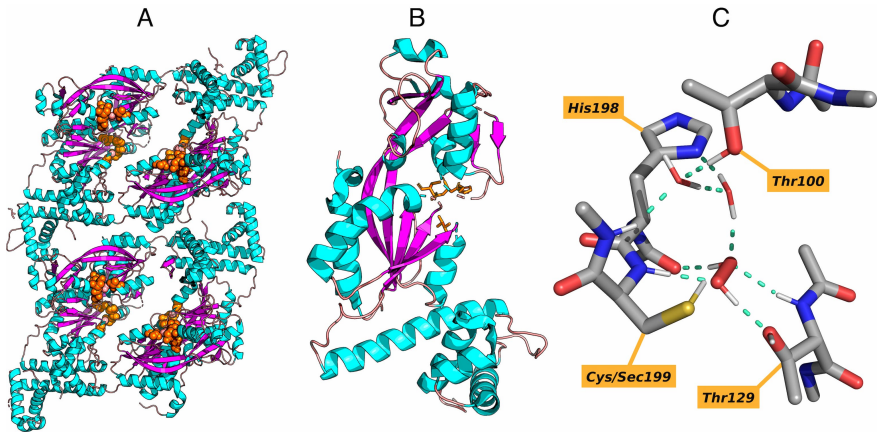

Figure 7.1. A) The full-length *Pa*OxyR: the color code highlights the secondary structure and the catalytic pocket is clearly visible in orange. B) Zoom on the B chain; selected residues are visible in orange. C) The selected framework of the active site near the H_2O_2 binding site. Asp199 has been substituted by Cys/Sec199 (sulfur/selenium atom in yellow).

The chosen residues are shown in Figure 7.1 B. Two water molecules nicely fit in the pocket in a favorable orientation to mediate a proton transfer and are also indicated. The histidine provides a good hydrogen acceptor moiety during the proton transfer while the two threonines keep the substrate and the water molecules in position. The mechanism, as it emerges from our DFT calculations, is sketched in Figure 7.2. Initially, Thr129 keeps H_2O_2 close to the thiol group via H bonding, while Thr100 and His198 are connected via a two water molecule bridges. The thiol/selenol proton shuttles to the NH group of His198

with an activation energy of 31.0/25.6 kcal mol^{-1}, respectively. In case of the Cys-enzyme, the zwitterionic form is highly destabilized and the formation of the sulfenic acid occurs via a very small activation energy, i.e. 0.6 kcal mol^{-1}. In case of the Sec-enzyme, the zwitterionic form is even less stable and the process of proton shuttling and oxidation to selenenic acid is concerted. Notably, the S_N2 attack of the thiolate/selenolate anion to H_2O_2 is facilitated since the deprotonation has enhanced the nucleophilicity of both chalcogens. Importantly, the thermodynamic driving force for the oxidation of Sec is much larger than that computed for the oxidation of Cys, suggesting that the presence of the heavier chalcogen in the catalytic pocket is thermodynamically as well as kinetically advantageous. To our knowledge, however, Sec variants of OxyR have so far not yet been discovered.

Based on X-ray structures and site-directed mutagenesis data, Pedre et al. [232] also postulate an essential role of Arg270. Indeed, Arg270 might offer an ultimate "parking lot" for the delocalized proton. However, we have not included this residue in the cluster essentially for two reasons: It is not close to the reactive thiol and so we can exclude a direct interaction. In addition, it interacts via N···O in *C. glutamicum* OxyR (here Arg278) and in *P. aeruginosa* OxyR with Thr100 (Thr107 in the former structure). We therefore assume that it primarily has a structural role, but with high impact on the proton transfer mechanism. In fact, if Thr100 is free to adopt a different orientation, the two-water bridges cannot form and so the thiol proton cannot be shuttled to His to initiate the peroxidatic process (Table 7.2).

Table 7.2. Forward proton transfer (PT_F), back proton transfer (PT_B) and nucleophilic substitution (S_N2) Gibbs free energies for *Pa*OxyR. ΔG_{solv} is in kcal mol^{-1}.

	Cys ΔG_{solv}	Sec ΔG_{solv}
1	0.00	0.00
TS(1, 2_{CS})	30.95	25.55
2_{CS}	24.81	Direct to products
TS(2_{CS}, 3)	25.44	
3	-46.36	-54.60
$\Delta G^{\ddagger}$ (PT_F)	30.95	25.55
$\Delta G^{\ddagger}$ (PT_B)	6.14	-
$\Delta G^{\ddagger}$ (S_N2)	0.63	0.00

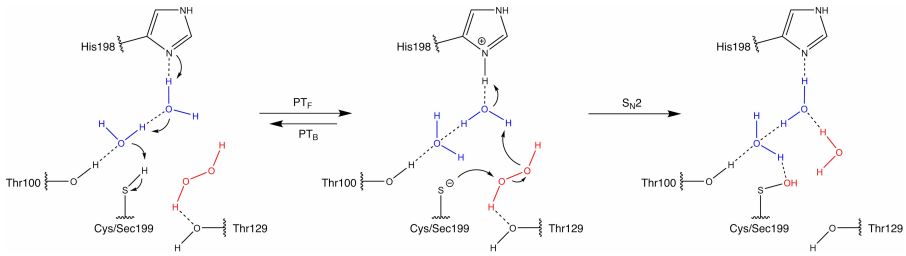

Figure 7.2. Mechanism of H_2O_2 reduction in *Pa*OxyR catalytic pocket.

7.3.2 *Hs*GAPDH (*Human* Glyceraldehyde 3-phosphate dehydrogenase)

The glycolytic glyceraldehyde 3-phosphate dehydrogenase (*Hs*GAPDH) is a tetramer formed by four chains (O, P, Q, and R) and every subunit contains a cysteine (Cys152) that is essential for both, the aldehyde dehydrogenase activity and the fast reduction of H_2O_2. The chosen structure is the human placental *Hs*GAPDH (PDBid: 1U8F). Like in *Pa*OxyR, the second essential amino acid is the His179, which works as hydrogen acceptor during the proton transfer step. Interestingly no water molecules are required during the reduction of the H_2O_2 substrate

and this is mainly due to the presence of several hydroxyl groups, those of Thr153, Tyr314 and Thr177, which allow H-bond formation between these residues and the substrate. The selected residues for modeling the catalytic pocket are Cys152, His179, Thr153, Cys156, Tyr314, Thr177 and Val178 from the chain P. The reaction mechanism is sketched in Figure 7.4.

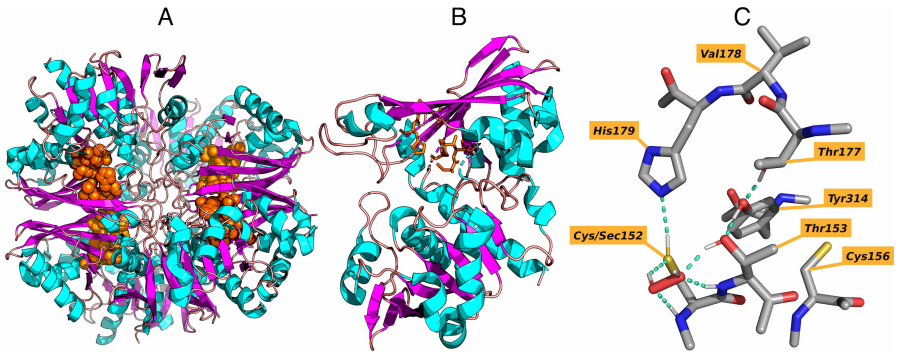

Figure 7.3. A) The *Hs*GAPDH enzyme: the color code highlights the different secondary structure and the catalytic pocket are clearly visible in orange. B) Only the P chain is shown and the active residues are depicted with licorice style in orange. C) The selected framework of the active site nearby the H_2O_2 binding site.

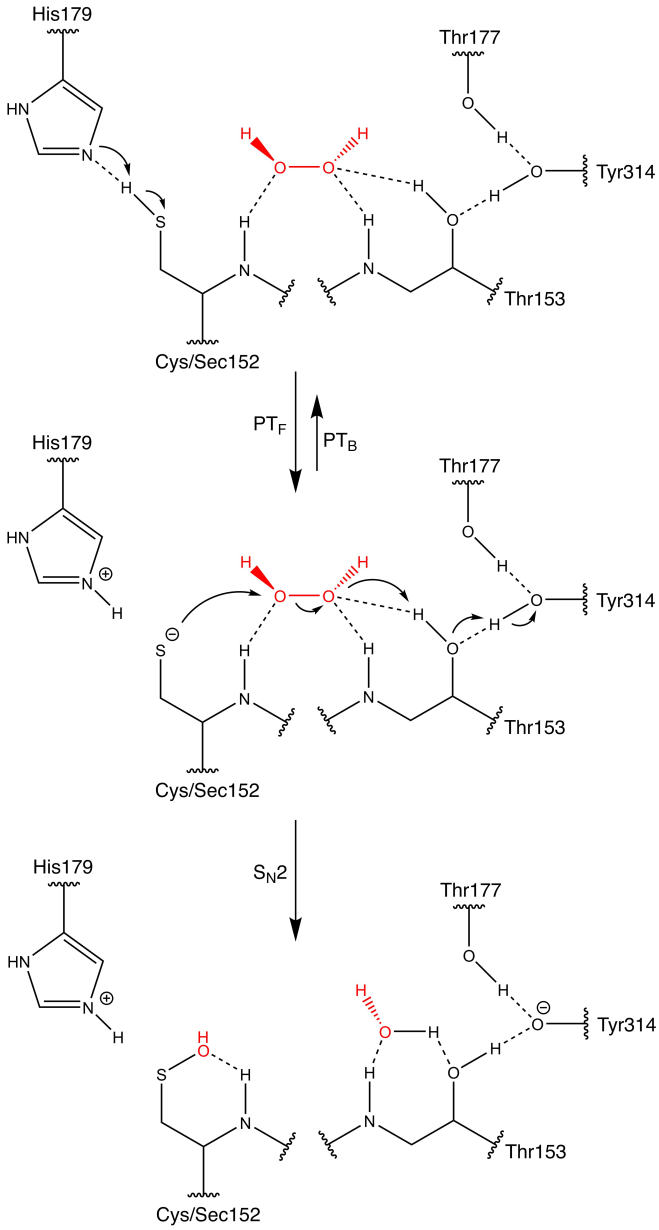

Figure 7.4. Mechanism of H_2O_2 reduction in *Hs*GAPDH catalytic pocket.

The peroxide oxygens of the H_2O_2 molecule is squeezed via hydrogen bonds of the NH groups and an OH group of Thr153 and Cys/Sec152. His179 and Cys/Sec152 are in a suitable position to favor the proton shuttling. Once the thiolate/selenolate is formed, the S_N2 attack on the

peroxide occurs, which is readily split with formation of a sulfenic (selenenic) acid. Protonation of the remaining OH by Thr153 facilitates the cleavage of water from the substrate. The latter step does not appear particularly likely, but here is facilitated by the extended hydrogen bond network, between Thr153, Thr177, Tyr314 and possibly more remote residues, which allow re-protonation of Thr153. The mechanism here calculated is practically identical to that proposed by Peralta et al., which was essentially based on molecular dynamics and bioinformatic tools [222,227].

The reaction energies are summarized in Table 7.3, and also in this case it emerges that the peroxide reduction is easier in presence of selenium rather than sulfur. Particularly, the barrier of the first step (proton transfer) is almost 6 kcal mol^{-1} smaller compared to that computed for the Cys-*Hs*GAPDH. The activation energy for the nucleophilic substitution is comparable between the two enzymes. Overall, however, the process is thermodynamically as well as kinetically more favored for the Sec-*Hs*GAPDH.

Table 7.3. Forward proton transfer (PT_F), back proton transfer (PT_B) and nucleophilic substitution (S_N2) Gibbs free energies for *Hs*GAPDH. ΔG_{solv} is in kcal mol^{-1}.

	Cys ΔG_{solv}	Sec ΔG_{solv}
1	0.00	0.00
TS(1, 2_{CS})	15.99	10.42
2_{CS}	-4.45	-5.08
TS(2_{CS}, 3)	8.99	3.79
3	-47.69	-51.22
$\Delta G^{\ddagger}$ (PT_F)	15.99	10.42
$\Delta G^{\ddagger}$ (PT_B)	20.44	15.49
$\Delta G^{\ddagger}$ (S_N2)	13.44	8.86

7.3.3 *Mt*AhpE (*Mycobacterium tuberculosis* alkyl hydroperoxide reductase E)

Last, we considered an example of a peroxiredoxin subgroup, the *Mt*AhpE, in which very fast catalytic reduction of H_2O_2 and other hydroperoxides occurs [239]. The selected crystallographic structure (PDBid: 4X0X) contains four chains made by two identical subgroups: A, B and C, D (Figure 7.5). The highly conserved amino acids are Cys45, Thr42, Glu48, Arg116, and Pro135. The essentiality of the residues homologous to Cys45 and Arg116 has been documented for many peroxiredoxins. Chain B has been chosen because the Arg116 orientation better resemble the conformation of the same conserved AA in other Prxs [240]. The Thr residue, which in natural peroxidoxins is sometimes exchange by serine, could be exchanged by serine in a peroxiredoxin of *Leishmania infantum* (here Thr 49), but not by any residue that lacked an OH function [241], In order to reduce the number of atoms involved and increase the chances for weak stabilizing interactions, Pro135 and Glu48 have been excluded because of the distance from the Cys45 and the residues Pro38 and Leu39 have been retained in the cluster because of their proximity to the reactive center. In this specific case, the used capping technique is hybrid: for terminations close to the center of the active region canonical ACE/NME residues have been used; for terminations pointing outward, a methyl substituent has been used to save computational time. The position of Arg116 is very close to Cys/Sec45: this is particularly useful because, once the chalcogenolate forms (after the proton transfer step), the positively charged Arg116 stabilizes the accumulation of electron density on the sulfur/selenium atom.

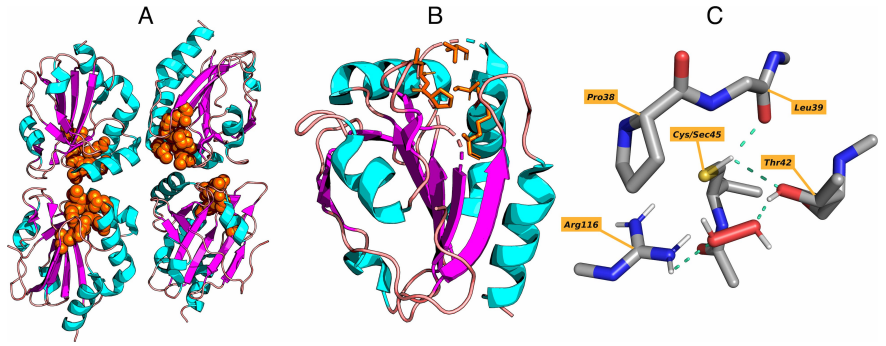

Figure 7.5. A) The *Mt*AhpE enzyme: the color code highlights the different secondary structure. The AAs involved in the active area are shown in orange. B) The catalytic pocket of a monomer (chain B, in orange). C) The five conserved AAs of the selected catalytic pocket.

The *Mt*AhpE mechanism, sketched in Figure 7.6, occurs in two steps. In the first one, a proton transfer between the donor Cys/Sec45 and the acceptor Thr42 takes place. The protonated threonine is not a commonly stable intermediate but, in this case, a stable charge separated structure is possible thanks to a synergic stabilization between the newly formed chalcogenolate and the positively charged -OH_2^+ moiety. A further stabilizing factor derives directly from a hydrogen bond established between the hydrogen of the charged oxygen of the threonine and the carbonyl moiety in the peptide bond of the same amino acid. H_2O_2 is bound between Thr42 and Arg116 via efficient hydrogen bonding [242,243]. The thiol/selenol is facing Thr42 in favorable position for the proton shuttling. In this first step, the barrier and the released energy values are advantageous for the Sec- enzyme by 6 kcal mol^{-1}. The barrier for the backward proton transfer is comparable between the Cys and the Sec enzyme. Unexpectedly, the S_N2 step is almost barrierless (0.1 kcal mol^{-1}) for the Cys enzyme and requires a really small activation energy for the Sec variant (2.5 kcal mol^{-1}). However, the released energy is almost 10 kcal mol^{-1} larger in the latter case.

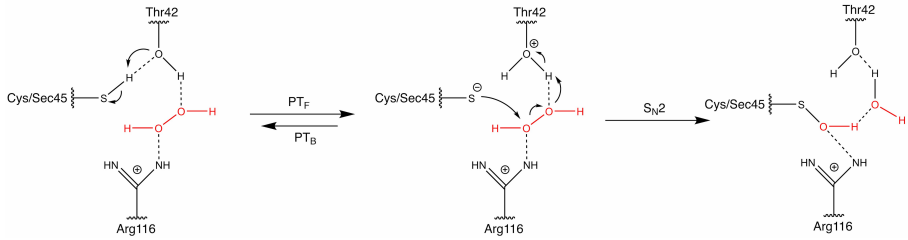

Figure 7.6. Mechanism of H_2O_2 reduction in *Mt*AhpE catalytic pocket.

The driving force pushing towards the oxidation of the chalcogenolate is to be ascribed to two key factors: the first one involves the reaction kinetics where the competitive back proton transfer is less favored than the nucleophilic substitution with the formation of the sulfenic/selenenic acid. Then, from a thermodynamic perspective, a strong stabilization in both the cases is possible only if the reaction proceeds to the oxidation of the chalcogenolate and the formation of one water molecule. The average exergonicity of the whole process is about 70 kcal mol^{-1}.

Table 7.4. Forward proton transfer (PT_F), back proton transfer (PT_B) and nucleophilic substitution (S_N2) Gibbs free energies for *Mt*AhpE. ΔG_{solv} is in kcal mol^{-1}.

	Cys ΔG_{solv}	Sec ΔG_{solv}
1	0.00	0.00
TS(1, 2_{CS})	24.28	18.27
2_{CS}	14.72	9.18
TS(2_{CS}, 3)	14.82	11.66
3	-64.18	-72.32
$\Delta G^{\ddagger}$ (PT_F)	24.28	18.27
$\Delta G^{\ddagger}$ (PT_B)	9.56	9.09
$\Delta G^{\ddagger}$ (S_N2)	0.10	2.48

The mechanism, as outlined above, differs from that described by Hall et al. [244]. This investigation of human Prx5, which also considered X-

ray structures of many Prxs with H_2O_2 mimics, postulate an S_N2 reaction between the thiolate of C_P and H_2O_2 as the key peroxidatic step, which complies with our results. It further stresses the stabilization of the C_P thiolate by the essential Arg, which also is in line with our results. However, it leaves open the problem, how the thiolate of C_P is generated. The neighborhood of Arg is discussed, but it is not easily understood, how the guanidinium function of an Arg with a pK_a around 12 should serve as a proton acceptor. Nor is it comprehensive that the very same Arg enhances the nucleophilicity of the C_P sulfur and the electrophilicity of the oxygen of H_2O_2 to be attacked. Also, Zeida et al., although they applied a similar approach to the same enzyme [245] ended up with a different mechanism, which is similar to the mechanistic proposal of Hall et al. [244]. Here the essential role of Thr42 was largely ignored. At best a hydrogen bond of the threonine OH to the reacting sulfur is considered, which must be rated as unlikely, since O-H···S bonds are not readily formed. The reason for the different outcome of the calculations results from different starting conditions. In fact, the essential Arg shows relatively high RMSD value [246], which indicates the possibility of different orientations of this residue. When we started with the same Arg orientation., we could in fact reproduce the results of Zeida et al.. When taking the alternate Arg orientation, the role of Thr42 as proton acceptor, as shown in Figure 7.6, was clearly disclosed.

7.4 Conclusions

For sure, the peroxidatic cysteine (C_P) or selenocysteine (U_P) has to be deprotonated to allow an efficient S_N2 reaction with the peroxide bond yielding a sulfenic or selenenic acid, and for sure, such electrophilic attack does not suffice to explain the rate constants of C_Ps or U_Ps. A second attack is required to cleave the peroxide bond efficiently.

As shown previously for the GPx family, the second attack is an electrophilic one on the second oxygen atom of the peroxide bond. Not

only in the GPx family, but also in the three protein families investigated herein, the electrophilic attack is achieved by a shuttling proton, which combines with the OH or OR to yield water or an alcohol, respectively, as ideal leaving group.

The labile proton stems from residues of the active site and usually reaches the peroxide bond by long-range proton shuttling via water molecules (GPx), residues of the active pocket (GAPDH, Prx) or both (OxyR).

The DFT calculations reveal that the chalcogenol proton is transferred to residues of the active site, where they form more or less stable bonds (ring nitrogen of Trp136 in human cytosolic GPx4, His nitrogen in OxyR and GAPDH, oxygen of Thr in Prx). The proton transfer may involve more remote residues that are not considered in our calculations. In any case, it creates a zwitterionic nature of the active site.

The complex between the zwitterionic form of the proteins and the hydroperoxide reacts without any or with a very low activation energy. The activation energy appears to be lowest, if the delocalized proton is bound in an unstable, i.e. highly energized way (bound to Trp or Thr).

If the chalcogen is selenium instead of sulfur as in many GPxs and sometimes in Prxs, the overall hydroperoxide reduction is thermodynamically and kinetically favored.

It remains to be demonstrated whether the emerging reaction scheme holds true for other protein families equipped with super-reactive chalcogenols. Interestingly, proton shuttling has also been implicated in the catalytic mechanism of horse radish peroxidase [247,248], suggesting that this principle may generally be helpful in splitting a peroxide bond, i.e. also in heme peroxidases.

8 Conclusions

Summary

As we thoroughly described in the chapters of this thesis, the density functional theory has been used to study selected systems of chemical and biochemical relevance. Using in silico methodologies, we were able to rationalize the mechanistic details and performances of inorganic catalysts as well as of enzymes and bioinspired molecules. In all these different examples, it emerges that elementary redox reactions play a role of paramount importance.

In Chapters 3 and 4, we have focused our attention on small-scale systems aimed at pure inorganic catalysis for the synthesis of benzene, pyridine and its derivatives via alkyne [2+2+2] cycloadditions. We were also able to see how this process, which is highly disfavored from the entropic point of view, can become viable with the help of group 9 metal half-sandwich catalysts. Firstly, we looked for the reason justifying the highest efficiency of cobalt-based catalysts through molecular orbital inspection and fragment-based energy decomposition analysis. Subsequently, we analyzed and classified all the screened catalysts,

ordering their efficiencies by the theoretical calculation of turnover frequency (TOF). This was used for a later structural study intended to keep track of the metal slippage in order to quantify it, in a new and rigorous way, through the introduction of a novel descriptor: the LISP. This was conceived to establish a meaningful and general structure-reactivity relationship. The combination of these two ingredients, i.e. TOF and LISP, and a cross comparison with literature data allowed us to reach our ambitious goal, drawing essential elements for a rational design of the studied catalysts.

The fifth chapter is intended to introduce the problem of oxidative stress and how this is tackled by small organic molecules acting as antioxidants, particularly as quenchers of harmful free radicals. Also, in this case, a deep characterization of the systems, i.e. phenothiazine, phenoselenazine and phenotellurazine, has turned out to be necessary to subsequently define the global capabilities of these radical scavengers. In this case, the catalytic center is a chalcogen atom, which makes the molecules mimic of the glutathione peroxidase. In fact, in principle, the chalcogen can reduce the peroxyl radicals toward which the scavenger is inactive. The path for the reduction of the chalcogen has not been explicitly investigated but is a process that quickly occurs in the presence of thiolates. The QM-ORSA protocol has been the central fulcrum for the estimation of antioxidant capacity and comparison to other well-known antioxidants. No significant differences due to the presence of S, Se and Te were found, but the role of the chalcogen in catalyzed processes is a breakthrough in Chapters 6 and 7.

In fact, in the last part of the thesis, entirely devoted to enzymatic catalysis, the oxidation of the enzymes GPx, OxyR, GAPDH and MtAhpE, which belongs to the Prx family is discussed; all these proteins have in common the presence of a peroxydatic (seleno)cysteine in the active site. The great advantage of selenium over sulfur in GPx is indisputable but one question arises spontaneously: is this advantage limited only to GPx? In Chapter 6, we have proposed a solid answer to

this question; in fact, we have observed how what we saw in GPx can be extended to the other three studied enzymes. This significant result shows us once again how the particular conformation of the catalytic pocket of GPx is not the only key to its activity but is part, together with the selenocysteine and an acceptor moiety (that can vary from enzyme to enzyme), of a set of essential features that are present also in other enzymes all possessing a peroxidatic (seleno)cysteine. Considering the importance of GPx, and supported by the collaboration of Prof. Leopold Flohé, who first discovered the presence of selenium in GPx, the whole Chapter 7 is dedicated to a model molecular system of GPx that can be easily analyzed by full QM calculations to explain in detail the two-step oxidation mechanism described by us as a general mechanism for the above listed enzymes.

It's my personal belief that the difficulty of describing a complex system lies mainly in identifying and collecting all its, apparently trivial, details. Most of the time, it is all in these small details that, coming together, form a much, much larger whole.

This brings us closer to the conclusion of this dissertation: we have seen how nowadays simulations, not only concerning chemistry, can be priceless for their predictive contribution. From the birth of the Turing machine through the modern High Performance Computing facilities, the role of what we know today as computers has never changed: answer our questions. Since the machine does not have any interpretative capabilities, everything lies in how the question is raised. We have in our hands a tool designed to simplify and accelerate model analysis and processes optimization and, like any other instrument, it must be used wisely without ever overestimating its capabilities. The man-machine equilibrium is at the basis of effective use of this now inestimable resource that can be used by everyone and which can make life easier in many contexts.

We have reached the very end and one last thing is left: a thank you is due for your patience and for coming all the way here.

I hope that the covered themes have been resolved to your satisfaction.

Ringraziamenti

Molte persone mi hanno accompagnato durante la stesura di questa tesi e ognuno mi ha supportato a suo modo: chi mi ha attivamente aiutato e chi invece mi è semplicemente stato vicino, spronandomi ogni giorno. Indipendentemente da questo, tutti hanno avuto un loro ruolo chiave e per questo vorrei sinceramente ringraziarli. Mi rendo conto che il compito è assai arduo ma proverò a fare del mio meglio per includere tutti quanti.

Un grazie del tutto speciale va alla mia famiglia, a mio Papà Renato, a mia sorella Roberta e alle zie/zii che mi hanno incoraggiato e sostenuto moralmente di giorno in giorno: senza di loro non sarei potuto andare molto distante e non sarei mai arrivato dove sono ora. Grazie per tutto!

Un grazie sincero alla Prof. Laura Orian che mi segue oramai da 5 anni (questa è già la terza tesi che revisiona!) con costante dedizione e professionalità. Sia durante la laurea che durante il dottorato, mi ha insegnato ed aiutato a risolvere problemi di diversa natura senza mai perdere la voglia di fare e lo spirito. Tutti i lavori contenuti in questa tesi non avrebbero mai visto la luce se non fosse stato per la sua importante guida.

Un grande ringraziamento va anche al Prof. Matthias Bickelhaupt e al Dr. Trevor Hamlin per il costante supporto durante il mio soggiorno ad Amsterdam di 6 mesi alla Vrije Universiteit. Mi hanno accolto nel loro gruppo di ricerca cercando di aiutarmi sempre con preziosi consigli, facendomi prendere parte attivamente a diverse attività già dal primo giorno che sono arrivato. Grazie a tutti gli amici e colleghi olandesi per l'aiuto e il tempo dedicatomi dove mi è stato insegnato a vedere ed analizzare certi dettagli con una nuova ed innovativa prospettiva.

Un "Danke vielmals!" va indiscutibilmente al Prof. Leopold Flohé per aver letto e supervisionato parte dei miei lavori a distanza ma sempre con estrema dedizione e competenza.

Un immenso grazie va agli amici di sala calcolo: Francesco (Fracni), Marco (grande), Alessandro, Enrico, Maurizio, Pierpaolo, Andrea (Pischio), Cecilia, Jonathan (JFK), Federico, Matteo, Pietro e Andrea che mi conoscono come Marcolino e che han saputo rallegrare l'ambiente ogni giorno e dai quali ho imparato un'infinità di cose. Senza questi, dubito sarebbe potuta esistere la Theoretical Pizza ed i numerosi aperitivi che allietavano la fine della giornata lavorativa!

Non potrei mai dimenticare gli amici di montagna e di arrampicate! Grazie Alice, Davide (membri fondatori dei P(q)U, EST. 2016), Mariagiulia (MG), Alessandro (Ale), Andrea (Volpe), Elena (Elly), Enrico, Enrico (Chef Troi), Matteo, Fabio, Anna ed Elisa per esserci in ogni momento e grazie per esserci sempre stati! A loro voglio dedicare questo piccolo pensiero:

"Torneremo con o senza la vetta
ma con una storia da raccontare"

-Simone Moro

Grazie anche ad Andrea (Loschi), Giordano, Alessio, Lorenzo (Bigio) e Lorenzo (Lollo) per avermi sostenuto innumerevoli volte ed avermi accompagnato durante gli studi e le avventure del dottorato.

Eccoci ... siamo arrivati alla fine e, con tutta probabilità, avrò dimenticato qualcuno: per questo mi scuso e lascio la mia infinita gratitudine per chi ho avuto la fortuna di conoscere durante questo percorso più o meno tormentato ma sicuramente con tante, tante soddisfazioni.

"If I see but one smile on your lips when we meet,
occasioned by this or any other exertion of mine,
I shall need no other happiness."

-Mary Shelley, Frankenstein, 1818

Acknowledgments

Many people have been with me during the writing of this thesis and everyone has supported me in their own way: those who have actively helped me and those who have stood by me, encouraging me every day. Apart from that, they all played a key role, and I would like to thank them for that. I understand that the task is quite challenging, but I will try my best to include everyone.

A very special thanks goes to my family, to my daddy Renato, to my sister Roberta and to the aunts/uncles who have been encouraging and supporting me day by day: without them, I could not have gone very far. Thanks for everything!

A sincere thanks goes to Prof. Laura Orian who has been following me for 5 years now (this is already the third thesis she reviews!) with constant dedication and professionalism. During my graduation and later, during my doctorate, she assisted me in solving problems of different nature without ever losing the will to do. All the work in this thesis would never have seen the light of day without his essential guidance.

A big thank you also goes to Prof. Matthias Bickelhaupt and Dr. Trevor Hamlin for their constant support during my 6-month stay in Amsterdam at Vrije Universiteit. They welcomed me into their research group and always tried to help me with precious suggestions, making me take an active part in different activities from the first day I was there. Thank you to all my Dutch friends and colleagues for the help and time dedicated to me, where I was taught to see and analyze many details with a new and innovative perspective.

A “Danke vielmals!” goes unquestionably to Prof. Leopold Flohé for reviewing some of my work with extreme dedication and competence.

A huge thank you goes to my friends in sala calcolo: Francesco (Fracni), Marco (grande), Alessandro, Enrico, Maurizio, Pierpaolo, Andrea

(Pischio), Cecilia, Jonathan (JFK), Federico, Matteo, Pietro and Andrea who know me as Marcolino and who have been able to cheer up the atmosphere every day and from whom I learned a lot of new things. Without these, I doubt that the Theoretical Pizza and the many aperitifs that cheered up the end of the working day could have existed!

I could never forget my mountain and climbing friends! Thanks Alice, Davide (founding members of P(q)U, EST. 2016), Mariagiulia (MG), Alessandro (Ale), Andrea (Volpe), Elena (Elly), Enrico, Enrico (Chef Troi), Matteo, Fabio, Anna and Elisa for always being there! I want to dedicate this little thought to them:

"We will come back with or without the summit
but with a story to tell."

-Simone Moro

Thanks also to Andrea (Loschi), Giordano, Alessio, Lorenzo (Bigio) and Lorenzo (Lollo) for supporting me so many times and for accompanying me during my studies and doctoral adventures.

Here we are ... we have reached the very end and, very likely, I forgot someone: I apologize for this and I leave my endless gratitude for those I had the chance to meet during this, more or less turbulent, journey but certainly with many, many satisfactions.

"If I see but one smile on your lips when we meet,
occasioned by this or any other exertion of mine,
I shall need no other happiness."

-Mary Shelley, Frankenstein, 1818

List of publications

- M. Baron, M. Dalla Tiezza, A. Carlotto, C. Tubaro, C. Graiff, L. Orian, *Journal of Organometallic Chemistry* **2018**, 866, 144–152.
- M. Bortoli, F. Zaccaria, M. Dalla Tiezza, M. Bruschi, C. Fonseca Guerra, F. M. Bickelhaupt, L. Orian, *Physical Chemistry Chemical Physics* **2018**, 20, 20874–20885.
- M. Dalla Tiezza, F. M. Bickelhaupt, L. Orian, *ChemPhysChem* **2018**, 19, 1766–1773.
- S. M. Ahmad, M. Dalla Tiezza, L. Orian, *Catalysts* **2019**, 9, 679. (with COVER)
- M. Bortoli, M. Dalla Tiezza, C. Muraro, C. Pavan, G. Ribaudo, A. Rodighiero, C. Tubaro, G. Zagotto, L. Orian, *Computational and Structural Biotechnology Journal* **2019**, 17, 311–318.
- M. Bortoli, M. Dalla Tiezza, C. Muraro, G. Saielli, L. Orian, *Molecules* **2019**, 24, 1250.
- M. Dalla Tiezza, F. M. Bickelhaupt, L. Orian, *ChemistryOpen* **2019**, 8, 143–154. (with COVER)
- M. Dalla Tiezza, G. Ribaudo, L. Orian, *Current Organic Chemistry* **2019**, 23, 1381–1402.
- C. Muraro, M. Dalla Tiezza, C. Pavan, G. Ribaudo, G. Zagotto, L. Orian, *Applied Sciences* **2019**, 9, 3631.
- M. Dalla Tiezza, F. M. Bickelhaupt, L. Flohé, M. Maiorino, F. Ursini, L. Orian, *Redox Biology* **2020**, 34, 101540.
- Madabeni, M. Dalla Tiezza, F. B. Omage, P. A. Nogara, M. Bortoli, J. B. T. Rocha, L. Orian, *Journal of Computational Chemistry* **2020**, 41, 2045–2054.

- M. Tosato, M. Asti, M. Dalla Tiezza, L. Orian, D. Häussinger, R. Vogel, U. Köster, M. Jensen, A. Andrighetto, P. Pastore, V. D. Marco, *Inorganic Chemistry* **2020**, 59, 10907–10919.
- M. Tosato, M. Verona, R. Doro, M. Dalla Tiezza, L. Orian, A. Andrighetto, P. Pastore, G. Marzaro, V. Di Marco, *New Journal of Chemistry* **2020**, 44, 8337–8350.

9 References

[1] R. E. Oesper, *J. Chem. Educ.* **1948**, *25*, 531.

[2] W. Reppe, O. Schlichting, K. Klager, T. Toepel, *Justus Liebigs Ann. Chem.* **1948**, *560*, 1–92.

[3] Y. Wakatsuki, H. Yamazaki, *J. Chem. Soc. Chem. Commun.* **1973**, 280a.

[4] K. P. C. Vollhardt, *Acc. Chem. Res.* **1977**, *10*, 1–8.

[5] K. P. C. Vollhardt, *Angew. Chem. Int. Ed. Engl.* **1984**, *23*, 539–556.

[6] H. Bönnemann, *Angew. Chem. Int. Ed. Engl.* **1978**, *17*, 505–515.

[7] H. Bönnemann, *Angew. Chem. Int. Ed. Engl.* **1985**, *24*, 248–262.

[8] F. A. Villamena, *Molecular Basis of Oxidative Stress: Chemistry, Mechanisms, and Disease Pathogenesis*, Wiley, Hoboken, New Jersey.

[9] O. Epp, R. Ladenstein, A. Wendel, *Eur. J. Biochem.* **1983**, *133*, 51–69.

[10] M. Maiorino, K.-D. Aumann, R. Brigelius-Flohé, D. Doria, J. van den Heuvel, J. McCarthy, A. Roveri, F. Ursini, L. Flohé, *Biol. Chem. Hoppe. Seyler* **1995**, *376*, 651–660.

[11] F. Ursini, M. Maiorino, C. Gregolin, *Biochim. Biophys. Acta* **1985**, *839*, 62–70.

[12] L. Orian, P. Mauri, A. Roveri, S. Toppo, L. Benazzi, V. Bosello-Travain, A. De Palma, M. Maiorino, G. Miotto, M. Zaccarin, A. Polimeno, L. Flohé, F. Ursini, *Free Radic. Biol. Med.* **2015**, *87*, 1–14.

[13] S. Toppo, L. Flohé, F. Ursini, S. Vanin, M. Maiorino, *Biochim. Biophys. Acta BBA - Gen. Subj.* **2009**, *1790*, 1486–1500.

[14] P. A. M. Dirac, *Proc. R. Soc. Lond. Ser. Contain. Pap. Math. Phys. Character* **1929**, *123*, 714–733.

[15] P. Hohenberg, W. Kohn, *Phys. Rev.* **1964**, *136*, B864–B871.

[16] W. Kohn, L. J. Sham, *Phys. Rev.* **1965**, *140*, A1133–A1138.
[17] L. H. Thomas, *Math. Proc. Camb. Philos. Soc.* **1927**, *23*, 542–548.
[18] E. Fermi, *Endiconti Accad. Naz. Dei Lincei* **1927**, 602–607.
[19] E. Fermi, *Z. Für Phys.* **1928**, *48*, 73–79.
[20] F. M. Bickelhaupt, K. N. Houk, *Angew. Chem. Int. Ed.* **2017**, *56*, 10070–10086.
[21] W. J. van Zeist, F. M. Bickelhaupt, *Org. Biomol. Chem.* **2010**, *8*, 3118–3127.
[22] G. T. de Jong, F. M. Bickelhaupt, *ChemPhysChem* **2007**, *8*, 1170–1181.
[23] F. M. Bickelhaupt, *J. Comput. Chem.* **1999**, *20*, 114–128.
[24] F. M. Bickelhaupt, E. J. Baerends, in *Rev. Comput. Chem.* (Eds.: K.B. Lipkowitz, D.B. Boyd), John Wiley & Sons, Inc., Hoboken, NJ, USA, **2000**, pp. 1–86.
[25] K. Morokuma, *J. Chem. Phys.* **1971**, *55*, 1236–1244.
[26] T. Ziegler, A. Rauk, *Theor. Chim. Acta* **1977**, *46*, 1–10.
[27] I. Fernández, F. M. Bickelhaupt, F. P. Cossío, *Chem. Eur. J.* **2012**, *18*, 12395–12403.
[28] S. Grimme, J. Antony, S. Ehrlich, H. Krieg, *J. Chem. Phys.* **2010**, *132*, 154104.
[29] S. Grimme, S. Ehrlich, L. Goerigk, *J. Comput. Chem.* **2011**, *32*, 1456–1465.
[30] C. Amatore, A. Jutand, *J. Organomet. Chem.* **1999**, *576*, 254–278.
[31] J. A. Christiansen, *Adv. Catal.* **1953**, *5*, 311–353.
[32] S. Kozuch, S. Shaik, *Acc. Chem. Res.* **2011**, *44*, 101–110.
[33] L. Orian, M. Swart, F. M. Bickelhaupt, *ChemPhysChem* **2014**, *15*, 219–228.
[34] A. Galano, J. R. Alvarez-Idaboy, *J. Comput. Chem.* **2013**, *34*, 2430–2445.
[35] R. A. Marcus, *Annu. Rev. Phys. Chem.* **1964**, *15*, 155–196.
[36] R. A. Marcus, *Rev. Mod. Phys.* **1993**, *65*, 599–610.
[37] S. F. Nelsen, S. C. Blackstock, Y. Kim, *J. Am. Chem. Soc.* **1987**, *109*, 677–682.
[38] S. F. Nelsen, M. N. Weaver, Y. Luo, J. R. Pladziewicz, L. K. Ausman, T. L. Jentzsch, J. J. O'Konek, *J. Phys. Chem. A* **2006**, *110*, 11665–11676.
[39] S. W. Benson, in *Found. Chem. Kinet.*, Krieger: Florida, **1982**.
[40] M. G. Evans, M. Polanyi, *Trans. Faraday Soc.* **1935**, *31*, 875.
[41] D. G. Truhlar, W. L. Hase, J. T. Hynes, *J. Phys. Chem.* **1983**, *87*, 2664–2682.
[42] M. v. Smoluchowski, *Z. Für Phys. Chem.* **1917**, *92*, 129.
[43] A. Einstein, *Ann. Phys.* **1905**, *322*, 549–560.
[44] G. G. Stokes, in *Math. Phys. Pap.*, Cambridge University Press: Cambridge, **1903**, p. 55.
[45] D. G. Truhlar, *J. Chem. Educ.* **1985**, *62*, 104.
[46] F. C. Collins, G. E. Kimball, *J. Colloid Sci.* **1949**, *4*, 425–437.
[47] A. H. Hoveyda, A. R. Zhugralin, *Nature* **2007**, *450*, 243–251.
[48] K. Tanaka, *Transition-Metal-Mediated Aromatic Ring Construction*, Wiley, Hoboken, New Jersey.
[49] Y. Shibata, K. Tanaka, *Synthesis* **2012**, *44*, 323–350.
[50] D. Broere, E. Ruijter, *Synthesis* **2012**, *44*, 2639–2672.
[51] A. Petit, P. Richard, I. Cacelli, R. Poli, *Chem. Eur. J.* **2006**, *12*, 813–823.

[52] C. G. Hartung, V. Snieckus, in *Mod. Arene Chem.* (Ed.: D. Astruc), Wiley-VCH Verlag GmbH & Co. KGaA, Weinheim, FRG, **2002**, pp. 330–367.

[53] W. Ma, C. Yu, T. Chen, L. Xu, W.-X. Zhang, Z. Xi, *Chem. Soc. Rev.* **2017**, *46*, 1160–1192.

[54] J. H. Hardesty, J. B. Koerner, T. A. Albright, G.-Y. Lee, *J. Am. Chem. Soc.* **1999**, *121*, 6055–6067.

[55] K. Kirchner, M. J. Calhorda, R. Schmid, L. F. Veiros, *J. Am. Chem. Soc.* **2003**, *125*, 11721–11729.

[56] L. Orian, J. N. P. van Stralen, F. M. Bickelhaupt, *Organometallics* **2007**, *26*, 3816–3830.

[57] T. A. Albright, P. Hofmann, R. Hoffmann, C. P. Lillya, P. A. Dobosh, *J. Am. Chem. Soc.* **1983**, *105*, 3396–3411.

[58] M. E. Rerek, L.-N. Ji, F. Basolo, *J. Chem. Soc. Chem. Commun.* **1983**, 1208–1209.

[59] M. J. Calhorda, L. F. Veiros, *Coord. Chem. Rev.* **1999**, *185–186*, 37–51.

[60] M. J. Calhorda, V. Félix, L. F. Veiros, *Coord. Chem. Rev.* **2002**, *230*, 49–64.

[61] L. Orian, A. Bisello, S. Santi, A. Ceccon, G. Saielli, *Chem. Eur. J.* **2004**, *10*, 4029–4040.

[62] L. Orian, P. Ganis, S. Santi, A. Ceccon, *J. Organomet. Chem.* **2005**, *690*, 482–492.

[63] Y. Wakatsuki, H. Yamazaki, *Bull. Chem. Soc. Jpn.* **1985**, *58*, 2715–2716.

[64] H. Bönnemann, *Angew. Chem. Int. Ed. Engl.* **1978**, *17*, 505–515.

[65] H. Bönnemann, *Angew. Chem. Int. Ed. Engl.* **1985**, *24*, 248–262.

[66] K. P. C. Vollhardt, *Acc. Chem. Res.* **1977**, *10*, 1–8.

[67] K. P. C. Vollhardt, *Angew. Chem. Int. Ed. Engl.* **1984**, *23*, 539–556.

[68] K. Abdulla, B. L. Booth, C. Stacey, *J. Organomet. Chem.* **1985**, *293*, 103–114.

[69] P. Cioni, P. Diversi, G. Ingrosso, A. Lucherini, P. Ronca, *J. Mol. Catal.* **1987**, *40*, 337–357.

[70] L. Orian, L. P. Wolters, F. M. Bickelhaupt, *Chem. Eur. J.* **2013**, *19*, 13337–13347.

[71] A. A. Dahy, K. Yamada, N. Koga, *Organometallics* **2009**, *28*, 3636–3649.

[72] B. M. Trost, M. C. Ryan, *Angew. Chem. Int. Ed.* **2017**, *56*, 2862–2879.

[73] L. Orian, W. J. van Zeist, F. M. Bickelhaupt, *Organometallics* **2008**, *27*, 4028–4030.

[74] A. A. Dahy, N. Koga, *Organometallics* **2015**, *34*, 4965–4974.

[75] C.-H. Guo, H.-S. Wu, M. Hapke, H. Jiao, *J. Organomet. Chem.* **2013**, *748*, 29–35.

[76] R. G. Parr, W. Yang, *Density-Functional Theory of Atoms and Molecules*, Oxford Univ. Press, New York, NY.

[77] G. te Velde, F. M. Bickelhaupt, E. J. Baerends, C. Fonseca Guerra, S. J. A. van Gisbergen, J. G. Snijders, T. Ziegler, *J. Comput. Chem.* **2001**, *22*, 931–967.

[78] C. Fonseca Guerra, J. G. Snijders, G. te Velde, E. J. Baerends, *Theor. Chem. Acc.* **1998**, *99*, 391–403.
[79] *ADF 2014-2019.3*, SCM, Theoretical Chemistry, Vrije Universiteit, Amsterdam, The Netherlands, http://www.scm.com.
[80] E. van Lenthe, E. J. Baerends, J. G. Snijders, *J. Chem. Phys.* **1994**, *101*, 9783–9792.
[81] A. D. Becke, *Phys. Rev. A* **1988**, *38*, 3098–3100.
[82] C. Lee, W. Yang, R. G. Parr, *Phys. Rev. B* **1988**, *37*, 785–789.
[83] C. R. Groom, I. J. Bruno, M. P. Lightfoot, S. C. Ward, *Acta Crystallogr. Sect. B Struct. Sci. Cryst. Eng. Mater.* **2016**, *72*, 171–179.
[84] Y. Wakatsuki, T. Sakurai, H. Yamazaki, *J. Chem. Soc. Dalton Trans.* **1982**, 1923–1927.
[85] P. Diversi, G. Ingrosso, A. Lucherini, W. Porzio, M. Zocchi, *J. Chem. Soc. Chem. Commun.* **1977**, 811–812.
[86] R. Bertani, P. Diversi, G. Ingrosso, A. Lucherini, F. Marchetti, V. Adovasio, M. Nardelli, S. Pucci, *J. Chem. Soc. Dalton Trans.* **1988**, 2983–2994.
[87] P. Diversi, G. Ingrosso, A. Lucherini, W. Porzio, M. Zocchi, *Inorg. Chem.* **1980**, *19*, 3590–3597.
[88] A. A. Dahy, C. H. Suresh, N. Koga, *Bull. Chem. Soc. Jpn.* **2005**, *78*, 792–803.
[89] Y. Wakatsuki, O. Nomura, K. Kitaura, K. Morokuma, H. Yamazaki, *J. Am. Chem. Soc.* **1983**, *105*, 1907–1912.
[90] N. Agenet, V. Gandon, K. P. C. Vollhardt, M. Malacria, C. Aubert, *J. Am. Chem. Soc.* **2007**, *129*, 8860–8871.
[91] P. E. Siegbahn, *J. Am. Chem. Soc.* **1996**, *118*, 1487–1496.
[92] A. Dachs, S. Osuna, A. Roglans, M. Solà, *Organometallics* **2010**, *29*, 562–569.
[93] G. Dazinger, M. Torres-Rodrigues, K. Kirchner, M. J. Calhorda, P. J. Costa, *J. Organomet. Chem.* **2006**, *691*, 4434–4445.
[94] F. M. Bickelhaupt, N. M. M. Nibbering, E. M. Van Wezenbeek, E. J. Baerends, *J. Phys. Chem.* **1992**, *96*, 4864–4873.
[95] G. Schmid, M. Schütz, *Organometallics* **1992**, *11*, 1789–1792.
[96] G. Schmid, M. Schütz, *J. Organomet. Chem.* **1995**, *492*, 185–189.
[97] G. Schmid, B. Kilanowski, R. Boese, D. Bläser, *Chem. Ber.* **1993**, *126*, 899–906.
[98] G. Schmid, R. Boese, *Z. Naturforschung B* **1983**, 485–492.
[99] G. Schmid, S. Amirkhalili, U. Höhner, D. Kampmann, R. Boese, *Chem. Ber.* **1982**, *115*, 3830–3841.
[100] G. Schmid, D. Kampmann, U. Höhner, D. Bläser, R. Boese, *Chem. Ber.* **1984**, *117*, 1052–1060.
[101] G. Schmid, F. Schmidt, *Chem. Ber.* **1986**, *119*, 1766–1771.
[102] G. Schmid, D. Kampmann, W. Meyer, R. Boese, P. Paetzold, K. Delpy, *Chem. Ber.* **1985**, *118*, 2418–2428.
[103] S.-Y. Liu, M. M.-C. Lo, G. C. Fu, *Angew. Chem.* **2002**, *114*, 182–184.
[104] A. J. Ashe, Fang, *Org. Lett.* **2000**, *2*, 2089–2091.

[105] A. J. Ashe, X. Fang, X. Fang, J. W. Kampf, *Organometallics* **2001**, *20*, 5413–5418.

[106] X. Fang, H. Yang, J. W. Kampf, M. M. Banaszak Holl, A. J. Ashe, *Organometallics* **2006**, *25*, 513–518.

[107] J. P. Collman, J. W. Kang, W. F. Little, M. F. Sullivan, *Inorg. Chem.* **1968**, *7*, 1298–1303.

[108] P. Diversi, L. Ermini, G. Ingrosso, A. Lucherini, *J. Organomet. Chem.* **1993**, *447*, 291–298.

[109] A. W. Fatland, B. E. Eaton, *Org. Lett.* **2000**, *2*, 3131–3133.

[110] L. Yong, H. Butenschön, *J. Chem. Soc. Chem. Commun.* **2002**, 2852–2853.

[111] M. Dalla Tiezza, F. M. Bickelhaupt, L. Orian, *ChemPhysChem* **2018**, *19*, 1766–1773.

[112] N. E. Schore, *Chem. Rev.* **1988**, *88*, 1081–1119.

[113] C. C. Pye, T. Ziegler, *Theor. Chem. Acc.* **1999**, *101*, 396–408.

[114] M. E. Rerek, F. Basolo, *J. Am. Chem. Soc.* **1984**, *106*, 5908–5912.

[115] F. A. Villamena, *Molecular Basis of Oxidative Stress: Chemistry, Mechanisms, and Disease Pathogenesis*, Wiley, Hoboken, New Jersey.

[116] M. F. Christman, R. W. Morgan, F. S. Jacobson, B. N. Ames, *Cell* **1985**, *41*, 753–762.

[117] M. Herbet, M. Gawrońska-Grzywacz, M. Izdebska, I. Piątkowska-Chmiel, *Exp. Ther. Med.* **2016**, *12*, 3440–3444.

[118] J. N. Cobley, M. L. Fiorello, D. M. Bailey, *Redox Biol.* **2018**, *15*, 490–503.

[119] J. A. Gingrich, *Nat. Med.* **2005**, *11*, 1281–1282.

[120] C. S. Nunes, M. Maes, C. Roomruangwong, J. B. Moraes, K. L. Bonifacio, H. O. Vargas, D. S. Barbosa, G. Anderson, L. G. P. de Melo, S. Drozdstoj, E. Moreira, A. F. Carvalho, S. O. V. Nunes, *J. Eval. Clin. Pract.* **2018**, *24*, 869–878.

[121] S. Salim, *Curr. Neuropharmacol.* **2014**, *12*, 140–147.

[122] W. Hassan, H. Noreen, V. Castro-Gomes, I. Mohammadzai, J. Batista Teixeira da Rocha, J. Landeira-Fernandez, *Curr. Pharm. Des.* **2016**, *22*, 2960–2974.

[123] S. Tsaluchidu, M. Cocchi, L. Tonello, B. K. Puri, *BMC Psychiatry* **2008**, *8*, S5.

[124] J. Allen, R. Romay-Tallon, K. J. Brymer, H. J. Caruncho, L. E. Kalynchuk, *Front. Neurosci.* **2018**, *12*, 386.

[125] C. N. Black, M. Bot, P. G. Scheffer, P. Cuijpers, B. W. J. H. Penninx, *Psychoneuroendocrinology* **2015**, *51*, 164–175.

[126] G. Ribaudo, M. Bortoli, C. Pavan, G. Zagotto, L. Orian, *Antioxidants* **2020**, *9*, 714.

[127] M. Bortoli, M. Dalla Tiezza, C. Muraro, C. Pavan, G. Ribaudo, A. Rodighiero, C. Tubaro, G. Zagotto, L. Orian, *Comput. Struct. Biotechnol. J.* **2019**, *17*, 311–318.

[128] C. Muraro, M. Dalla Tiezza, C. Pavan, G. Ribaudo, G. Zagotto, L. Orian, *Appl. Sci.* **2019**, *9*, 3631.

[129] R. H. Schirmer, B. Coulibaly, A. Stich, M. Scheiwein, H. Merkle, J. Eubel, K. Becker, H. Becher, O. Müller, T. Zich, W. Schiek, B. Kouyaté, *Redox Rep.* **2003**, *8*, 272–275.

[130] A. Pascual, M. Henry, S. Briolant, S. Charras, E. Baret, R. Amalvict, E. Huyghues des Etages, M. Feraud, C. Rogier, B. Pradines, *Antimicrob. Agents Chemother.* **2011**, *55*, 2472–2474.

[131] G. Ribaudo, M. Bortoli, A. Ongaro, E. Oselladore, A. Gianoncelli, G. Zagotto, L. Orian, *RSC Adv.* **2020**, *10*, 18583–18593.

[132] M. J. Frisch, G. W. Trucks, H. B. Schlegel, G. E. Scuseria, M. A. Robb, J. R. Cheeseman, G. Scalmani, V. Barone, G. A. Petersson, H. Nakatsuji, X. Li, M. Caricato, A. V. Marenich, J. Bloino, B. G. Janesko, R. Gomperts, B. Mennucci, H. P. Hratchian, J. V. Ortiz, A. F. Izmaylov, J. L. Sonnenberg, Williams, F. Ding, F. Lipparini, F. Egidi, J. Goings, B. Peng, A. Petrone, T. Henderson, D. Ranasinghe, V. G. Zakrzewski, J. Gao, N. Rega, G. Zheng, W. Liang, M. Hada, M. Ehara, K. Toyota, R. Fukuda, J. Hasegawa, M. Ishida, T. Nakajima, Y. Honda, O. Kitao, H. Nakai, T. Vreven, K. Throssell, J. A. Montgomery Jr., J. E. Peralta, F. Ogliaro, M. J. Bearpark, J. J. Heyd, E. N. Brothers, K. N. Kudin, V. N. Staroverov, T. A. Keith, R. Kobayashi, J. Normand, K. Raghavachari, A. P. Rendell, J. C. Burant, S. S. Iyengar, J. Tomasi, M. Cossi, J. M. Millam, M. Klene, C. Adamo, R. Cammi, J. W. Ochterski, R. L. Martin, K. Morokuma, O. Farkas, J. B. Foresman, D. J. Fox, *Gaussian 16 Rev. C.01*, Wallingford, CT.

[133] Y. Zhao, D. G. Truhlar, *Theor. Chem. Acc.* **2008**, *120*, 215–241.

[134] A. D. McLean, G. S. Chandler, *J. Chem. Phys.* **1980**, *72*, 5639–5648.

[135] R. Krishnan, J. S. Binkley, R. Seeger, J. A. Pople, *J. Chem. Phys.* **1980**, *72*, 650–654.

[136] T. H. Dunning, *J. Chem. Phys.* **1989**, *90*, 1007–1023.

[137] A. K. Wilson, D. E. Woon, K. A. Peterson, T. H. Dunning, *J. Chem. Phys.* **1999**, *110*, 7667–7676.

[138] A. V. Marenich, C. J. Cramer, D. G. Truhlar, *J. Phys. Chem. B* **2009**, *113*, 6378–6396.

[139] C. L. Bianco, J. P. Toscano, J. M. Fukuto, in *Nitric Oxide*, Elsevier, **2017**, pp. 9–21.

[140] E. G. Hrycay, S. M. Bandiera, in *Adv. Pharmacol.*, Elsevier, **2015**, pp. 35–84.

[141] J. P. Kehrer, J. D. Robertson, C. V. Smith, in *Compr. Toxicol.*, Elsevier, **2010**, pp. 277–307.

[142] H. Sies, *Eur. J. Biochem.* **1993**, *215*, 213–219.

[143] W. H. Koppenol, D. M. Stanbury, P. L. Bounds, *Free Radic. Biol. Med.* **2010**, *49*, 317–322.

[144] J. A. Dobado, H. Martínez-García, Molina, M. R. Sundberg, *J. Am. Chem. Soc.* **1999**, *121*, 3156–3164.

[145] A. Galano, J. R. Alvarez-Idaboy, *RSC Adv.* **2011**, *1*, 1763.

[146] M. Quintiliani, R. Badiello, M. Tamba, A. Esfandi, G. Gorin, *Int. J. Radiat. Biol. Relat. Stud. Phys. Chem. Med.* **1977**, *32*, 195–202.

[147] T. E. Eriksen, G. Fransson, *J. Chem. Soc. Perkin Trans. 2* **1988**, 1117.
[148] D. Hofstetter, T. Nauser, W. H. Koppenol, *Chem. Res. Toxicol.* **2010**, *23*, 1596–1600.
[149] M. Z. Baker, R. Badiello, M. Tamba, M. Quintiliani, G. Gorin, *Int. J. Radiat. Biol. Relat. Stud. Phys. Chem. Med.* **1982**, *41*, 595–602.
[150] A. Galano, J. R. Alvarez-Idaboy, M. Francisco-Márquez, *J. Phys. Chem. B* **2011**, *115*, 13101–13109.
[151] R. Joshi, M. S. Kumar, K. Satyamoorthy, M. K. Unnikrisnan, T. Mukherjee, *J. Agric. Food Chem.* **2005**, *53*, 2696–2703.
[152] J. R. León-Carmona, A. Galano, *J. Phys. Chem. B* **2011**, *115*, 4538–4546.
[153] P. C. Kesavan, E. L. Powers, *Int. J. Radiat. Biol. Relat. Stud. Phys. Chem. Med.* **1985**, *48*, 223–233.
[154] T. P. A. Devasagayam, J. P. Kamat, H. Mohan, P. C. Kesavan, *Biochim. Biophys. Acta BBA - Biomembr.* **1996**, *1282*, 63–70.
[155] V. Brezová, A. Šlebodová, A. Staško, *Food Chem.* **2009**, *114*, 859–868.
[156] T. Masuda, K. Yamada, T. Maekawa, Y. Takeda, H. Yamaguchi, *J. Agric. Food Chem.* **2006**, *54*, 6069–6074.
[157] A. D. N. J. de Grey, *DNA Cell Biol.* **2002**, *21*, 251–257.
[158] B. Poeggeler, R. J. Reiter, R. Hardeland, D.-X. Tan, L. R. Barlow-Walden, *Redox Rep.* **1996**, *2*, 179–184.
[159] Z. Matuszak, K. J. Reszka, C. F. Chignell, *Free Radic. Biol. Med.* **1997**, *23*, 367–372.
[160] J. E. Roberts, D.-N. Hu, J. F. Wishart, *J. Photochem. Photobiol. B* **1998**, *42*, 125–132.
[161] P. Stasica, P. Ulanski, J. M. Rosiak, *J. Radioanal. Nucl. Chem.* **1998**, *232*, 107–113.
[162] Y.-J. Chyan, B. Poeggeler, R. A. Omar, D. G. Chain, B. Frangione, J. Ghiso, M. A. Pappolla, *J. Biol. Chem.* **1999**, *274*, 21937–21942.
[163] Y. Villuendas-Rey, J. R. Alvarez-Idaboy, A. Galano, *J. Chem. Inf. Model.* **2015**, *55*, 2552–2561.
[164] A. Galano, A. Martínez, *J. Phys. Chem. B* **2012**, *116*, 1200–1208.
[165] Y. Okada, K. Tanaka, E. Sato, H. Okajima, *J. Am. Oil Chem. Soc.* **2010**, *87*, 1397–1405.
[166] A. Galano, J. R. Alvarez-Idaboy, M. Francisco-Márquez, M. E. Medina, *Theor. Chem. Acc.* **2012**, *131*, 1173.
[167] N. M. Storozhok, N. V. Gureeva, A. P. Krysin, V. E. Borisenko, I. F. Rusina, N. G. Khrapova, E. B. Burlakova, *Kinet. Catal.* **2004**, *45*, 488–496.
[168] O. I. Aruoma, P. J. Evans, H. Kaur, L. Sutcliffe, B. Halliwell, *Free Radic. Res. Commun.* **1990**, *10*, 143–157.
[169] A. Pérez-González, A. Galano, *J. Phys. Chem. B* **2011**, *115*, 1306–1314.
[170] S. Abe, K. Kirima, K. Tsuchiya, M. Okamoto, T. Hasegawa, H. Houchi, M. Yoshizumi, T. Tamaki, *Chem. Pharm. Bull. (Tokyo)* **2004**, *52*, 186–191.
[171] M. Lin, Y. Katsumura, K. Hata, Y. Muroya, K. Nakagawa, *J. Photochem. Photobiol. B* **2007**, *89*, 36–43.

[172] D. L. Klayman, W. H. H. Günther, *Organic Selenium Compounds: Their Chemistry and Biology*, Wiley-Interscience, New York.

[173] G. Ribaudo, M. Bellanda, I. Menegazzo, L. P. Wolters, M. Bortoli, G. Ferrer-Sueta, G. Zagotto, L. Orian, *Chem. Eur. J.* **2017**, *23*, 2405–2422.

[174] J. Egea, I. Fabregat, Y. M. Frapart, P. Ghezzi, A. Görlach, T. Kietzmann, K. Kubaichuk, U. G. Knaus, M. G. Lopez, G. Olaso-Gonzalez, A. Petry, R. Schulz, J. Vina, P. Winyard, K. Abbas, O. S. Ademowo, C. B. Afonso, I. Andreadou, H. Antelmann, F. Antunes, M. Aslan, M. M. Bachschmid, R. M. Barbosa, V. Belousov, C. Berndt, D. Bernlohr, E. Bertrán, A. Bindoli, S. P. Bottari, P. M. Brito, G. Carrara, A. I. Casas, A. Chatzi, N. Chondrogianni, M. Conrad, M. S. Cooke, J. G. Costa, A. Cuadrado, P. My-Chan Dang, B. De Smet, B. Debelec–Butuner, I. H. K. Dias, J. D. Dunn, A. J. Edson, M. El Assar, J. El-Benna, P. Ferdinandy, A. S. Fernandes, K. E. Fladmark, U. Förstermann, R. Giniatullin, Z. Giricz, A. Görbe, H. Griffiths, V. Hampl, A. Hanf, J. Herget, P. Hernansanz-Agustín, M. Hillion, J. Huang, S. Ilikay, P. Jansen-Dürr, V. Jaquet, J. A. Joles, B. Kalyanaraman, D. Kaminskyy, M. Karbaschi, M. Kleanthous, L.-O. Klotz, B. Korac, K. S. Korkmaz, R. Koziel, D. Kračun, K.-H. Krause, V. Křen, T. Krieg, J. Laranjinha, A. Lazou, H. Li, A. Martínez-Ruiz, R. Matsui, G. J. McBean, S. P. Meredith, J. Messens, V. Miguel, Y. Mikhed, I. Milisav, L. Milković, A. Miranda-Vizuete, M. Mojović, M. Monsalve, P.-A. Mouthuy, J. Mulvey, T. Münzel, V. Muzykantov, I. T. N. Nguyen, M. Oelze, N. G. Oliveira, C. M. Palmeira, N. Papaevgeniou, A. Pavićević, B. Pedre, F. Peyrot, M. Phylactides, G. G. Pircalabioru, A. R. Pitt, H. E. Poulsen, I. Prieto, M. P. Rigobello, N. Robledinos-Antón, L. Rodríguez-Mañas, A. P. Rolo, F. Rousset, T. Ruskovska, N. Saraiva, S. Sasson, K. Schröder, K. Semen, T. Seredenina, A. Shakirzyanova, G. L. Smith, T. Soldati, B. C. Sousa, C. M. Spickett, A. Stancic, M. J. Stasia, H. Steinbrenner, V. Stepanić, S. Steven, K. Tokatlidis, E. Tuncay, B. Turan, F. Ursini, J. Vacek, O. Vajnerova, K. Valentová, F. Van Breusegem, L. Varisli, E. A. Veal, A. S. Yalçın, O. Yelisyeyeva, N. Žarković, M. Zatloukalová, J. Zielonka, R. M. Touyz, A. Papapetropoulos, T. Grune, S. Lamas, H. H. H. W. Schmidt, F. Di Lisa, A. Daiber, *Redox Biol.* **2017**, *13*, 94–162.

[175] M. Bortoli, F. Zaccaria, M. Dalla Tiezza, M. Bruschi, C. Fonseca Guerra, F. M. Bickelhaupt, L. Orian, *Phys. Chem. Chem. Phys.* **2018**, *20*, 20874–20885.

[176] M. Bortoli, M. Bruschi, M. Swart, L. Orian, *New J. Chem.* **2020**, *44*, 6724–6731.

[177] H. J. Reich, R. J. Hondal, *ACS Chem. Biol.* **2016**, *11*, 821–841.

[178] L. Orian, G. Cozza, M. Maiorino, S. Toppo, F. Ursini, in *Glutathione*, CRC Press (2018) Ed., **2018**, pp. 53–66.

[179] G. C. Mills, *J. Biol. Chem.* **1957**, *229*, 189–197.

[180] W. A. Günzler, H. Vergin, I. Müller, L. Flohé, *Hoppe. Seylers Z. Physiol. Chem.* **1972**, *353*, 1001–1004.

[181] L. Orian, P. Mauri, A. Roveri, S. Toppo, L. Benazzi, V. Bosello-Travain, A. De Palma, M. Maiorino, G. Miotto, M. Zaccarin, A. Polimeno, L. Flohé, F. Ursini, *Free Radic. Biol. Med.* **2015**, *87*, 1–14.

[182] M. Bortoli, M. Torsello, F. M. Bickelhaupt, L. Orian, *ChemPhysChem* **2017**, *18*, 2990–2998.

[183] R. Prabhakar, T. Vreven, K. Morokuma, D. G. Musaev, *Biochemistry* **2005**, *44*, 11864–11871.

[184] R. Prabhakar, K. Morokuma, D. G. Musaev, *Biochemistry* **2006**, *45*, 6967–6977.

[185] M. Maiorino, K.-D. Aumann, R. Brigelius-Flohé, D. Doria, J. van den Heuvel, J. McCarthy, A. Roveri, F. Ursini, L. Flohé, *Biol. Chem. Hoppe. Seyler* **1995**, *376*, 651–660.

[186] L. Flohé, G. Loschen, W. A. Günzler, E. Eichele, *Hoppe-Seyler´s Z. Für Physiol. Chem.* **1972**, *353*, 987–1000.

[187] S. Toppo, L. Flohé, F. Ursini, S. Vanin, M. Maiorino, *Biochim. Biophys. Acta BBA - Gen. Subj.* **2009**, *1790*, 1486–1500.

[188] M. Dalla Tiezza, F. M. Bickelhaupt, L. Flohé, M. Maiorino, F. Ursini, L. Orian, *Redox Biol.* **2020**, *34*, 101540.

[189] A. D. Becke, *J. Chem. Phys.* **1993**, *98*, 5648–5652.

[190] C. Lee, W. Yang, R. G. Parr, *Phys. Rev. B* **1988**, *37*, 785–789.

[191] P. J. Stephens, F. J. Devlin, C. F. Chabalowski, M. J. Frisch, *J. Phys. Chem.* **1994**, *98*, 11623–11627.

[192] S. H. Vosko, L. Wilk, M. Nusair, *Can. J. Phys.* **1980**, *58*, 1200–1211.

[193] P. Scheerer, A. Borchert, N. Krauss, H. Wessner, C. Gerth, W. Höhne, H. Kühn, *Biochemistry* **2007**, *46*, 9041–9049.

[194] L. J. Thénard, *Ann. Chim. Phys.* **1818**, *8*, 306–312.

[195] C. F. Schönbein, *J. Für Prakt. Chem.* **1863**, *89*, 323–344.

[196] G. Linossier, *C. R. Seances Soc. Biol. Fil.* **1898**, *50*, 373–375.

[197] L. Planche, *Bull Pharm* **1810**, 578–580.

[198] O. Loew, *Science* **1900**, *11*, 701–702.

[199] C. Glorieux, P. B. Calderon, *Biol. Chem.* **2017**, *398*, 1095–1108.

[200] K. G. Stern, *Yale J. Biol. Med.* **1937**, *10*, 161–178.

[201] A. Brill, in *Compr. Biochem.*, Florkin M, Stotz EH. Amsterdam: Elsevier, **1966**, pp. 447–479.

[202] B. Chance, G. R. Schonbaum, in *The Enzymes*, Academic Press, New York, **1976**, pp. 362–408.

[203] L. Flohé, *Biochim. Biophys. Acta BBA - Gen. Subj.* **2009**, *1790*, 1389–1403.

[204] L. Flohe, W. A. Günzler, H. H. Schock, *FEBS Lett.* **1973**, *32*, 132–134.

[205] J. T. Rotruck, A. L. Pope, H. E. Ganther, A. B. Swanson, D. G. Hafeman, W. G. Hoekstra, *Science* **1973**, *179*, 588–590.

[206] J. W. Forstrom, J. J. Zakowski, A. L. Tappel, *Biochemistry* **1978**, *17*, 2639–2644.

[207] A. Wendel, B. Kerner, K. Graupe, in *Funct. Glutathione Liver Kidney* (Eds.: H. Sies, A. Wendel), Springer Berlin Heidelberg, Berlin, Heidelberg, **1978**, pp. 107–113.

[208] F. Ursini, M. Maiorino, C. Gregolin, *Biochim. Biophys. Acta BBA - Gen. Subj.* **1985**, *839*, 62–70.

[209] M. Maiorino, F. Ursini, V. Bosello, S. Toppo, S. C. E. Tosatto, P. Mauri, K. Becker, A. Roveri, C. Bulato, L. Benazzi, A. De Palma, L. Flohé, *J. Mol. Biol.* **2007**, *365*, 1033–1046.

[210] L. Flohé, J. R. Harris, *Subcell. Biochem.* **2007**, *44*, 1–25.

[211] S. G. Rhee, H. Z. Chae, K. Kim, *Free Radic. Biol. Med.* **2005**, *38*, 1543–1552.

[212] B. Söhling, T. Parther, K. P. Rücknagel, M. Wagner, J. R. Andreesen, *Biol. Chem.* **2001**, *382*, 979–986.

[213] L. Flohé, S. Toppo, G. Cozza, F. Ursini, *Antioxid. Redox Signal.* **2011**, *15*, 763–780.

[214] R. Brigelius-Flohé, L. Flohé, *Antioxid. Redox Signal.* **2011**, *15*, 2335–2381.

[215] A. Zeida, M. Trujillo, G. Ferrer-Sueta, A. Denicola, D. A. Estrin, R. Radi, *Chem. Rev.* **2019**, *119*, 10829–10855.

[216] L. Flohé, *Free Radic. Res.* **2016**, *50*, 126–142.

[217] A. Delaunay, D. Pflieger, M.-B. Barrault, J. Vinh, M. B. Toledano, *Cell* **2002**, *111*, 471–481.

[218] B. A. Morgan, E. A. Veal, in *Peroxiredoxin Syst.* (Eds.: L. Flohé, J.R. Harris), Springer Netherlands, Dordrecht, **2007**, pp. 253–265.

[219] M. C. Sobotta, W. Liou, S. Stöcker, D. Talwar, M. Oehler, T. Ruppert, A. N. D. Scharf, T. P. Dick, *Nat. Chem. Biol.* **2015**, *11*, 64–70.

[220] K. D. Tew, in *Glutathione*, Flohé L. Boca Raton FL: CRC Press, **2019**, pp. 201–313.

[221] S. Stöcker, M. Maurer, T. Ruppert, T. P. Dick, *Nat. Chem. Biol.* **2018**, *14*, 148–155.

[222] T. Hildebrandt, J. Knuesting, C. Berndt, B. Morgan, R. Scheibe, *Biol. Chem.* **2015**, *396*, 523–537.

[223] G. Ferrer-Sueta, B. Manta, H. Botti, R. Radi, M. Trujillo, A. Denicola, *Chem. Res. Toxicol.* **2011**, *24*, 434–450.

[224] C. C. Winterbourn, in *Methods Enzymol.*, Elsevier, **2013**, pp. 3–25.

[225] C. C. Winterbourn, M. B. Hampton, *Free Radic. Biol. Med.* **2008**, *45*, 549–561.

[226] D. A. Meireles, R. M. Domingos, J. W. Gaiarsa, E. G. Ragnoni, R. Bannitz-Fernandes, J. F. da Silva Neto, R. F. de Souza, L. E. S. Netto, *Redox Biol.* **2017**, *12*, 600–609.

[227] D. Peralta, A. K. Bronowska, B. Morgan, É. Dóka, K. Van Laer, P. Nagy, F. Gräter, T. P. Dick, *Nat. Chem. Biol.* **2015**, *11*, 156–163.

[228] L. A. H. van Bergen, M. Alonso, A. Palló, L. Nilsson, F. De Proft, J. Messens, *Sci. Rep.* **2016**, *6*, 30369.

[229] J. L. Jenkins, J. J. Tanner, *Acta Crystallogr. D Biol. Crystallogr.* **2006**, *62*, 290–301.

[230] I. Jo, I.-Y. Chung, H.-W. Bae, J.-S. Kim, S. Song, Y.-H. Cho, N.-C. Ha, *Proc. Natl. Acad. Sci.* **2015**, *112*, 6443–6448.

[231] B. Cardey, M. Enescu, *ChemPhysChem* **2005**, *6*, 1175–1180.

[232] B. Pedre, D. Young, D. Charlier, Á. Mourenza, L. A. Rosado, L. Marcos-Pascual, K. Wahni, E. Martens, A. G. de la Rubia, V. V. Belousov, L. M. Mateos, J. Messens, *Proc. Natl. Acad. Sci.* **2018**, *115*, E11623–E11632.

[233] M. Trujillo, G. Ferrer-Sueta, L. Thomson, L. Flohé, R. Radi, in *Peroxiredoxin Syst.* (Eds.: L. Flohé, J.R. Harris), Springer Netherlands, Dordrecht, **2007**, pp. 83–113.

[234] N. J. DeYonker, K. A. Peterson, A. K. Wilson, *J. Phys. Chem. A* **2007**, *111*, 11383–11393.

[235] V. Asgeirsson, B. O. Birgisson, R. Bjornsson, U. Becker, F. Neese, C. Riplinger, H. Jonsson, **n.d.**

[236] F. Neese, *WIREs Comput. Mol. Sci.* **2012**, *2*, 73–78.

[237] F. Neese, *WIREs Comput. Mol. Sci.* **2018**, *8*, DOI 10.1002/wcms.1327.

[238] L. Li, C. Li, Z. Zhang, E. Alexov, *J. Chem. Theory Comput.* **2013**, *9*, 2126–2136.

[239] A. Zeida, C. M. Guardia, P. Lichtig, L. L. Perissinotti, L. A. Defelipe, A. Turjanski, R. Radi, M. Trujillo, D. A. Estrin, *Biophys. Rev.* **2014**, *6*, 27–46.

[240] B. Pedre, L. A. H. van Bergen, A. Palló, L. A. Rosado, V. T. Dufe, I. V. Molle, K. Wahni, H. Erdogan, M. Alonso, F. D. Proft, J. Messens, *Chem. Commun.* **2016**, *52*, 10293–10296.

[241] L. Flohé, H. Budde, K. Bruns, H. Castro, J. Clos, B. Hofmann, S. Kansal-Kalavar, D. Krumme, U. Menge, K. Plank-Schumacher, H. Sztajer, J. Wissing, C. Wylegalla, H.-J. Hecht, *Arch. Biochem. Biophys.* **2002**, *397*, 324–335.

[242] C. Fonseca Guerra, F. M. Bickelhaupt, J. G. Snijders, E. J. Baerends, *Chem. – Eur. J.* **1999**, *5*, 3581–3594.

[243] L. P. Wolters, F. M. Bickelhaupt, *ChemistryOpen* **2012**, *1*, 96–105.

[244] A. Hall, D. Parsonage, L. B. Poole, P. A. Karplus, *J. Mol. Biol.* **2010**, *402*, 194–209.

[245] A. Zeida, A. M. Reyes, M. C. G. Lebrero, R. Radi, M. Trujillo, D. A. Estrin, *J. Chem. Soc. Chem. Commun.* **2014**, *50*, 10070–10073.

[246] E. Cuevasanta, A. M. Reyes, A. Zeida, M. Mastrogiovanni, M. I. De Armas, R. Radi, B. Alvarez, M. Trujillo, *J. Biol. Chem.* **2019**, *294*, 13593–13605.

[247] E. Derat, S. Shaik, C. Rovira, P. Vidossich, M. Alfonso-Prieto, *J. Am. Chem. Soc.* **2007**, *129*, 6346–6347.

[248] P. Vidossich, G. Fiorin, M. Alfonso-Prieto, E. Derat, S. Shaik, C. Rovira, *J. Phys. Chem. B* **2010**, *114*, 5161–5169.